

Computational models of human and animal larynx and vocal folds

Hani Bakhshaee

Doctor of Philosophy

Department of Mechanical Engineering

McGill University

Montreal, Quebec

August 2013

A dissertation submitted to McGill University in partial fulfillment of the
requirements for the degree of Doctor of Philosophy

Copyright ©2013 by Hani Bakhshaee

To all children with cancer all over the world

Abstract

Voice production is the result of the fluid-structure-interaction (FSI) of airflow through glottis and the vocal folds. The physics of the voice production consists of the geometry of the vocal folds and larynx, the aerodynamics of the airflow within larynx, and mechanical properties of the vocal folds. Through these physical aspects of voice production, engineering analyses can contribute to voice research. Creation of patient-specific computer models of the vocal folds and larynx may be considered as one of the main contributions of engineering studies in voice research. Person-to-person differences in voice parameters are considered in patient-specific models and as a result, they have high potential for clinical applications. In this dissertation, the aforementioned physical aspects of voice production were studied through the creation of patient-specific geometries, numerical analyses on glottal airflow, and investigation of the vocal folds' strain-stress field during oscillation.

To address the geometry parameters, the patient-specific three-dimensional (3D) geometries of the vocal folds, larynx, and laryngeal cartilages (i.e., thyroid, cricoid and arytenoid) were built. Morphometric measurements were performed and the obtained results were compared to the existing cadaver data. Low discrepancies between these measurements indicate the feasibility of using Computed Tomography (CT) scan data for creation of 3D models. General laryngeal cartilage models were created while preserving all the biomechanically important morphometric features.

A methodology to create accurate geometries of the vocal folds with desired glottal angles was introduced based on mapping high-speed digital imaging (HSDI) data with that from Magnetic Resonance Imaging (MRI).

To address the fluid dynamics of voice production, the quasi-steady approximation in glottal airflow simulations was investigated in a two dimensional (2D) driven model. The surface area of the model was kept constant to avoid volume variations. Two-dimensional dynamic simulations of airflow through an idealized glottal orifice with moving walls were performed. A series of steady flow simulations was then performed using vocal fold configurations and boundary conditions that instantaneously coincide with data from the dynamic simulations. Aerodynamic parameters such as fluid flow rate, normal pressure on the vocal folds, shear stress on the glottal walls, and orifice discharge coefficients were compared between the dynamic and static simulations and similarities and differences were discussed.

Three-dimensional simulations of the glottal airflow within patient-specific geometries were performed. One of the models was for a healthy subject and the second model was a postsurgical geometry from a patient with cancer. The effects of the geometry differences on the aerodynamic parameters such as orifice discharge coefficient and flow resistance were shown and discussed. To investigate the 3D nature of the glottal airflow, a 2D simulation was conducted in a computational domain made from a frontal CT scan image. The 2D results were compared to the corresponding slice in the 3D simulation. Significant differences between 2D and 3D simulations were observed in orifice discharge coefficients, jet flow deflection, and

secondary flow, highlighting the importance of using realistic 3D models for glottal airflow simulations.

To address the mechanical properties of the vocal folds, the deformation field on the superior visible surface of the vocal folds was captured in the excised larynx experiments using Digital Image Correlation (DIC). An isotropic constitutive law, the polymer eight-chain model, was used to estimate the surface distributions of planar and impact stresses from the strain data. The initial pre-phonatory strain was measured using a dissection protocol and added to the relative strain obtained during the vocal folds' vibration to calculate the net strain. Kinematics of the vocal folds' oscillation was compared to that of synthetic models and similarities and differences were discussed.

Résumé

La production de la voix résulte de l’interaction fluide-structure entre l’écoulement d’air dans la glotte et les cordes vocales. La physique de la production de la voix comporte trois aspects principaux que sont respectivement la géométrie des cordes vocales et du larynx, l’aérodynamique de l’écoulement d’air et les propriétés mécaniques des cordes vocales. Ces trois aspects de la production vocale se situent dans le cadre de l’ingénierie. La création de modèles numériques de cordes vocales et de larynx spécifiques à l’patient peut être vue comme une contribution majeure pour l’analyse technique dans la recherche sur la voix. Ces modèles ont beaucoup d’intérêt pour les applications médicales et thérapeutiques parce qu’ils prennent en compte la variation des propriétés des tissus et de la géométrie entre chaque individu. Dans cette thèse, trois aspects de la production vocale ont été pris en compte : la création de modèles géométriques propres à chaque individu, l’analyse numérique de l’écoulement glottique et la recherche des relations entre les déformations et les contraintes au sein des cordes vocales au cours de la vibration. Afin d’obtenir des paramètres géométriques, des modèles numériques de cordes vocales, du larynx et des cartilages laryngés (i.e. la thyroïde, le cricoïde et les arytenoïdes) ont été conçus en trois dimensions et pour chaque patient. Des mesures morphométriques ont été réalisées et comparées à des données ex-vivo. La faible divergence entre ces mesures a permis de valider l’utilisation de la tomographie par rayons X pour la création de

modèles 3D. Des modèles standards de cartilages laryngés furent créés tout en conservant les caractéristiques biomécaniques importantes. Une méthode basée sur la mise en correspondance de données d'imageries haute vitesse (HSDI) et d'Imageries par Résonnance Magnétique (IRM), a été introduite pour créer des géométries précises des cordes vocales avec le contour glottique souhaité. La dynamique des fluides lors de la production vocale a été étudiée en utilisant une approximation quasi-statique de l'écoulement glottique dans un modèle 2D. La surface du modèle était fixée constante afin d'éviter des variations de volume et éliminer ainsi la création de sources monopôles parasites. Les simulations dynamiques à deux dimensions de l'écoulement de l'air ont alors été réalisées à travers une glotte idéale aux parois mobiles. Une série de simulations d'écoulement statique étaient alors réalisées en utilisant les configurations de cordes vocales ainsi que les conditions aux limites qui coïncidaient avec les données provenant des simulations dynamiques au même instant. Les paramètres aérodynamiques tels que le débit du fluide, la pression normale aux cordes vocales, la contrainte de cisaillement sur les parois glottiques, le coefficient de perte de charge ont été comparés et discutés pour les simulations dynamiques et statiques. Des simulations 3D de l'écoulement glottique ont été réalisées pour chaque modèle individuel. Une des géométries étaient considérée comme saine et la seconde correspondait à la géométrie post-chirurgicale pour un patient atteint d'un cancer. Les effets des différences géométriques sur les paramètres aérodynamiques tels que le coefficient de perte de charge dû à un changement de section et la résistance à l'écoulement ont été mis en valeur et discutés. Afin d'étudier le comportement 3D de l'écoulement d'air

glottique, des calculs 2D ont été effectués à partir des domaines numériques construits à l'aide des images tomographiques dans le plan frontal. Les résultats des calculs 2D ont alors été comparés au tranches correspondantes dans la simulation 3D. Des écarts notables ont été observés entre les simulations 2D et 3D concernant les pertes de charge lors d'un changement de section, la déviation de l'écoulement du jet d'air et la mise en valeur d'un écoulement secondaire, soulignant donc l'importance d'utiliser des modèles 3D réalistes pour simuler l'écoulement glottique. Afin de caractériser les propriétés mécaniques des cordes vocales, le champ de déformation de la surface supérieure et visible des cordes vocales d'un larynx excisé a été mesuré à l'aide d'une technique de corrélation d'image numérique (DIC). Les distributions surfaciques des contraintes planes et de contact ont été estimées à partir des déformations en utilisant une loi de constitution isotropique, le modèle de polymer eight-chain. La déformation initiale de pré-phonation a été mesurée à l'aide d'un récent protocole de dissection et ajoutée à la mesure de déformation relative obtenue pendant la vibration des cordes vocales afin de calculer la contrainte totale. La cinématique de l'oscillation de ces cordes vocales a alors été comparée à celle de modèles synthétiques afin d'observer les similitudes et les différences.

Acknowledgment

Foremost, I would like to express my gratitude to my supervisor Prof. Luc Monneau for all his supports during my Ph.D, for his patience and immense knowledge. His being a mentor paved the way for me to explore new ideas in research. I appreciate the feedback offered by my co-adviser Prof. Rosaire Mongrain, and I would like to thank the rest of my thesis committee: Prof. Fariborz Alipour, Damiano Pasini, Richard Leask, Arun Misra for their encouragement and insightful comments.

Special thanks to Dr. Karen Kost and Dr. Nadine Yammie for performing the clinical experiments in Montreal General Hospital and I would like to express my appreciation to Dr. Carlose Torres for providing radiology data. My sincere thanks also go to Dr. Michael Ferreira and Dr. Bruce Pike for their help on designing and performing the MRI experiments.

I thank my fellow labmates and friends at Biomechanics lab: Dr. Alireza Najafi-Yazdi, Dr. Amir Kamal Miri, Dr. Hossein Khadivi Heris, Mostafa Najafi-Yazdi, Siavash Kazemi-Rad, Alfred Chan for all their helps and comments about my research. I would also thank undergraduate students Justin Yang, Leon Johnson, Nihal George, Liam Meade and Omar Elkayyali who helped me for designing the test set up and Christina Moro for 3D reconstructions.

Financial supports from NIH is gratefully acknowledged and the computational resources were provided by Compute/Calcul Canada through the CLUMEQ and the RQCHP High Performance Computing Consortia.

TABLE OF CONTENTS

1	Introduction	3
1.1	Overview	3
1.2	Background and literature review	5
1.2.1	Three-dimensional (3D) reconstruction of human vocal folds and laryngeal cartilages using CT scan data	5
1.2.2	Three-dimensional reconstruction of human vocal folds by mapping HSDI data and MRI images	7
1.2.3	Assessment of the quasi-steady approximation in glottal airflow	8
1.2.4	Numerical simulations of the airflow in subject-specific airway models	10
1.2.5	Determination of strain field on porcine excised larynges using DIC	12
1.3	Research objectives	14
1.4	Outline of the thesis	18
2	Three-dimensional reconstruction of human vocal folds and laryngeal cartilages using CT scan data	20
2.1	Introduction	20
2.2	Methods	21
2.2.1	CT scan data	21
2.2.2	Segmentation	21
2.2.3	Morphometric measurements	22
2.2.4	Surface treatment or mesh smoothing	22
2.3	Results	23
2.3.1	Laryngeal cartilages	23
2.3.2	Vocal tract and vocal fold models	27
2.4	Discussion	33
2.4.1	Comparison of morphometric measurements between 3D solid models and cadaver data	33

2.4.2	General laryngeal cartilage models	35
2.4.3	Vocal tract and vocal fold models	36
2.4.4	Limitation of the present study	36
3	3D reconstruction of human vocal folds by mapping HSDI data and MRI images	37
3.1	Introduction	37
3.2	Experiments	38
3.2.1	High speed digital imaging (HSDI)	38
3.2.2	Magnetic resonance imaging (MRI)	39
3.3	Image processing algorithm	40
3.3.1	Obtaining pixel size in HSDI images	40
3.3.2	Vocal folds edge detection and motion functions	43
3.3.3	Mucosal wave detection	43
3.3.4	Moving functions of the vocal folds' lower layers	46
3.3.5	Rewriting MRI data for intermediate geometry of vocal folds	50
3.4	Results	53
3.5	Discussion	54
4	Assessment of the quasi-steady approximation in glottal airflow	56
4.1	Introduction	56
4.2	Methods	57
4.2.1	Orifice profiles and wall motion	57
4.2.2	Numerical simulations	58
4.2.3	Mesh refinement	63
4.3	Results and discussion	64
4.3.1	Velocity profile and unsteady flow features	64
4.3.2	Pressure gradient	66
4.3.3	Wall shear stress	67
4.3.4	Flow rate	67
4.3.5	Orifice discharge coefficient	68
5	Numerical simulations of the airflow in subject-specific airway models . .	76
5.1	Introduction	76
5.2	Creation of solid models from CT scan	76
5.3	Numerical procedures	77
5.3.1	Lattice Boltzmann method	77

5.3.2	Computational setup	78
5.4	Results	83
5.4.1	Three dimensional models	83
5.4.2	Two dimensional model	87
5.5	Discussion	89
5.5.1	Orifice discharge coefficient	89
5.5.2	Flow asymmetry	92
5.5.3	Secondary flow	93
6	Determination of strain field on porcine excised larynges using DIC	96
6.1	Introduction	96
6.2	Methods	97
6.2.1	Sample preparation	97
6.2.2	Experimental apparatus	98
6.2.3	Digital image correlation	102
6.2.4	Determination of the initial pre-phonatory strain	105
6.3	Results and Discussion	108
6.3.1	Initial strain field on the vocal folds	108
6.3.2	Kinematics of vocal fold vibration	109
6.3.3	Impact stress assessment using an isotropic constitutive law	117
7	Concluding remarks and future work	121
7.1	Concluding remarks	121
7.1.1	Three-dimensional reconstruction of human vocal folds and laryngeal cartilages using CT scan data	121
7.1.2	Three-dimensional reconstruction of human vocal folds by mapping HSDI data and MRI images	122
7.1.3	Assessment of the quasi-steady approximation in glottal airflow	122
7.1.4	Numerical simulation of the airflow in subject-specific airway models	124
7.1.5	Determination of strain field on excised porcine larynges using DIC	124
7.2	Contributions to the voice research	126
7.3	Recommendations for future work	128
7.3.1	Assessment of the quasi-steady approximation in 3D-accurate models	128

7.3.2	<i>In vivo</i> digital image correlation analyses	128
7.3.3	Building subject-specific models of the larynx and vocal folds	129
A	Design details of laryngeal cartilages and engineering drawings	130
B	M5 model	137

LIST OF TABLES

2-1 Comparison of the morphometric features of 3D reconstructed model to those of Tayama <i>et al.</i> for Thyroid cartilage	24
2-2 Comparison of the morphometric features of 3D reconstructed model to those of Tayama <i>et al.</i> for Cricoid cartilage	25
2-3 Comparison of the morphometric features of 3D reconstructed model to those of Tayama <i>et al.</i> for Arytenoid cartilage	26
4-1 The number of elements in each refinement step and relative error between refinement steps	64
4-2 The discrepancy between the shear stress of the dynamic and static solutions	67
5-1 Inlet, outlet and glottis areas for both healthy and postsurgical geometries	79
5-2 Comparison between C_{ds} for different cases	90
5-3 Comparison between fluid resistances for different cases	92

6-1 Pre-strain in the vocal fold	108
--	-----

LIST OF FIGURES

1–1 Overall objectives of the present dissertation	14
2–1 3D reconstructed laryngeal framework from CT scan data: (a) thyroid (b) cricoid (c) arytenoid (d) laryngeal cartilage framework	23
2–2 Measurements definitions and landmarks: (a) thyroid (b) cricoid (c) arytenoid	29
2–3 Cross section view of 3D reconstructed vocal tract: (a) healthy larynx before smoothing (b) healthy larynx after smoothing (c) postsurgical larynx	30
2–4 Healthy larynx: (a) vocal tract model and (b) corresponding sagittal view	31
2–5 Post-surgery larynx: (a) Vocal tract model and (b) Corresponding sagittal view	31
2–6 Complete vocal tract: (a) 3D solid model (b) Corresponding sagittal view	32

3–1 Summary of the image processing method (1) pixel size calculation in HSDI images (2,3) vocal fold edge detection and extraction of the oscillation function of the edge points (4,5) mucosal wave detection and calculation of the mucosal wave propagation speed (6) overlapping HSDI images with the MRI data and estimating the oscillation functions of vocal folds' lower points (7) imposing the desired location of the vocal fold boundaries on the MRI images and creation of a new set of MRI data	41
3–2 Comparison between the anterior-posterior lengths of the vocal fold while performing similar tasks: (a) $L_M(m)$, the anterior-posterior length in an MRI image and (b) $L_H(Pixel)$, the anterior-posterior length in a high-speed image.	42
3–3 Image processing algorithm, Subject 1 phonating at 130 Hz: (a) pre-processed high-speed image, region of interest and non-vertical glottal midline; (b) magnified region of interest with vertical glottal midline; (c) binary image; (d) perimeter of the binary image, where boundaries represent the vocal fold edge; (e) the search window for mucosal wave detection, with obtained vocal fold edge overlapped on the gray scale image; (f) obtained mucosal wave overlapped on the gray scale image	44

3–4 The intensity gradient on a medial-lateral line passing through the vocal folds' midpoint. (a) Phonation frequency 130 Hz , mucosal wave peak was seen only on the right fold, (b) Phonation frequency 110 Hz , mucosal wave peak was seen on both folds	45
3–5 HSDI data shows the superior surface of the vocal folds. The lower layers of the vocal folds are visible in transverse MRI images. HSDI data was overlapped on the corresponding MRI transverse image at the location shown on the magnified box.	47
3–6 Overlapping HSDI and MRI images of vocal folds. The motion functions of the superior points S_i were obtained from the edge detection method on HSDI images. The motion functions of the lowe layers, L_i were obtained using the mucosal wave speed. Each of the lower layers corresponds to one MRI image in the inferior-superior direction	48
3–7 Schematic frontal view of the vocal folds. The amplitude of vibration was calculated for the edge points at different layers by comparing the fully closed and fully open shapes	50
3–8 (a) MRI image in the transverse plane at the level of the vocal folds (b) New boundaries of the vocal folds for an intermediate geometry were shown as hashed regions. The image intensity of the hashed regions was set to be equal to that of the adjacent points on the vocal folds	52

3–9 (a) 3D reconstructed geometry of vocal folds with the fully open shape (b) 3D reconstructed geometry of vocal folds from edited dicom data. Vocal folds have an intermediate configuration between fully closed and fully open.	53
4–1 Computational domain geometry with divergent vocal fold shape	59
4–2 Computational fluid streamlines in divergent shape (a) Dynamic simulation (b) Steady simulation	69
4–3 Computational fluid streamlines in parallel shape (a) Dynamic simu- lation (b) Steady simulation	70
4–4 Computational fluid streamlines in convergent shape (a) Dynamic simulation (b) Steady simulation	71
4–5 Convective and local accelerations for point A and B: $\cdots \circ \cdots$:Convective acceleration at A $\cdots \square \cdots$:Convective acceleration at B, $-$ Local acceleration at A, $\cdots :$ Local acceleration at B	72
4–6 Ratio of the local acceleration to the convective acceleration for point A	73
4–7 Glottal wall pressures for dynamic and static simulations at 14 virtual probes for divergent, convergent and parallel glottal shape	73
4–8 Flow rate vs. orifice angle over one cycle ■: static, $\cdots \circ \cdots$:Dynamic .	74
4–9 Orifice discharge coefficient over half a cycle model $- \circ -$: static , $\cdots \square \cdots$ dynamic	75
5–1 Computational domain for the healthy subject	80
5–2 2D computational domain on the (a) frontal (b) sagittal CT image . .	82

5–3 Velocity profile in shown on a mid-coronal and three transverse planes for (a) healthy (b) post-surgery geometry. Mid-coronal slice overlapped with streamlines for (c) healthy (d) post-surgery vocal folds	85
5–4 Velocity profiles in the mid-sagittal cross section (a)healthy geometry (b) post-surgery vocal folds	86
5–5 Velocity profile in (a) 2D cross section (b) corresponding slice of 3D simulation	88
5–6 Gauge pressure distribution along the inferior superior direction, Dash line (- -): 2D model, Dash dot line (.-): Open-shape, Solid line(-): post-surgery	91
5–7 V_y Velocity profile on the transverse plane at the glottis level and the velocity profile on the anterior-posterior line	95
6–1 Dissection of porcine larynx, (a) Dash-lines show the direction of dissection on the thyroid cartilage, (b) False folds in porcine larynx, (c) Cutting the false folds to reveal the vocal folds.	98
6–2 (a) Excised larynx set-up (b) Larynx holder	99
6–3 Schematic illustration of the excised larynx testbed	101
6–4 Pressure vs. flow rate for three porcine larynges	102
6–5 The chemical colors used in the experiment and the outcome results .	104
6–6 Vocal folds with a layer of speckle pattern with the contour of depth position on the superior surface of vocal fold and inspection lines in both anterior-posterior and medial-lateral direction.	105

6-7 (a) Larynx before after cut showing dissection path, (b)-(c) The larynx before cut	107
6-8 (a) Variations of W along the anterior-posterior during closing and (b) Variations of U along the anterior-posterior during opening (c) Variation of W along the medial-lateral inspection line during opening phase of oscillation	111
6-9 (a) Time history of displacement of the vocal fold midpoint, (b) Elliptical trajectory of midpoint	112
6-10 Contours of normal strain on deformed superior surface of vocal fold for (a) Open state and (b) Close state of vocal folds	114
6-11 Strain-time history	115
6-12 Normal strain vs flow rate at vocal fold midpoint (a) ϵ_{xx} (b) ϵ_{yy} . . .	116
6-13 U , W , ϵ_{xx} , and ϵ_{yy} , over four cycles	117
6-14 A-B) Distribution of the normal stress σ_{xx} on deformed surface of vocal fold at closing position based on dynamic strains and dynamic strain with pre-strain,respectively; C-D) Distribution of the normal stress σ_{xx} on deformed surface of vocal fold at closing position based on dynamic strains and dynamic strain with pre-strain,respectively. E) Distribution of the normal stress σ_{xx} on deformed surface of vocal fold at opening position. F) Distribution of the normal stress σ_{yy} on deformed surface of vocal fold at opening position	120
A-1 Engineering drawings of standard thyroid cartilage model	132
A-2 Engineering drawings of standard cricoid cartilage model	133

“Success is about what you are doing for yourself, but significance, is about what you are doing for others ”

– John Maxwell

Nomenclature

Abbreviation

<i>ALE</i>	Arbitrary Lagrangian-Eulerian
<i>BDF</i>	Backward Differentiation Formula
<i>CFD</i>	Computational Fluid Dynamics
<i>CT</i>	Computed Tomography
<i>DIC</i>	Digital Image Correlation
<i>DOF</i>	Degrees of Freedom
<i>FE</i>	Finite Element
<i>FSI</i>	Fluid Structure Interaction
<i>HSDI</i>	High Speed Digital Imaging
<i>MRI</i>	Magnetic Resonance Imaging

Greek Symbols

Ψ	Orifice included angle
ϵ_{0xx}	Initial strain in the medial-lateral direction
ϵ_{0yy}	Initial strain in the anterior-posterior direction
ϵ_{xx}	Strain in the medial-lateral direction
ϵ_{yy}	Strain in the anterior-posterior direction
σ_{xx}	Normal stress in the medial lateral direction
σ_{yy}	Normal stress in the anterior posterior direction
ω	Angular velocity of the wave
τ	Relaxation time, see eq 5.2
ν	Kinematic viscosity, see eq 5.2
μ	Air viscosity

Roman symbols

A	Area of the frontal cross section of the vocal fold see Appendix B
A_{L_i}	Oscillation amplitude of the i^{th} layer
A_m	Minimum area, see eq 4.7
AT_i	Absolute tolerance for DOF i see, eq 4.3
c_m	Mucosal wave propagation speed
D	Channel width in Chapter 4
E_i	Error estimated by the solver, see eq 4.3
f	Frequency of oscillation
$f_i(\mathbf{x}, t)$	Single-particle distribution function at position \mathbf{x} , see eq 5.1
$f_i^{eq}(\mathbf{x}, t)$	Equilibrium state, see eq 5.1
$I(x, y)$	Image intensity
L_H	Anterior-Posterior length of vocal folds in high-speed digital imaging data
L_i	MRI transverse images that show the vocal folds
L_M	Anterior-Posterior length of vocal folds in MRI images
MF	Moving Function of lower layers of the vocal folds
$MW(x, y)$	Mucosal Wave peak location in high-speed imaging data
N	Number of HSDI frames in which the vocal fold midpoint moves between the fully closed and fully open phase
N_d	Number of degrees of freedom see eq 4.3
P	Pressure
Q	Volume flow rate
R	Relative tolerance see eq 4.3
R_f	Flow Resistance see eq 4.7
Re	Reynolds number
s	Arc length in the direction of the wave propagation
S_i	Vocal fold physical points on the superior surface of the vocal folds edge that are visible in HSDI data
St	Strouhal number
SR	Sampling Rate of high-speed imaging
S^{dy}	Shear stress on the vocal from the dynamic simulation
\bar{U}	Inlet average velocity
U	Displacement amplitudes of the vocal fold physical points in the medial-lateral direction
\mathbf{u}	Velocity vector, see eq 4.2
$VF(x, y)$	Vocal fold edge as a function high-speed imaging data
\bar{V}_{edge}	Average edge velocity of the midpoint in the medial lateral direction
ΔVF	Edge displacement of the midpoint between the fully closed and fully open phase
VR	Variable Resolution
w_i	Weighting parameters for D3Q19 model, see eq 5.6
W	Displacement amplitudes of the vocal fold physical points in the inferior-superior direction

CHAPTER 1

Introduction

1.1 Overview

Voice production and speech play an essential role in communication and expressing emotions in human life. Based on statistics from the National Institute on Deafness and other Communication Disorders (NIDCD), approximately 7.5 million people in the United States have trouble in using their voice. The importance of treatments for and research into voice disorders is clear. The physics of voice production consists of the geometry of the larynx, vocal folds and vocal tract, the aerodynamics of the airflow within the larynx, and the mechanical properties of the tissues and muscles involved in vocal fold self-oscillation. All physical aspects of phonation fall within the scope of engineering analysis, revealing the importance of experimental and computational engineering investigations. Numerous computational and experimental analyses have been performed to investigate the mechanism of phonation. Mittal et al. (2013) presented a comprehensive review of the experimental and computational studies and findings related to the fluid dynamics of human phonation. Most vocal pathologies are related to biomechanical dysfunctions, which can change vocal folds' geometry, mechanical properties or kinematics (Mittal et al., 2013). For instance, the condition known as "breathy voice" has the biomechanical origin of incomplete glottal closure, and vocal fold nodules emanate from

excessive vocal folds contact stress (Mittal et al., 2013). Therefore, engineering models that consider the biomechanical aspects of voice disorders are becoming essential for treatments. Recently, a strong interest in subject-specific models has developed, and these are becoming indispensable in voice research. Subject-specific models consider person-to-person differences in the voice production parameters (i.e., geometry, aerodynamics and structure); consequently, they provide more accurate results with higher potential for clinical applications.

To create an accurate subject-specific model of voice production, the physical aspects of phonation-geometry, aerodynamics, and mechanical properties-should be taken into account. The geometry of voice production comprises the vocal tract, larynx, vocal folds, laryngeal framework cartilages and trachea. Depending on which phonation parameters are to be analyzed, some of these parts may be included or excluded. For instance, to simulate the airflow within the larynx, the geometries of the trachea, vocal tract, and vocal folds are used. However, to estimate the impact stress between the vocal folds, only the vocal fold geometry is needed. The second parameter is the fluid dynamics of the air passing through the larynx, the glottis and the vocal tract, which determines the aerodynamic forces on the vocal folds. Fluid dynamics of the airflow inside the larynx directly defines the acoustics field in the vocal tract. The third aspect of phonation encompasses the mechanical properties of the vocal folds which determines the response of the tissue to the aerodynamics forces applied by the airflow. These three aspects together governs the FSI between airflow and the vocal folds and produce the self-sustained oscillation of the vocal folds.

In the present dissertation, the mentioned aspects were taken into account to pave the way toward obtaining a realistic, non-expensive, human-specific model of the larynx and vocal fold for analyzing voice production. Considering the geometry component of voice production, a 3D reconstruction of the vocal folds, larynx and laryngeal cartilages was performed. A methodology for creating 3D geometries of vocal folds with a desired glottal angle is introduced. To investigate glottal airflow, the quasi-steady approximation in a 2D model was assessed. Furthermore, 3D simulations of airflow in subject-specific models were performed. Finally, to investigate the deformation of vocal folds, excised larynx experiments were performed and the strain-stress field on the superior surface of the vocal folds was calculated.

1.2 Background and literature review

1.2.1 Three-dimensional (3D) reconstruction of human vocal folds and laryngeal cartilages using CT scan data

Realistic biomechanical laryngeal models are gaining value in clinical applications and research related to laryngeal disorders. These models are beneficial for examining several phonation aspects such as aerodynamics, acoustics, vocal fold vibrations, kinematics of cartilage motion and mechanical properties of vocal fold tissue. In the medical field, they can be used for surgical planning and analysis of laryngeal anomalies (Tayama et al., 2001). Of particular importance is the morphology of the laryngeal framework, which along with the action of muscles and their locations, determines cartilage motion and consequently the vocal folds postures (Tayama et al., 2001). As a result, to create a realistic 3D laryngeal model, accurate anatomical data on laryngeal cartilages and vocal fold geometry are needed.

Computer Tomography (CT) scan images have been used to create realistic 3D vocal fold and vocal tract geometries for the purpose of studying laryngeal anomalies. For instance, the asymmetry of vocal folds in patients with immobility (Oyamada et al., 2005) and unilateral vocal fold paralysis before and after treatment (Hiramatsu et al., 2008) have been studied. However, according to literature, 2D or simplified 3D vocal folds and vocal tract geometries have been used for computational fluid dynamics (CFD), finite element (FE) and FSI simulations. Less attention has been paid to the creation of realistic vocal fold and vocal tract models for computer simulations. Gökcan et al. (2010) used accurate geometries made from CT scan data for CFD analysis. Šidlof et al. (2008) used plaster castings to capture the vocal fold profiles from excised human larynges. In this approach, the geometry of the excised larynx is not very realistic, because the thyroarytenoid muscle is not active.

Eckel et al. (1994); Tayama et al. (2001); Sprinzl et al. (1999); Eckel & Sittel (1995) have reported morphometric measurement data of the laryngeal framework of cadaver larynges. CT scans and MRI have been used to create 3D computer models of laryngeal cartilages (Chen et al., 2011; ?; Selbie et al., 2002). However, having the dimensions of the complex cartilage geometries is insufficient for recreating the laryngeal cartilage framework. Furthermore, the previous efforts for defining general laryngeal framework are not repeatable unless one has access to the specific CT or MRI data used, and the same segmentation steps from the previous studies should be precisely followed.

1.2.2 Three-dimensional reconstruction of human vocal folds by mapping HSDI data and MRI images

Despite recent progress on simulation of the voice production FSI problem, challenges in the simulation of voice production persist in the areas of boundary conditions of vocal fold vibration, accurate parametrization of the tissue properties of vocal folds, computational modeling of the vocal folds contacts, and the complex vocal folds geometry (Mittal et al., 2013). Evaluation of the quasi-steady approximation in 3D glottal airflow is therefore critical. For this, 3D geometries of the vocal folds at different glottal angles during one complete cycle are needed. Vocal folds configurations include fully closed, fully open and the intermediate geometries with divergent, convergent or parallel glottal angles. The MRI and CT images used for 3D reconstruction of vocal folds and laryngeal framework cartilages belong to one specific moment; as a result, the reconstructed geometries represent one specific shape of the vocal fold. To create geometries of the vocal folds with different shapes, HSDI data from the superior surface of the vocal folds with a very high temporal resolution (4000 frames per second) were overlapped with MRI images. Using image processing methods, the vocal fold edges and mucosal wave peaks were detected and moving functions of the vocal folds edges were calculated. The moving functions of the lower layers in the inferior-superior direction were also calculated using wave propagation methods. The MRI images were then revised and new image series were produced. The reconstructed 3D geometries from the new MRI data correspond to the desired shape of the vocal fold.

High speed digital imaging has been widely used in voice research and its clinical applications are reported in previous studies (Zhang et al., 2011; Deliyski et al.,

2008; Deliyski & Hillman, 2010; Bhandari et al., 2012). The review paper by Kendall (2012) presents the recent advances in HSDI of the larynx and vocal folds and its clinical applications. Several methods have been suggested to demarcate the vocal fold edges (Yan et al., 2006; Lohscheller et al., 2007; Zhang et al., 2010). Mucosal wave propagation has been assessed clinically by different measurement techniques such as electrography, photoglottography, ultrasound and visualization techniques including videokymography, stroboscopy and high speed imaging (Boessenecker et al., 2007; George et al., 2008; Voigt et al., 2010; Krausert et al., 2011). Krausert et al. (2011) investigated the advantages and disadvantages of each technique. Boessenecker et al. (2007) characterized mucosal wave properties using an excised human hemi-larynx. Thirty microsutures were uniformly placed over the medial and superior surfaces of the vocal fold. The surface kinematics were studied by high-speed recording of the vocal fold oscillation and tracing the trajectory of the microsutures across a range of phonatory conditions. George et al. (2008) studied the generation and propagation of mucosal waves. They used a laser-triangulation endoscope and high-speed cameras to capture the human vocal folds profile during vibration *in vivo*. Voigt et al. (2010) presented a detection algorithm for mucosal wave propagation using HDSI.

1.2.3 Assessment of the quasi-steady approximation in glottal airflow

Phonation is a direct by-product of airflow through the glottis and the associated vocal fold vibrations. Because of FSI during phonation, the vocal folds undergo 3D oscillations at frequencies around 100-200 Hz for normal phonation. Realistic computational models of voice production describing the complex flow-induced oscillations

are computationally expensive, and simplification assumptions are needed. For instance 2D geometries have been used to model the actual 3D glottal airway (Alipour & Scherer, 2004; Alipour et al., 1996b; Scherer et al., 2001; Zhao et al., 2002; Šidlof et al., 2008). Driven models, with imposed wall motion eliminate the need to take FSI into consideration (Krane et al., 2010; Mongeau et al., 1997; Barney et al., 1999; Kucinschi et al., 2006; Park & Mongeau, 2007; Krane et al., 2007). Quasi-steady approximation is often used in voice production simulations e.g (Pelorson et al., 1994). It models unsteady fluid flow through a time-varying orifice as a series of steady flows through fixed orifices, with configurations and boundary conditions instantaneously the same as for time-varying cases at specific time values. In other words, the contribution of time-dependent terms in the equations of fluid motion is assumed negligible. The quasi-steady approximation may lead to a significant decrease in computational cost by converting a dynamic problem into a sequence of static problems that are much easier to simulate.

Contradictions in the previous studies highlight the need for further investigations. Experimental verifications of quasi-steady approximation have been reported. Zhang et al. (2002) built a dynamic mechanical model of the larynx and investigated the validity range of the quasi-steady approximation. The dynamic-model results were compared to predictions based on the quasi-steady approximation, and good agreement was obtained between the two sets of data for a range of operating frequencies, flow rates and orifice shapes. It was concluded that the quasi-steady approximation is valid for the tonal component of sound generated by pulsating confined jets. Vilain et al. (2004) presented a theoretical description of glottal flow based

on quasi-steady boundary layer theory and performed experimental verifications of the quasi-steady approximation. Other theoretical and experimental studies have reported that unsteady fluid flow effects are significant and time-dependent terms cannot be ignored, as postulated by the quasi-steady approximation. In a theoretical assessment of aerodynamic effects in phonation, Krane & Wei (2006) identified two temporal regimes. The first one is dominated by unsteady effects, local fluid acceleration and acceleration induced by the vocal fold walls. The second temporal regime is the interval over which flow behavior is quasi-steady. Measurements of fluid flow through a scaled-up model of the human glottis have been performed by Krane et al. (2007) to investigate unsteady glottal flow. According to this study, flow through the moving vocal folds is significantly different from that through the non-moving glottis; however the reciprocating motion of the rigid model used, may have exacerbated unsteady flow contributions.

1.2.4 Numerical simulations of the airflow in subject-specific airway models

Experiments measuring the aerodynamic parameters of human or excised larynges are difficult because of the lack of space and the high frequency of vocal folds motion. Furthermore, *in vivo* experiments are mostly invasive. As a result, several experimental and computer models have been made to investigate different aspects of voice production. Mittal et al. (2013) present a comprehensive review of the experimental and CFD studies. Scherer et al. (2010) used a physical model to investigate intraglottal pressure. They also made a 3D computer glottal model, from which aerodynamic parameters were calculated and compared to those of the physical model. Park & Mongeau (2007) evaluated the quasi-steady approximation using life-scale

convergent and divergent glottis-shape rubber models. They compared the orifice discharge coefficients of the steady jets from fixed orifices with those of unsteady jets from modulated orifices.

Computational simulations of glottal airflow, vocal fold vibration and the interaction airflow and vocal folds also provides insight into phonation. Major advancements in the ability to simulate complex models, encouraged many researchers to perform simulations based on 3D rather than 2D simplified models (Zheng et al., 2010; Gökcan et al., 2010; Zheng et al., 2011b; Becker et al., 2009). Zheng et al. (2010, 2011b) performed two- and three-dimensional FSI simulations of the glottal jet flow. The 2D computational domain was extracted from a coronal CT scan image and the 3D geometry was made by extrusion of the 2D geometry. A 3D finite element model was used by de Oliveira Rosa & Pereira (2008) to calculate the glottal airflow velocities and pressure. They also investigated the effects of false folds dimensions as well as glottal shape and area on the airflow. Gökcan et al. (2010) performed a computational study on the airflow for patients with bilateral abductor vocal fold immobility. They developed 3D geometries of the normal and pathological larynges from CT scan data and investigated how changes in geometry from loss of muscular tonus affected aerodynamics of glottal airflow (Gökcan et al., 2010). The asymmetry of vocal folds in patients with immobility Oyamada et al. (2005) and unilateral vocal fold paralysis before and after treatment Hiramatsu et al. (2008) were studied using 3D laryngeal geometries made from CT scan data.

1.2.5 Determination of strain field on porcine excised larynges using DIC

Vocal abuse, misuse, and overuse are postulated to be the etiology behind common vocal fold pathologies, including nodules, cysts and polyps (Johns, 2003). These benign lesions may cause hoarseness, throat discomfort and pitch breaks. It is believed that benign lesions on vocal folds are caused by contact and trauma during normal or pressed phonation (Roy et al., 2005). A better understanding of the mechanics of phonation is required to design proper treatments for vocal fold pathologies. To yield this understanding, a detailed knowledge of stress and strain during vocal fold vibration is needed. Mechanical stresses acting on vocal fold tissue during phonation include shear, aerodynamic, tensile, compression and inertial stresses. These cause 3D deformations during vocal fold vibration (Titze, 1994). Determining the deformation over a surface using a constitutive model allows the calculation of the stress components over that surface. Stress and strain data obtained from experiments on excised larynges can be compared with the corresponding parameters obtained from computer models, thus providing a framework for verifying computer simulations.

Impact stress generated by the collision of vocal fold tissue is believed to be the strongest contributor to voice trauma (Gray & Titze, 1988). High impact stresses are believed to cause the formation of nodules, polyps and cysts; however, the absence of a reliable and accurate method to measure vocal fold deformations hampers the development of quantitative metrics. Many approaches have been introduced to determine stress and strain fields (Spencer et al., 2008), including excised-larynx experiments (Jiang & Titze, 1994; Verdolini et al., 1998; Jiang et al., 2001), physical

rubber models (Spencer et al., 2008; Chen & Mongeau, 2011), human in-vivo measurements (Hess et al., 1998; Verdolini et al., 1999; Gunter et al., 2005) and FE based simulations (Gunter, 2003; Tao et al., 2006; Helm et al., 1996). For instance, Jiang & Titze (1994) measured impact stresses using surface-pressure measurements in excised canine hemilarynges. Verdolini et al. (1998) used the electroglottography close quotient (EGG CQ), the ratio of the time during which the glottis is closed to the oscillation period, as a noninvasive estimate of vocal fold impact stress in excised canine larynges. Jiang et al. (2001) compared vocal fold acceleration with the simultaneously measured impact stresses. The second derivative of the photoglottography (PGG) data was used to obtain vocal fold acceleration, which is expected to be proportional to the impact stress. Their experimental setup included a pressure transducer that was placed between the vocal folds during phonation to measure the impact stress at the mid-glottal location. Spencer et al. (2008) used DIC to determine the strain field on the superior surface of a self-oscillating physical replica of the human vocal folds . They estimated the distribution of the contact pressure on the medial surface using superior surface strains and a Hertzian contact model. Chen & Mongeau (2011) developed a microphone coupler attached to a probe, with 0.64-mm outer diameter, to noninvasively measure the contact pressure between the two colliding sides of a synthetic silicone replica of the human vocal folds. They also created a finite element model of the replica and compared the results with empirical and predicted results from a Hertzian impact model.

1.3 Research objectives

Figure 1–1 shows the objective and the specific goals of the present dissertation. The overall objective was to develop computer models that can be used to create subject-specific models of human larynx and vocal folds.

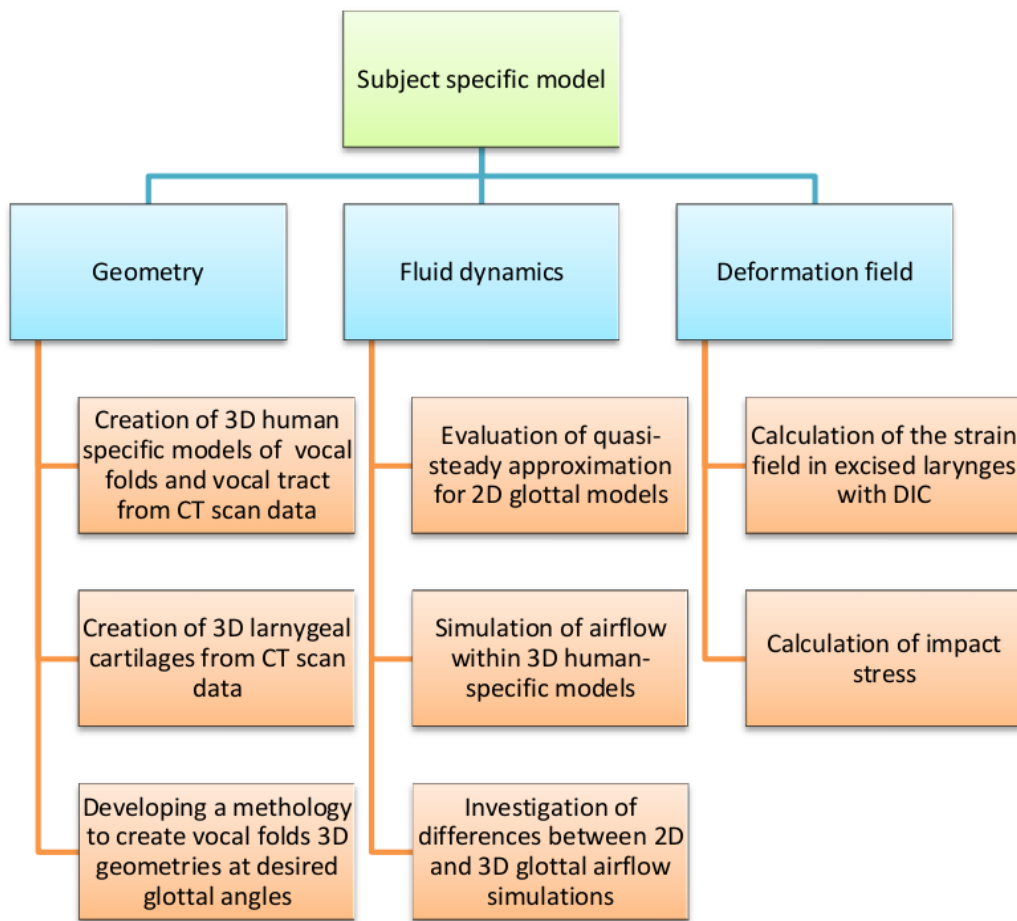


Figure 1–1: Overall objectives of the present dissertation

The first goal was to create accurate subject-specific geometries of vocal folds, vocal tract and laryngeal cartilages using CT scan and MRI data. Manual and automatic image segmentations were performed on depersonalized CT scan data to create 3D models of the larynx. Subject-specific 3D models of the vocal folds and vocal tract during phonation and respiration were created and geometrical differences were investigated. Geometries of thyroid, cricoid and arytenoid cartilages were reconstructed, and biomechanically important dimensions of the generated cartilages were compared with previously reported cadaver measurements, Tayama et al. (2001), to evaluate the precision of the segmentation procedure. Mesh smoothing and surface treatment methods were used to remove any artifacts and sharp edges that could affect the convergence of computational simulations.

The second goal was to create “general cartilage models” that can be used for computational simulations. Preserving all biomechanically important dimensions, CT scan based cartilage geometries were recreated using known geometrical features in modeling softwares. The “general cartilage models” are accessible, subject independent and can be considered as generic laryngeal cartilage geometries that can be used for further simulations.

The third goal was to develop a methodology to create accurate 3D vocal folds geometries at a desired glottal angle covering one oscillation cycle. This was done by overlapping the MRI/CT images with HSDI data of the superior surface of the vocal folds. A threshold based image processing method was used to demarcate the vocal fold edges and the mucosal wave peaks. Using wave propagation methods and mucosal wave propagation speed, the moving functions of different layers of the vocal

folds in the inferior-superior direction were obtained and MRI images rewritten to create the new sets of data corresponding to the specific vocal fold shape desired (e.g., fully open, fully closed, or a geometry with an intermediate glottal angle).

The fourth goal was to further evaluate the accuracy of the quasi-steady approximation through comparisons between the aerodynamic parameters of the dynamic simulation and the results for the corresponding orifice shape in a steady-state solution. A 2D driven model of the larynx was used. Simulations were performed using COMSOL multiphysics[®] software. Details of the dynamic and static model setups, such as glottal geometry, the simulation methods and boundary conditions, were presented. The velocity field, the pressure and shear stress on the vocal folds surface, flow rate, and orifice discharge coefficients were compared for static and dynamic solutions to assess the accuracy of the quasi-steady approximation.

The fifth goal was to perform fluid flow simulations in subject-specific 3D models created from CT scan data. The increased availability of high-performance computational resources allows the creation of computer models that are more detailed and based on the anatomy of individual subjects. CT scan data were used to create 3D solid models of the vocal folds and the larynx. CT scan or MRI data supply more accurate subject-specific geometries in comparison with excised larynges. In addition, computer analysis of a series of 2D images is much more convenient than working with cadavers. Numerical simulations of fluid flow were performed using accurate geometries and aerodynamic parameters were compared for different glottal shapes. Differences between 2D and 3D simulations and the 3D nature of the glottal airflow were investigated. Powerflow[®], a commercially available parallel code based on

the Lattice-Boltzmann kernel, was used for the numerical simulations. The 2D vocal fold profile extracted from CT scan images is used for 2D simulation. The results from the 2D and 3D simulations were compared at a location corresponding to the simulated 2D slice used for creating the 2D vocal fold profile.

The sixth goal was to determine the impact stress between the vocal folds using digital image correlation (DIC) and excised porcine larynges. The objective was to develop an accurate, easy-to-use and noninvasive method for the measurement of the deformation field over the superior surface of the vocal fold tissue. An excised larynx test bench, equipped with two high-speed digital cameras for optical measurements and a regulated airflow supply, was used. Several porcine larynges ($n=4$) were used in flow-induced, self-oscillation experiments. The vocal fold surface was covered with a speckle pattern made of graphite powder. The 3D deformation field on the superior surface of the vocal folds was then determined from recorded digital images using DIC. Vocal folds are initially under tension because of their natural geometry in the laryngeal framework. Additional tension was applied on the vocal folds mounted on the setup to yield the proper self-oscillation. Therefore, the read-out strain fields are biased because of the initial prephonatory strain, hereinafter called “initial strain.” A unique dissection protocol was introduced and used in the experiments to evaluate the initial strain field. The kinematics of the vocal folds was investigated to study the vibratory characteristics, the homogeneity of the deformation and the time-dependency of displacement components. Finally, an estimation

of the impact stress was computed using the effective strain field—that is, the summation of relative strain calculated by DIC plus initial strain—and an eight-chain constitutive model adapted from previous studies on polymers (Miri et al., 2012b).

1.4 Outline of the thesis

Chapter 2 describes the 3D reconstruction of the vocal fold, vocal tract and laryngeal cartilages from CT scan data. The procedure for the creation of the general models is also described and engineering drawings of these models is presented in appendix A. The feasibility of using CT scan data for the creation of 3D solid laryngeal models along with the advantages, disadvantages and limitations of doing so are discussed. Chapter 3 introduces the image processing methods for overlapping the HSDI data with MRI images to capture the motion functions of the vocal folds. The procedure of rewriting MRI images related to the desired glottal shape is described and 3D models of vocal folds in different configurations are presented.

In Chapter 4, evaluation of the quasi-steady approximation for a 2D driven model is presented. Comparisons between a dynamic simulation and a series of static simulations with instantaneous identical orifice angles are presented and aerodynamic parameters are compared. The validity of this approximation and its limitations are discussed.

Chapeter 5 reviews the computational simulation of airflow within 3D reconstructed models created in Chapter 2 using Lattice Boltzmann method. Aerodynamic parameters within healthy and post-surgery geometries are compared and the similarities and differences are scrutinized . Furthermore, similarities and differences between a 2D and 3D glottal airflow simulations are discussed.

In Chapter 6, the excised larynx experiment and the DIC method to calculate the strain field on the superior surface of the porcine vocal folds are explained. The estimated impact stress and the comparison with previous results are discussed. Finally, Chapter 7 reviews the principal findings of this study and suggests directions for future work.

CHAPTER 2

Three-dimensional reconstruction of human vocal folds and laryngeal cartilages using CT scan data

2.1 Introduction

Three-dimensional (3D) computer models of the human larynx are useful tools for research and for eventual clinical applications. Recently, CT scanning and MRI have been used to recreate realistic models of human larynx. In the present Chapter, CT scan images were used to create computer models of vocal folds, vocal tract, and laryngeal cartilages and the procedure to create solid models was explained in details. Vocal folds and vocal tract 3D models of healthy and post-surgery larynges during phonation and respiration were created and morphometric parameters were scrutinized. The laryngeal framework of eight patients was also reconstructed from CT scan images and assessed for accuracy. That means for each cartilage, morphometric landmarks were measured on the basis of their importance for biomechanical modeling. A quantitative comparison was made between measurement values from the reconstructions and those from human excised larynges in literature. Low discrepancies between these measurements indicates the feasibility of using CT scan data for creation of 3D models. General models of the laryngeal framework were created using known features in modeling softwares. They are created based on the morphometric landmark dimensions previously defined and all biomechanically important dimensions were preserved. These models are accessible, subject independent, easy

to use for computational simulations and make the comparisons between different studies possible.

2.2 Methods

2.2.1 CT scan data

In the present study, data from 12 anonymous subjects were provided from the Montreal General Hospital, however only 8 were used. Three data sets were discarded on the basis of very poor grey level intensity contrast between cartilage and surrounding soft tissue and poor resolution. Another set was deemed inadequate due to movement of the patient during the scanning process. All data were related to male subjects. One set of the CT data was related to post-surgery images for a patient with cancer. No more information about the images was available on the data. There are differences between the CT imaging settings from one case to another. However the criteria for including and excluding one set of data is the grey level intensity contrast between the region of interest and its surroundings.

2.2.2 Segmentation

Segmentation was done using an open-source software, ITK-Snap Yushkevich et al. (2006), which permits simultaneous tri-axial display of the sagittal, coronal and transverse medical images, as well as a 3D view of the segmented structure. A semi-automatic segmentation procedure was used, based on ITK-Snap's region-based sectioning method (Yushkevich et al., 2006). The grey level intensity interval for each geometry was determined by displacing the crosshairs on the input image in the region of interest. The upper and lower thresholds were input into the “pre-process image” window, and smoothness was set to maximum.

In order to minimize time consumption and user error, the segmentation process was first done using ITK-Snap's automatic segmentation feature. The intensity contrast between air and tissue is high in CT images. Therefore, vocal folds and vocal tract boundaries could be well visualized and no manual editing was required. However, manual segmentation tools were used in some cases to edit the cartilage structures after automatic segmentation. For instance, certain elements of the arytenoid and cricoid cartilages could not be well visualized in CT scan images, especially those composed of elastic cartilage such as the arytenoid apices (Mupparapu & Vuppalapati, 2005).

2.2.3 Morphometric measurements

The STL (Stereolithography) files created from ITK-Snap were converted into solid bodies in Solidworks[®] using the Surface Wizard from the Scan to 3D add-in. Dimensioning was computed according to the morphometric measurements defined by Tayama et al. (2001) for the purpose of biomechanical modeling.

2.2.4 Surface treatment or mesh smoothing

Surface treatment was necessary to eliminate the sharp edges and artifacts from 3D reconstructed geometries, as they can affect the convergence of CFD or FE simulations. *Meshlab*, the open source software for processing and editing of unstructured 3D triangular meshes was used. Several different mesh smoothing methods are available in the software and among them, best results were obtained by using the Laplacian smoothing method. More details about Laplacian smoothing method can be found in (Field, 1988).

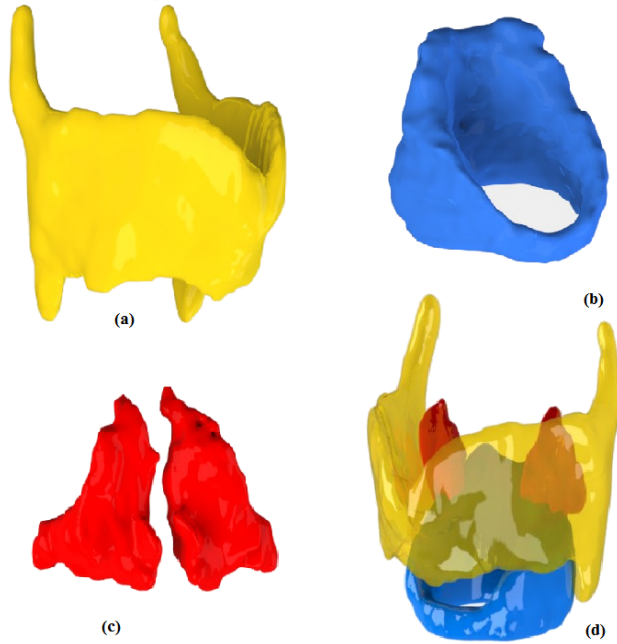


Figure 2–1: 3D reconstructed laryngeal framework from CT scan data: (a) thyroid (b) cricoid (c) arytenoid (d) laryngeal cartilage framework

2.3 Results

2.3.1 Laryngeal cartilages

3D reconstructed models and morphometric measurement

The 3D reconstructed cartilages from one set of CT scan images are shown individually and assembled in figure 2–1. All measurement definitions and landmarks are schematically shown in figures 2–2(a), 2–2(b) and 2–2(c). The results of the morphometric measurements performed on the segmented thyroid, cricoid and arytenoid cartilages are recorded in tables 2–1, 2–2 and 2–3, respectively.

The number of models associated with each measurement varied between cartilages and landmark points. One thyroid was excluded due to physiological anomalies.

Thyroid	Present study			Tayama <i>et al.</i>		Diff (%)
	Mean	S.D	Num	Mean	S.D	
Superior cornu, Left to Right ($A - A'$)	37.55	7.30	6	35.5	7.75	5.79
Superior to inferior cornu, Left ($A - B$)	47.17	3.87	6	46.38	4.58	1.70
Superior to inferior cornu, Right ($A' - B'$)	45.22	7.90	7	43.07	7.37	4.98
Left to right width of posterior edges, midvertical ($1 - 1'$)	44.47	4.02	7	41.65	2.82	6.77
Anterior thyroid notch to inferior border ($D - D'$)	19.77	1.59	7	19.24	0.79	2.75
Superior thyroid seam thickness ($D' - C'$)	3.69	0.60	7	4.13	0.38	10.65
Inferior thyroid seam thickness ($D - 2$)	3.32	0.43	7	3.68	1	9.89
Anterior to posterior length, bottom (inside $2 - 2'$)	27.30	1.59	7	29.7	4.62	8.08
Inferior cornu, Left to Right ($B - B'$)	31.33	3.27	7	34.8	4.06	9.97
Laryngeal prominence to posterior edges ($C - C'$)	34.32	1.37	7	37.27	4.52	7.91
Angle between thyroid laminae (α)	64.51	7.70	7	77.17	10.15	16.41
Angle between seam and cornu (θ)	34.96	3.20	7	35.22	3.46	0.75
Average percent difference						7.14%

Table 2–1: Comparison of the morphometric features of 3D reconstructed model to those of Tayama *et al.* for Thyroid cartilage

Two arytenoids could not be accurately segmented due to low visibility in the CT scan images. Moreover, the joint facets proved to be the most difficult features to observe. This may be due to the differences in joint physiology and its soft tissue percentage which is difficult to see using computed tomography (Windisch *et al.*, 2010). For each morphometric landmark, the mean and standard deviation were calculated. The accuracy of the segmentation procedure was verified by calculating the relative difference between the results from Tayama *et al.* and the results from

Cricoid	Present study			Tayama <i>et al.</i>		Diff (%)	
	Mean	S.D	Num	Mean	S.D		
Anterior arch, superior-inferior height ($I - I'$)	7.28	2.21	8	7.05	1.02	3.25	
Anterior arch, anterior-posterior thickness (mid-height,G)	3.53	0.80	8	3.16	0.72	11.86	
Posterior wall, superior-inferior height ($F - F'$)	27.47	study	3.40	8	22.69	1.68	21.05
Posterior wall, left to right width (at CT facets, 5 – 5')	30.99	4.51	8	29.86	2.59	3.78	
Inside diameter, anterior-poster (cranial edge, 6 – 6')	30.90	2.12	8	29.36	2.87	5.24	
Inside diameter, anterior-posterior (caudal edge, 7 – 7')	21.78	2.55	8	20.44	2.67	6.56	
Inside diameter, left to right (cranial edge, 8 – 8')	18.11	2.13	8	18.26	1.23	0.80	
Inside diameter, left to right (caudal edge, 9 – 9')	21.10	2.40	8	22.38	1.43	5.73	
Cricothyroid articular facet, major diameter (1â2)	6.14	0.23	4	6.15	1.12	0.18	
Cricothyroid articular facet, minor diameter (3-4)	4.99	0.15	4	4.73	0.72	5.59	
Cricoarytenoid articular facets, major diameter (J-M)	7.28	0.65	6	8.04	0.74	9.43	
Cricoarytenoid articular facets, minor diameter (O-N)	4.01	0.40	6	4.07	0.36	1.38	
Average percent difference						6.24%	

Table 2–2: Comparison of the morphometric features of 3D reconstructed model to those of Tayama *et al.* for Cricoid cartilage

the present study. An average percent difference is shown in the last row of each table.

Arytenoid	Present study			Tayama <i>et al.</i>		Diff (%)
	Mean	S.D	Num	Mean	S.D	
Vocal process to muscular process (R-S)	12.90	0.91	6	15.53	1.23	16.96
Vocal process to apex (R-Q)	16.31	1.18	6	17.51	2.08	6.85
Muscular process to apex (S-Q)	17.45	1.25	6	18.03	1.12	3.24
Cricoarytenoid facet, major diameter (W-V)	6.31	0.37	6	6.05	0.44	4.32
Cricoarytenoid facet, minor diameter (T-U)	5.07	0.50	6	5.87	0.47	13.71
Vocal process to cricoarytenoid facet center (R-X)	8.72	1.31	6	12.36	1.36	29.47
Muscular process to cricoarytenoid facet center (S-X)	5.28	0.75	6	5.18	1.13	1.95
Apex to ccricoarytenoid facet center (Q-X)	14.83	1.31	6	14.84	1.4	0.09
Average percent difference						9.57%

Table 2–3: Comparison of the morphometric features of 3D reconstructed model to those of Tayama *et al.* for Arytenoid cartilage

General laryngeal cartilage models

Although important research has been done on the morphology of the thyroid, cricoid, and arytenoid cartilages, an understanding of the relationships between the cartilages was of primary importance for creating a model for the purpose of biomechanical analysis. To do so, the 3D reconstructed models from CT images were analyzed and simplified, while preserving the biomechanically important dimensions. General laryngeal cartilage models were created and based primarily on the morphometric dimensions recorded in tables 2–1, 2–2 and 2–3. For the creation of an accurate model, more dimensions were required which were performed on the geometries reconstructed from CT images.

The models were constructed using splines, points, and simple geometrical shapes. Splines were used to outline sketches by joining the respective points. They also served as guide curves to delimit the curvature of the cartilage. The points marked important locations measured from the reconstructed geometries. Details about the creation of the general models, and engineering drawings showing the important cross-sections and dimensions for the cartilages are presented in appendix A.

2.3.2 Vocal tract and vocal fold models

CT scan data for different postures of the larynx and vocal folds were used, two of which are shown in figure 2–3.

The cross section of the 3D vocal tract model of the first set of images, before and after smoothing is illustrated in figures 2–3(a) and 2–3(b). A large gap between the vocal folds can be observed in these images showing that this set was obtained during respiration. No abnormalities were visible in the images and according to our otolaryngologist collaborator, the subject can be considered geometrically healthy. Sharp edges were removed after smoothing, making the geometry ready for further numerical simulations. Vocal folds, false folds, ventricles, subglottal and supraglottal regions are shown in figure 2–3(b). The second set of CT data was related to the post-surgery images of a patient with cancer and was obtained during phonation with the vocal folds partially closed. The smoothed cross section from the 3D solid model of the post-surgery larynx is shown in figure 2–3(c). Asymmetry between left and right vocal folds can be observed because cancerous tissue was removed from the left vocal fold.

In a human larynx, the vocal tract and glottis are defined as the hollow space within the larynx and between the vocal folds respectively. In numerical simulations, these cavities substitute the computational domain. The 3D vocal tract model and the corresponding 2D mid-sagittal images for both healthy and post-surgery larynges are shown in figures 2–4 and 2–5 respectively.

Three dimensional models of the vocal tract were built with various sizes depending on the type of simulation that the geometry will be used for. For instance, geometries that only consist of vocal folds, can be used for structural and vibration analysis. However, more accurate results may be obtained for acoustic and CFD simulations if geometries that include the upper and lower airways are used. In figure 2–6, a large part of the trachea, vocal folds, pharynx, oral cavity and the beginning of the nasal cavity are visible, permitting a more realistic 3D model to be used for fluid flow simulation in the vocal tract and upper airway.

Morphometric measurements of the laryngeal cartilages and creation of the general models were performed by undergraduate student Christina Moro under co-supervision of the author of the present dissertation as a Summer Undergraduate Research in Engineering (SURE) at McGill University. Visual analysis of the CT scan data for the present study was preformed by Karen Kost¹.

¹ Otolaryngologist MD from the Department of otolaryngology, head and neck surgery, McGill University

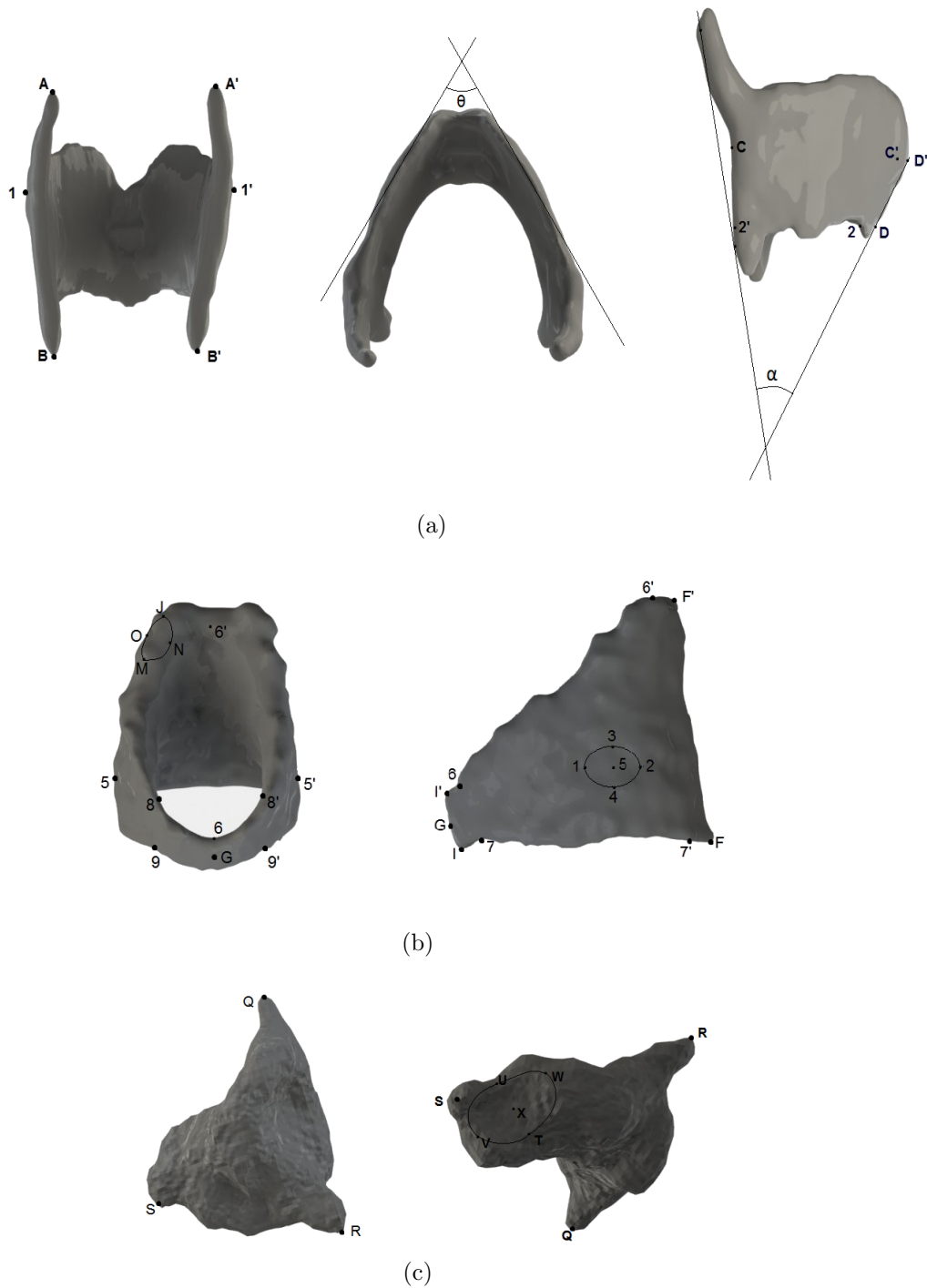


Figure 2-2: Measurements definitions and landmarks: (a) thyroid (b) cricoid (c) arytenoid

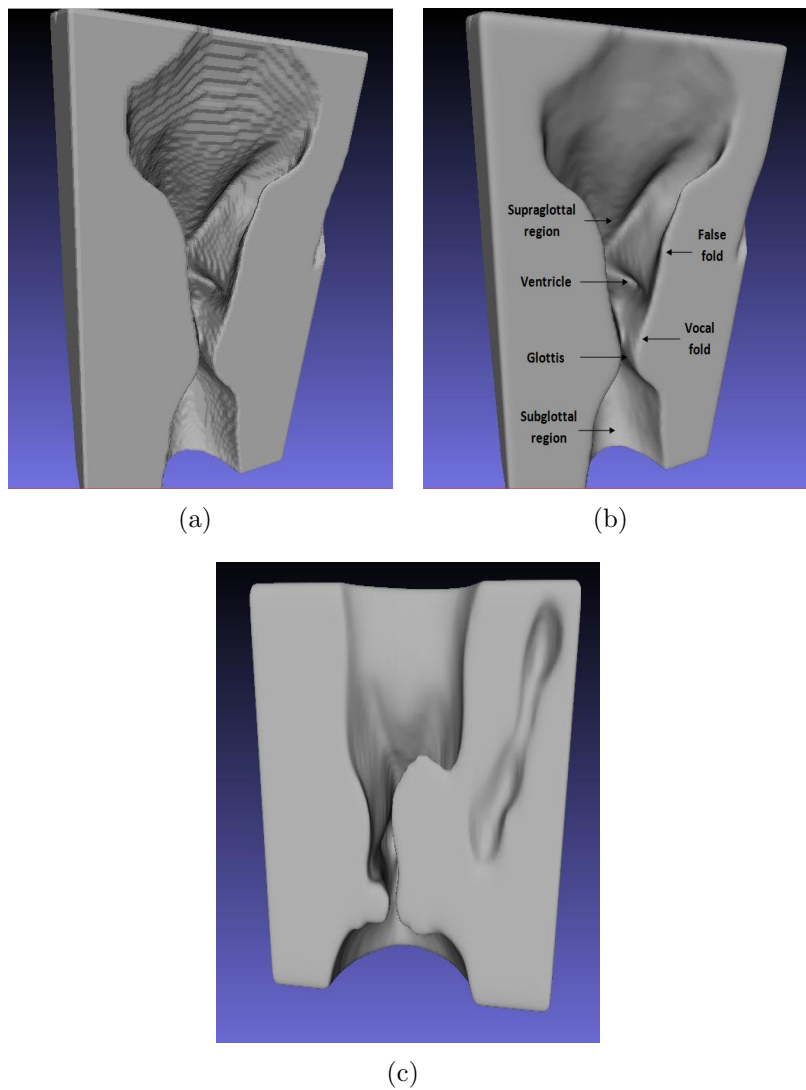


Figure 2–3: Cross section view of 3D reconstructed vocal tract: (a) healthy larynx before smoothing (b) healthy larynx after smoothing (c) postsurgical larynx

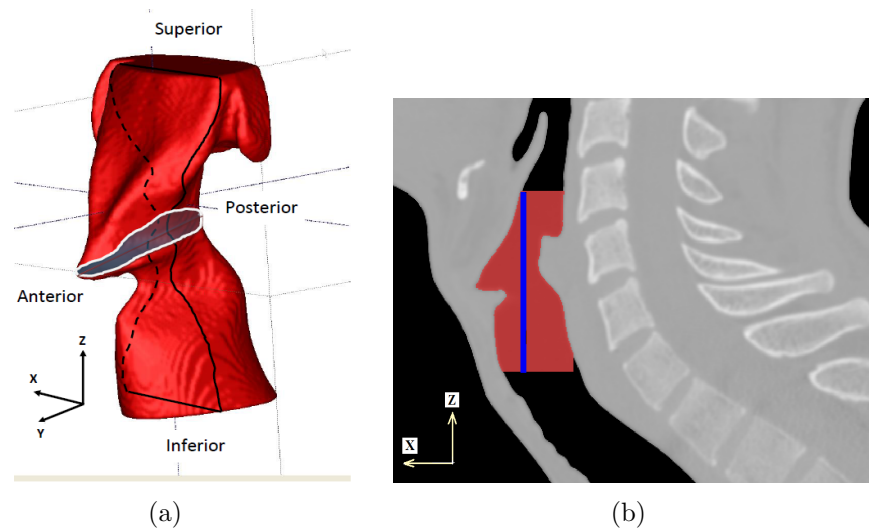


Figure 2-4: Healthy larynx: (a) vocal tract model and (b) corresponding sagittal view

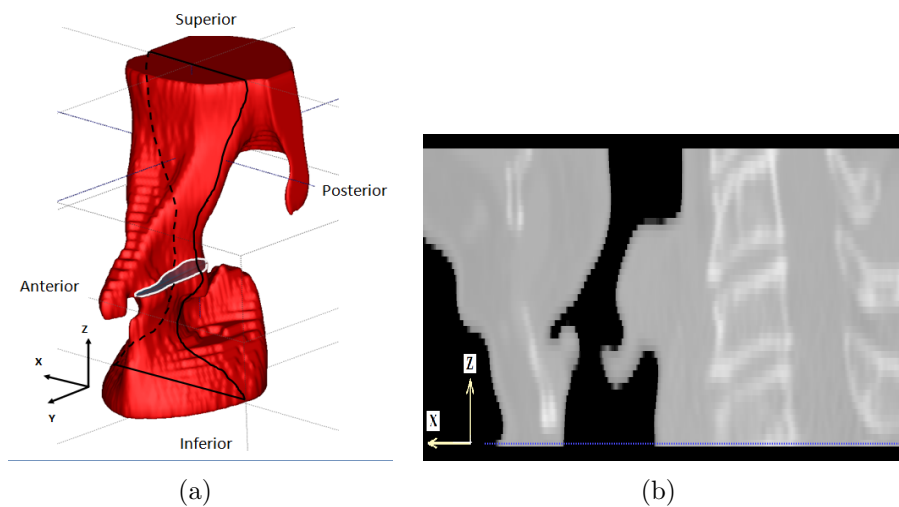
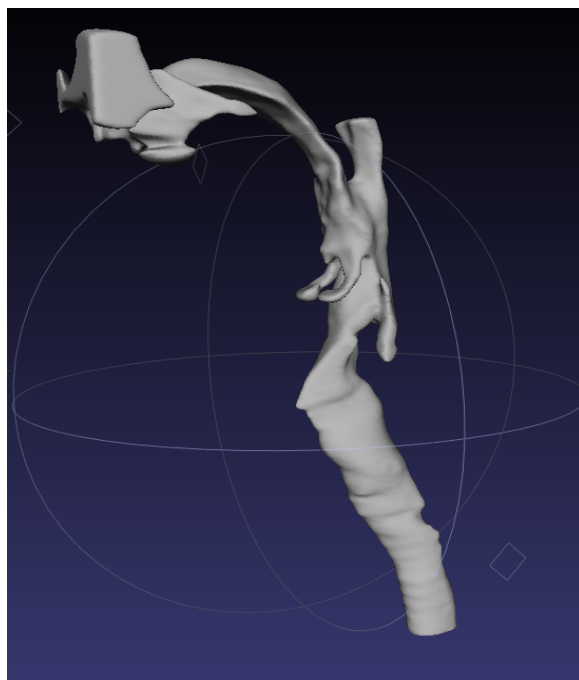


Figure 2-5: Post-surgery larynx: (a) Vocal tract model and (b) Corresponding sagittal view



(a)



(b)

Figure 2–6: Complete vocal tract: (a) 3D solid model (b) Corresponding sagittal view

2.4 Discussion

2.4.1 Comparison of morphometric measurements between 3D solid models and cadaver data

For the purpose of reconstructing the laryngeal framework and vocal folds, CT was used in this study because it is well suited for visualization of ossified structures. CT scanning also permits in-vivo visualization of the human larynx, and has the advantage of being more accessible and more accurate than excised larynges because the geometry of the excised larynx is not completely realistic. Therefore, models created from patient scans are preferred as they conserve the realism of the muscles and the larynx. The same morphometric features defined by previous studies Eckel et al. (1994); Tayama et al. (2001) were easily measured on the reconstructed geometries, and accurate within a relatively small range of error.

During the segmentation process, the thyroid was found to be the easiest cartilage to section due to its large size and high ossification levels. Generally, manual editing was limited to the interior of the lamina thickness, which is the last part of the cartilage to calcify (Dang-Tran et al., 2010). It is noteworthy to mention that manual editing of this part did not alter the measurements, but could potentially determine whether the imported body in Solidworks[®] was a solid body or a surface body. The dimensions of the segmented 3D models were comparable to those of Tayama et al. (2001), both in terms of average percent difference (7.14%) and standard deviations. These data are shown in table 2–1. The largest percent difference (16.41%) occurred for the angle between the thyroid laminae (α). This was expected because the standard deviation calculated by Tayama et al. (2001) was also very large (10.15).

Some aspects of the cricoid cartilage were difficult to segment. For instance, the inferior section of the cricoid cartilage displayed significant inhomogeneity in its laminae. Automatic segmentation was thus performed twice using different gray level intensity intervals in order to minimize the required amount of editing. A significant difference of 21.05% was recorded for the average height of the cricoid measurement ($F-F'$) in table 2–2. The standard deviations were twice those for the data by Tayama et al. (2001), 3.40% and 1.68% respectively. This may be because the rear boundaries are blurry near the inferior part of the cricoid, making the gray level intensity interval very similar to that of the surrounding soft tissue. It was therefore necessary to superimpose previously well segmented images onto the current image and define the remainder of the structure manually, which increased the error. Nevertheless, the average relative difference between the computed values and those of Tayama et al. (2001) was only 6.24%, suggesting accurate segmentation of the cartilage.

The pair of arytenoid cartilages were the hardest to segment and required the greatest amount of manual editing out of the three cartilages. The arytenoid cartilages gray level intensity interval overlapped with that of the cricoid, which may have caused the software to indiscriminately assign the same label to both structures. The arytenoids are mainly composed of two cartilages. The body is composed of hyaline cartilage, which ossifies over time, and the apices are composed of elastic cartilage, which never ossifies (Mupparapu & Vuppala, 2005). The vocal and muscular processes are thus more difficult to detect using CT imaging. The low visibility of the arytenoid apices may account for the relatively large differences in table 2–3 for the

distance measured between the vocal and muscular processes (16.96% - measurement R-S), and the distance between the vocal process and center of the cricoarytenoid facet (29.47% - measurement R-X).

2.4.2 General laryngeal cartilage models

The geometry of laryngeal cartilages is quite complex, and shows large differences in size and shape between subjects. For these reasons, it is very difficult to develop standard-sized medical tools (Joshi et al., 2001). There is a growing interest for subject-specific laryngeal models as tools for personalized medical care (Hunter et al., 2005). Nonetheless, the definition of generic models may be more useful for research applications, especially when investigating general phonation phenomena. General laryngeal cartilage models are desirable to ensure repeatability and comparability between research groups; and to provide a simple and accessible geometry to be used for simulation analysis. These models also allow the easy manipulation and editing of the structure, in order to conform to the desired research goals. Since all the biomechanically important dimensions are conserved, general laryngeal cartilage models can be used for various sorts of simulations, e.g. finite element modeling of the laryngeal framework or kinematic analysis of the laryngeal cartilages in different postures and its effects on the vocal folds, simulation of swallowing mechanism and simulation of larynx movement when pronouncing different sounds. Contrary to subject-specific models, general models are more easily accessible, because they do not require CT scans or MRI data of the subjects.

2.4.3 Vocal tract and vocal fold models

Vocal folds and vocal tract geometries are less complex than those of laryngeal cartilages. As pointed out earlier, because of the large difference between tissue and air intensity, segmentation of the vocal fold and vocal tract is easier and faster than that of laryngeal cartilages. As a result, it is more feasible to create human-specific solid models of the vocal tract and vocal folds rather than creating general models. In the present study, suggesting a general model for vocal folds was not considered because vocal folds are soft and their elongation varies in different phonation postures. Therefore the creation of a general 3D model of vocal fold depends on the mechanical property of the vocal folds' tissue, frequency of the phonation and the posture of the laryngeal framework which are beyond the scope of this study.

2.4.4 Limitation of the present study

Performing CT scan on healthy subjects may be hazardous due to the radiation, therefore all the reconstructions were performed on the existing patient data in the hospital archive. That hampered the creation of a normative model of a healthy larynx and vocal fold. Unfortunately, no comprehensive pathology information was available for subjects and that makes the comparison between cases more challenging and limited to the visible features from CT images. The settings of the CT imaging also differs from one subject to another and that could have affected the comparisons between different cases.

CHAPTER 3

3D reconstruction of human vocal folds by mapping HSDI data and MRI images

3.1 Introduction

The method of reconstructing 3D vocal fold models from CT scan data was explained in Chapter 2. However, MRI or CT images, show the geometry of the vocal folds at one specific moment. Therefore, the reconstructed geometries from these images represent one specific shape of the vocal folds. The 3D nature of the glottal airflow and the importance of 3D simulation are discussed in Chapter 5. However, performing FSI simulations has many difficulties, which make quasi-steady approximation in 3D-accurate geometries for glottal airflow simulation as an interesting alternative. In order to use quasi-steady approximation, the geometries of the vocal folds at different glottal angles during one complete cycle are needed. In the present chapter, the details about the image processing method for creating such geometries are explained. HSDI data was overlapped with MRI data. Due to the high temporal resolution of the HSDI data, after overlapping, the locations of the vocal folds edges at different time steps were obtained in MRI transverse images. Modified sets of MRI data were produced for the desired shape of the vocal folds in one complete oscillation cycle.

3.2 Experiments

The review board of the Research Ethics and Compliance of McGill University, Montreal Neurological Institute (MNI) and Hospital Research Ethics Board (REB) approved the protocol and consent procedure for the HSDI and MRI experiments, respectively. Four non-smoking adults, three men and one woman, aged between 22 and 29 years, participated in this study. The subjects were healthy with no current or past medical history or voice disorders. No subject was a trained voice user or had any background in clinical voice practice. Each subject participated in the HSDI and MRI experiments during different sessions. Each experiment is described separately in the following subsections.

3.2.1 High speed digital imaging (HSDI)

One color high-speed camera (Fastcam MC2- Model 10K; Photron Limited, San Diego, CA) attached to a rigid endoscope and a *Luxtec®* light source (*Integra®*, Burlington MA, Inc) were used for image recording. The sampling rate was selected to be $SR = 4000$ frame/s for all the measurements. A higher frame rate simply decreased image quality and camera field of view. The measurements were performed by an otolaryngologist at the voice clinic of the Montreal General Hospital. The subjects were asked to sustain vowel /i/ with a steady volume intensity of 80 dB during the recording. To prevent discomfort or burning from the powerful light, imaging was performed for no more than five seconds at a time. Ignoring transients associated with phonation onset and shutoff, the middle three seconds of the recording were selected for image processing. A microphone was held 30 cm away from the subject to monitor radiated sound pressure level. Each subject phonated at different pitches

with fundamental frequencies of $f_0 = 110, 130, 165, 220, 260$ and $f_0 = 220, 330, 440$ Hz for male and female subjects, respectively. Prior to the start of the imaging, subjects were asked to match their voice to a musical note produced at the desired pitch frequency.

3.2.2 Magnetic resonance imaging (MRI)

MRI experiments were performed to determine the exact pixel size in the high-speed digital images. The subjects repeated the same tasks as for the HSDI experiments. In addition, the subjects were asked to breath normally during imaging for two and half minutes. The vocal folds are far apart and have the open shape during breathing. To capture the closed shape of the vocal folds, the subjects were asked to start vowel /i/ and stop phonation after one second, hold their breath and keep their vocal folds closed during 12 seconds of imaging.

Three-dimensional MRI was performed using a Siemens 3T (Siemens Medical Solutions, Erlangen, Germany) scanner at the Montreal Neurological Institute. The Siemens “Neck Matrix Coil” and laser alignment was used to fix the position of the larynx. The subjects were scanned in a supine position while phonating normally at their comfort. Subjects were asked to sustain phonation during a scanning period of 12 seconds. The scanning protocol acquired T1-weighted (T1W) images and was performed with a FLASH (Fast Low Angle Shot) gradient echo sequence, with the following parameters: voxel size: $1.0 \times 1.0 \times 2.0 \text{ mm}$ with repetition time (TR): 12.0 ms and echo time (TE): 4.01 ms, flip angle: 20 degrees, and an image matrix of 256 pixels, giving a field of view (FOV) of 256mm. Again, the subject heard a musical note at the desired frequency through an intercom before each scan.

3.3 Image processing algorithm

The summary of the image processing method is shown in figure 3–1. The first step was to calculate the pixel size in high-speed images by comparing one known length in a HSDI image with the corresponding MRI image. In the second and third step, vocal folds edges were detected from HSDI images and their motion functions were obtained as functions of time. The mucosal wave was detected on the vocal folds in the fourth step and the mucosal wave propagation speed was calculated in the fifth step. In the sixth step, HSDI images were overlapped on the corresponding transverse MRI images and the motion functions of the vocal folds' lower layers were estimated using mucosal wave propagation speed and wave propagation methods. Finally, knowing the motion functions of the vocal folds surface, the desired location of the vocal fold surface and new series of MRI images were created. These new MRI images were used to construct 3D geometries of the vocal folds at the desired shapes.

Each step is elaborated in the following subsections.

3.3.1 Obtaining pixel size in HSDI images

The pixel size in MRI images were known from the scanning protocol therefore, by comparing a known anatomical feature in the MRI images with the corresponding ones in HSDI data, the pixel size of HSDI images were obtained for each set of data. For instance, the anterior-posterior length of the vocal fold, $L_M(m)$, in one transverse MRI image and the same length in the high-speed digital image, $L_H(Pixel)$, are shown in figure 3–2(a) and figure 3–2(b), respectively. As a result, the pixel size in HSDI data is $L_M/L_H(mm)$.

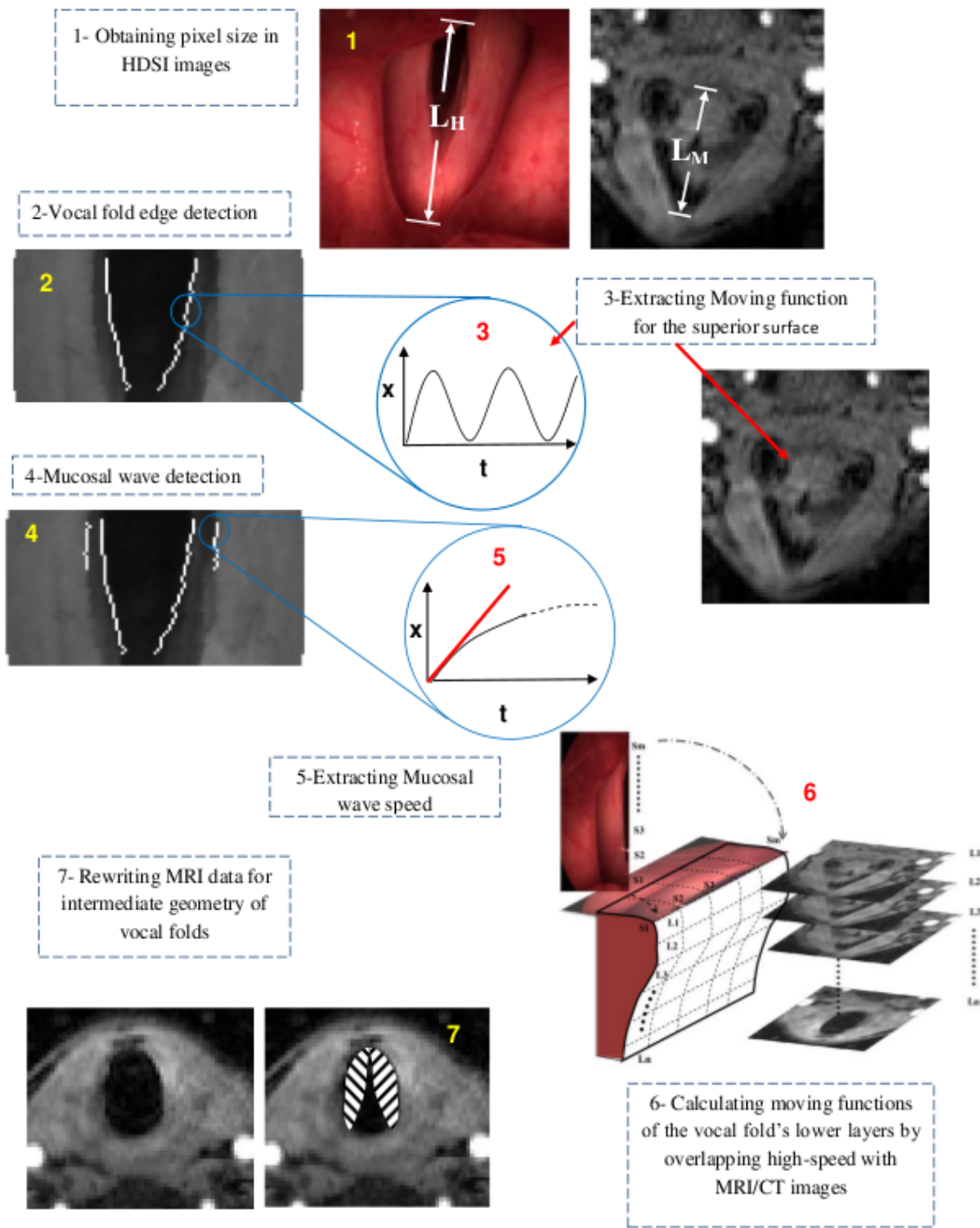
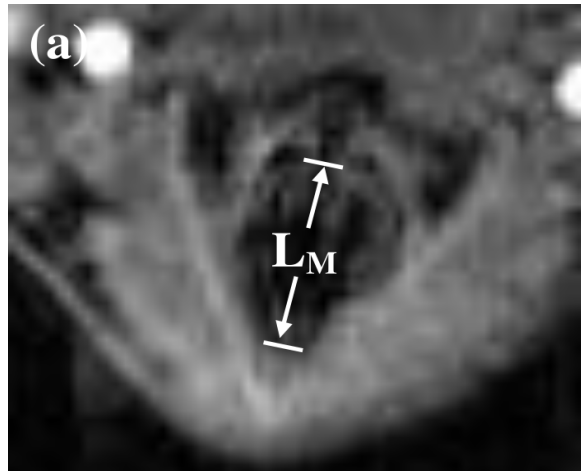
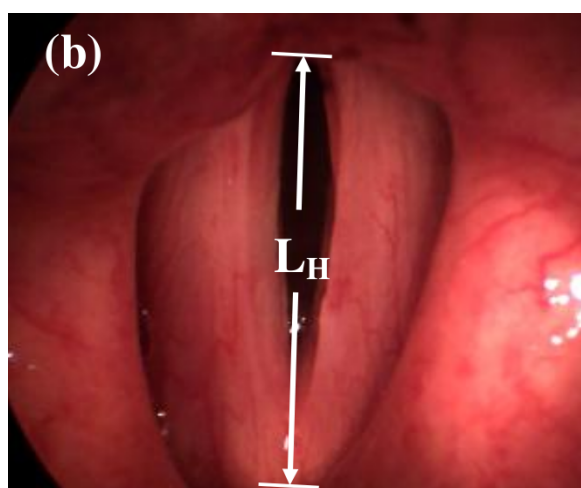


Figure 3–1: Summary of the image processing method (1) pixel size calculation in HSDI images (2,3) vocal fold edge detection and extraction of the oscillation function of the edge points (4,5) mucosal wave detection and calculation of the mucosal wave propagation speed (6) overlapping HSDI images with the MRI data and estimating the oscillation functions of vocal folds' lower points (7) imposing the desired location of the vocal fold boundaries on the MRI images and creation of a new set of MRI data



(a)



(b)

Figure 3–2: Comparison between the anterior-posterior lengths of the vocal fold while performing similar tasks: (a) $L_M(m)$, the anterior-posterior length in an MRI image and (b) $L_H(Pixel)$, the anterior-posterior length in a high-speed image.

3.3.2 Vocal folds edge detection and motion functions

Several methods have been suggested for vocal fold edge detection in the literature (Yan et al., 2006; Lohscheller et al., 2007; Zhang et al., 2010). A threshold-based edge detection algorithm was used in the present study. High-speed images were imported in *Matlab*® for image processing. The glottal midline was defined interactively by selecting and connecting the anterior and posterior commissures points in the first frame with the maximum glottal gap among the selected images in the stack of data as shown in figure 3–3 (a). The same line was considered the glottal midline for subsequent images in each set of data, because of the high imaging rate and the negligible movement of the larynx within the short imaging time interval. The midline center region of the vocal folds along the anterior-posterior direction was determined as the region of interest and the images were rotated ($\frac{\pi}{2} - \alpha$) degrees to make the glottal midline vertical, as shown in figure 3–3(b). To demarcate the vocal fold edges, the cropped high-speed digital images were converted to binary ones and the perimeter of the binary images was identified as shown in figure 3–3(c) and figure 3–3(d), respectively. The conversion threshold was obtained from the first local minimum of the image histogram (Wittenberg et al., 1995; Zhang et al., 2010). The locations where the intensity became unity in the binary images represented the vocal fold edge location, $VF(x, y)$. The obtained vocal fold edge overlapped on the gray scale image is shown in figure 3–3(e).

3.3.3 Mucosal wave detection

To estimate the motion functions of the lower layers of the vocal folds, the mucosal wave propagation speed should be calculated, as explained in section 3.3.4.

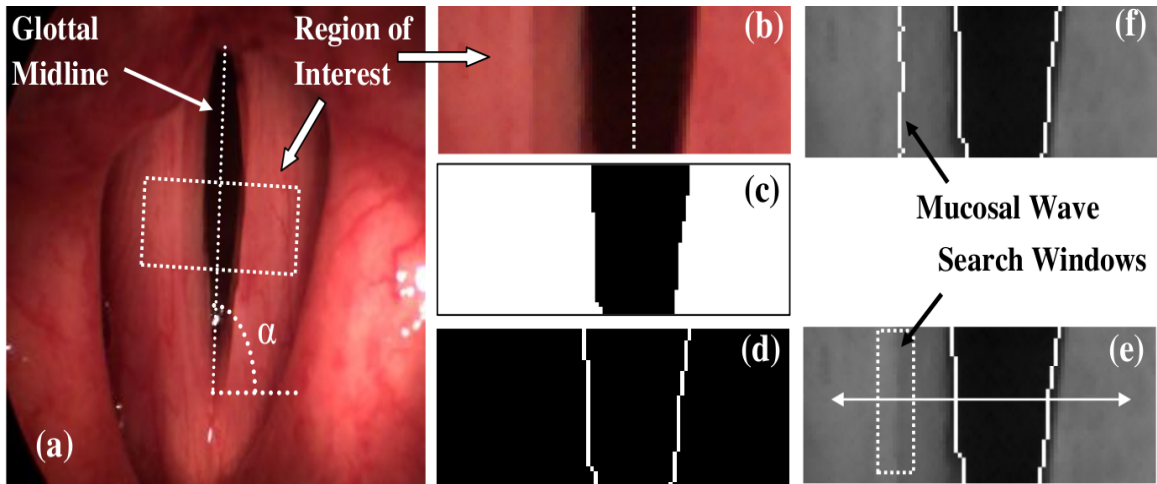


Figure 3-3: Image processing algorithm, Subject 1 phonating at 130 Hz: (a) pre-processed high-speed image, region of interest and non-vertical glottal midline; (b) magnified region of interest with vertical glottal midline; (c) binary image; (d) perimeter of the binary image, where boundaries represent the vocal fold edge; (e) the search window for mucosal wave detection, with obtained vocal fold edge overlapped on the gray scale image; (f) obtained mucosal wave overlapped on the gray scale image

Image intensity, $I(x, y)$, changed significantly in the vicinity of the vocal fold edge and the mucosal wave peak. To illustrate this, the gradient of the intensity along the arrow line in figure 3-3(e) is shown in figure 3-4(a). The two main extrema represent the location of the right and left vocal fold edges. A local extremum is also seen in figure 3-4(a) on the left fold that shows the location of the mucosal wave peak amplitude. In the case shown in figure 3-3 and 3-4(a), the wave on the left fold could not be detected possibly because the location of the camera was not exactly on the vocal folds' midline and perpendicular to the superior surface. However, in most cases the mucosal wave was detected on both of the folds, as shown in figure 3-4(b).

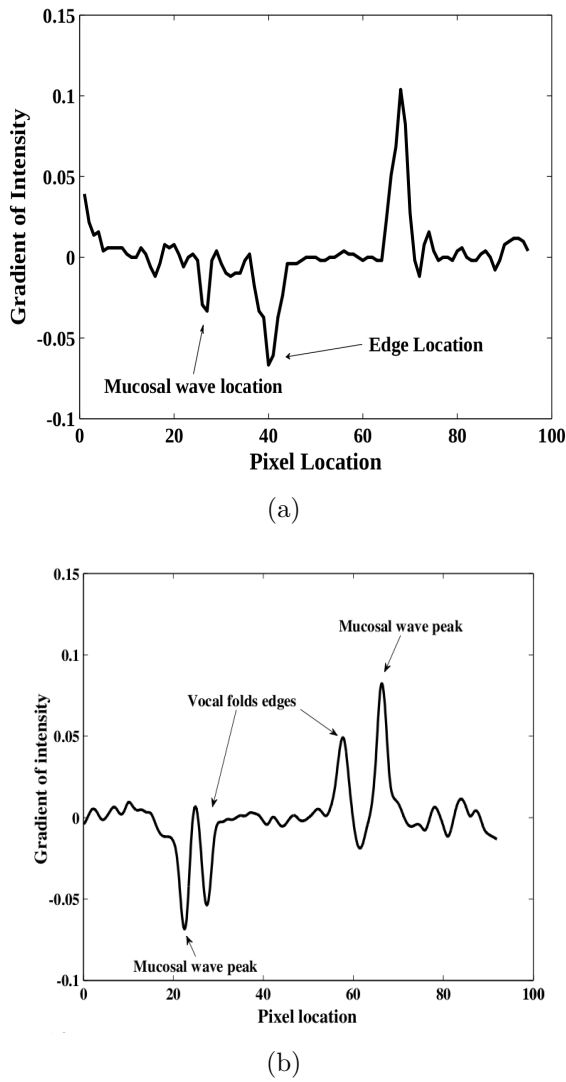


Figure 3–4: The intensity gradient on a medial-lateral line passing through the vocal folds' midpoint. (a) Phonation frequency 130 Hz , mucosal wave peak was seen only on the right fold, (b) Phonation frequency 110 Hz , mucosal wave peak was seen on both folds

To detect the mucosal wave, a search window was defined near the vocal fold edge, as shown in figure 3–3(e). The search window moved in the lateral direction with a velocity equal to the average edge velocity of the midpoint in the medial lateral direction, $\bar{V}_{edge} = \Delta VF/N$, where ΔVF is the edge displacement of the midpoint between the fully closed and fully open phases, and N is the number of frames in which this displacement occurs. The width of the search windows was selected to be equal to ΔVF pixels. The gradient of intensity in the search window was calculated and the location of the mucosal wave peak, $MW(x, y)$, was obtained. The mucosal wave peak is shown overlapped with the gray scale image in figure 3–3(f). The mucosal wave propagation speed, c_m , for each row in the image was calculated from:

$$c_m = \Delta MV \cdot SR \cdot L_M/L_H \quad (3.1)$$

where ΔMV (pixel/frame) is the change in the location of the mucosal wave in the lateral direction, SR is the sampling rate and L_M/L_H is the pixel size calculated in section 3.3.1. For the cases in which the mucosal wave is visible on both vocal folds, the average of the values obtained from the left and right vocal folds was considered as the mucosal wave speed. For each set of images, the mucosal wave speed was obtained from four different oscillation cycles with at least 1000-frame distance. The variations were found to be negligible, with a standard deviation of less than 6 percent, and thus the mean values were used in the following sections.

3.3.4 Moving functions of the vocal folds' lower layers

The superior surfaces of the vocal folds are visible in the HSDI data. The location of the visible surface is shown on one sagittal MRI image in figure 3–5.

Lower layers of the vocal folds are only visible in transverse MRI images as shown in figure 3–5. To obtain the motion functions of the vocal folds edges for the lower layers, the HSDI and transverse images were overlapped. Figure 3–6 schematically

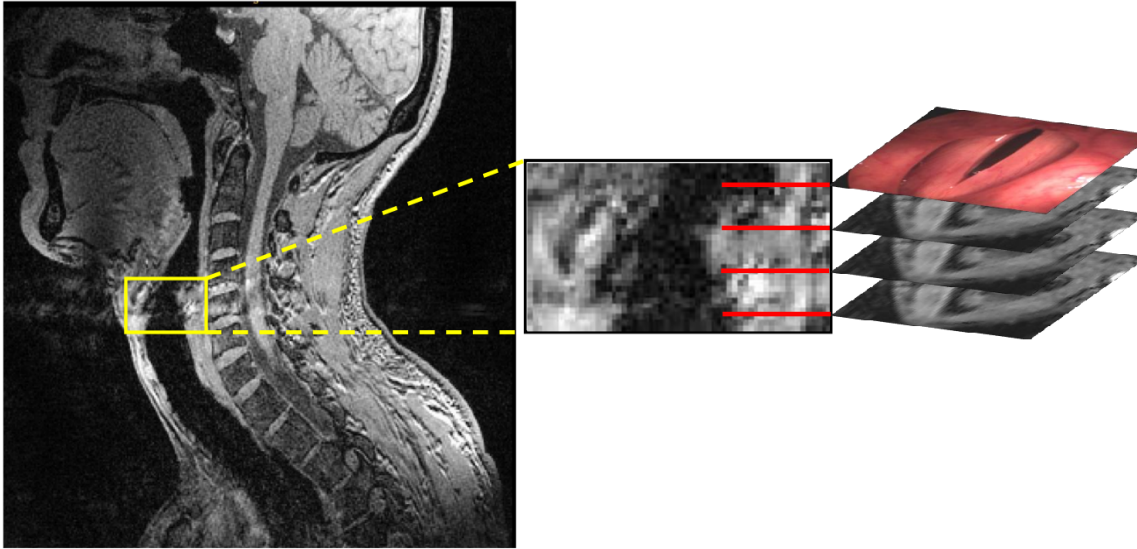


Figure 3–5: HSDI data shows the superior surface of the vocal folds. The lower layers of the vocal folds are visible in transverse MRI images. HSDI data was overlapped on the corresponding MRI transverse image at the location shown on the magnified box.

shows the overlapping of HSDI and MRI images. S_i ($i = 1 \dots m$) show the points at the vocal fold edge that are visible in the HSDI data. The number of points, m , depends on the number of pixels in the HSDI images showing the vocal folds edge in the anterior-posterior direction. L_i ($i = 1 \dots n$) show the number of MRI transverse images that show the vocal folds.

By obtaining the location of the vocal fold edges, as described in section 3.3.2, the edge movement as a function of time was curve-fitted with a sinusoidal function

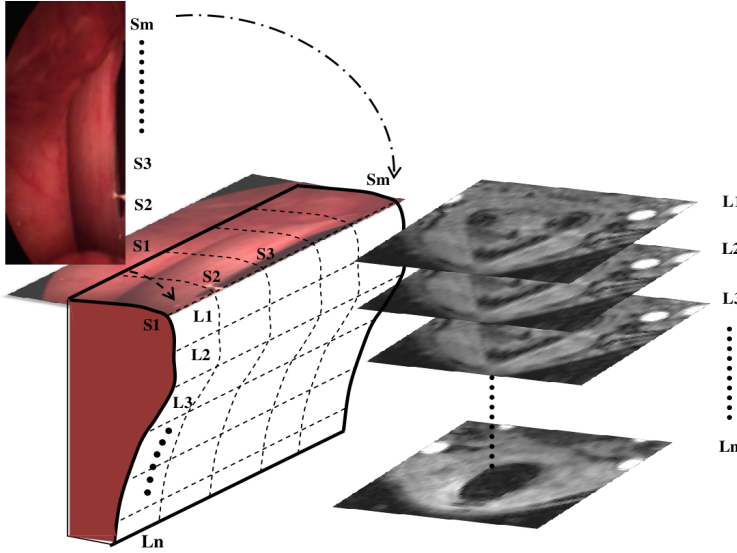


Figure 3–6: Overlapping HSDI and MRI images of vocal folds. The motion functions of the superior points S_i were obtained from the edge detection method on HSDI images. The motion functions of the lower layers, L_i were obtained using the mucosal wave speed. Each of the lower layers corresponds to one MRI image in the inferior-superior direction

for superior points, S_i ($i = 1 \dots m$) in figure 3–6. The motion functions of the vocal fold points are assumed to have the form

$$MF(s, t) = A_i \cos(\omega(s/c_m - t)) \quad (3.2)$$

with vibration amplitude of A_i and propagation speed of c_m . In Eq 3.2, s is the arc length in the direction of the wave propagation. The mucosal waves propagate from the lower layers of the vocal folds toward the superior layers and, upon reaching the surface, travel in the lateral direction. It was assumed that $s = 0$ represents the vocal fold edge on the superior surface. The frequency of oscillation was known and the mucosal wave propagation speed was calculated in Eq 3.1. To estimate the oscillation

amplitude in the medial-lateral direction, the frontal MRI images of the vocal folds in two different shapes of fully closed and fully open were used. Figure 3–7 shows the schematic frontal slice of the vocal folds in two different shapes. The solid line shows the closed shape at $t = t_1$ and the dashed line shows the open shape of vocal folds at $t = t_2$. For the superior points, the displacement of the vocal fold edge in the medial-lateral direction between $t = t_1$ and $t = t_2$ was considered to be two times the oscillation amplitude as shown in figure 3–7.

In order to obtain the motion functions of the vocal folds' lower layers, (i.e., $L_i (i = 1 \dots n)$), the oscillation phase differences and amplitude differences between lower layer points and the corresponding superior point were calculated. The actual distance between L_1 and S_1 , ΔS , was approximated by the distance in the inferior-superior direction, ΔZ , as shown in figure 3–7. Given the ΔZ and using Eq 3.2, the phase difference between S_i and L_i was calculated. To estimate the amplitude of the point L_1 , Eq 3.2 at $t = t_1$ and $t = t_2$ was used:

$$MF(L_1, t_1) = A_{L_1} \cos(\omega (\Delta z / c_m - t_1)) \quad (3.3)$$

$$MF(L_1, t_2) = A_{L_1} \cos(\omega (\Delta z / c_m - t_2)) \quad (3.4)$$

$$A_{L_1} = \frac{MF(L_1, t_2) - MF(L_1, t_1)}{[\cos(\omega (\Delta z / c_m - t_2)) - \cos(\omega (\Delta z / c_m - t_1))]} \quad (3.5)$$

$\Delta MF = (MF(L_1, t_2) - MF(L_1, t_1))$ is the displacement of the point L_1 between the fully closed and fully open shape, which can be measured from the frontal MRI

image, as shown in figure 3–7. The same procedure was repeated for all the points on the vocal fold surface and they motion functions were thus obtained.

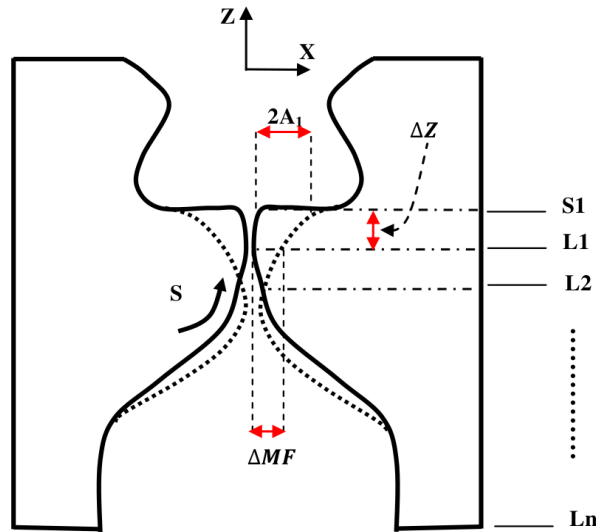


Figure 3–7: Schematic frontal view of the vocal folds. The amplitude of vibration was calculated for the edge points at different layers by comparing the fully closed and fully open shapes

3.3.5 Rewriting MRI data for intermediate geometry of vocal folds

Having the motion functions of the vocal folds at different layers, the MRI images of vocal folds at intermediate configurations between fully open and fully closed shapes were produced. The boundary location of the vocal folds at each layer was obtained from edge motion functions, calculated in section 3.3.4. The fully open MRI transverse images at each layer were selected and the new vocal fold boundary was superimposed on the original image, as shown in figure 3–8. Figure 3–8(a) shows the original MRI transverse image of fully open vocal folds. Figure 3–8(b) schematically shows the new boundary of the vocal folds for an intermediate

configuration superimposed on the original image. The image intensity for the hashed points was set equal to that of the adjacent points on the vocal folds. This procedure was repeated for all layers (i.e., L_1 to L_n). Revised images along with the other unchanged images were used to make the new set of data, which corresponds to the intermediate geometry of the vocal folds.

MRI and CT scan images have the DICOM extension and each set of DICOM images has a unique identifier(UID) that can be obtained using the `info.SeriesInstanceUID` command in *Matlab*. A new UID should be generated to write the modified images as a new series of DICOM images. The following command was used to create the unique identifier.

```
uid = dicomuid;
```

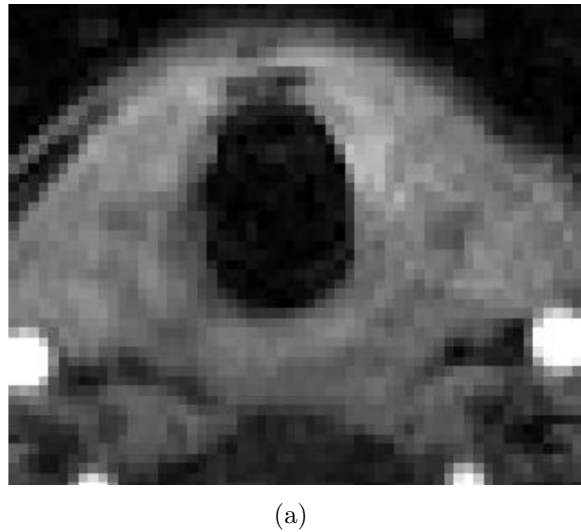
and the value of the `info.SeriesInstanceUID` was set to be:

```
info.SeriesInstanceUID= uid;
```

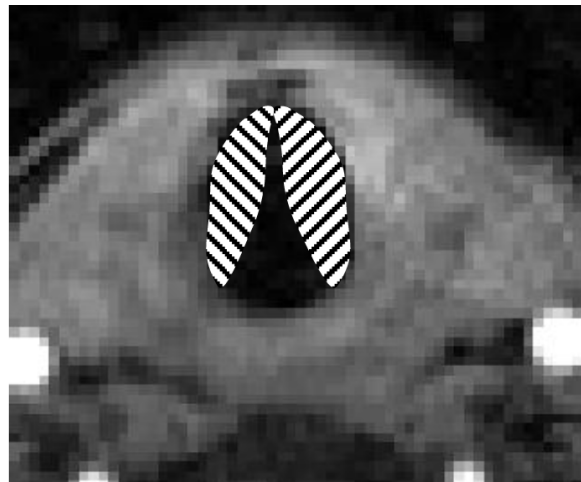
Using `dicomwrite` command, the modified images were written as a new set of `dicom` data:

```
dicomwrite(Modified_images,'New_set_of_images.dcm',info);
```

Further details can be found in the help of *Matlab* software under the section of “Reading and Writing Data in Medical File Formats.”



(a)



(b)

Figure 3–8: (a) MRI image in the transverse plane at the level of the vocal folds
(b) New boundaries of the vocal folds for an intermediate geometry were shown as hashed regions. The image intensity of the hashed regions was set to be equal to that of the adjacent points on the vocal folds

3.4 Results

The 3D geometry of the vocal folds in the fully open shape is shown in figure 3–9(a). This geometry is reconstructed from the input `dicom` data with no additional editing on the images. Figure 3–9(b) shows an example of the intermediate geometry of the vocal folds at an arbitrary shape between fully closed and fully open. This geometry was made from the modified set of `dicom` data. Figure 3–9(b) shows that the vocal folds are partially closed, with the anterior points not yet closed. For the sake of better visibility, both images are shown from the inferior direction. Both 3D geometries were smoothed after reconstruction.

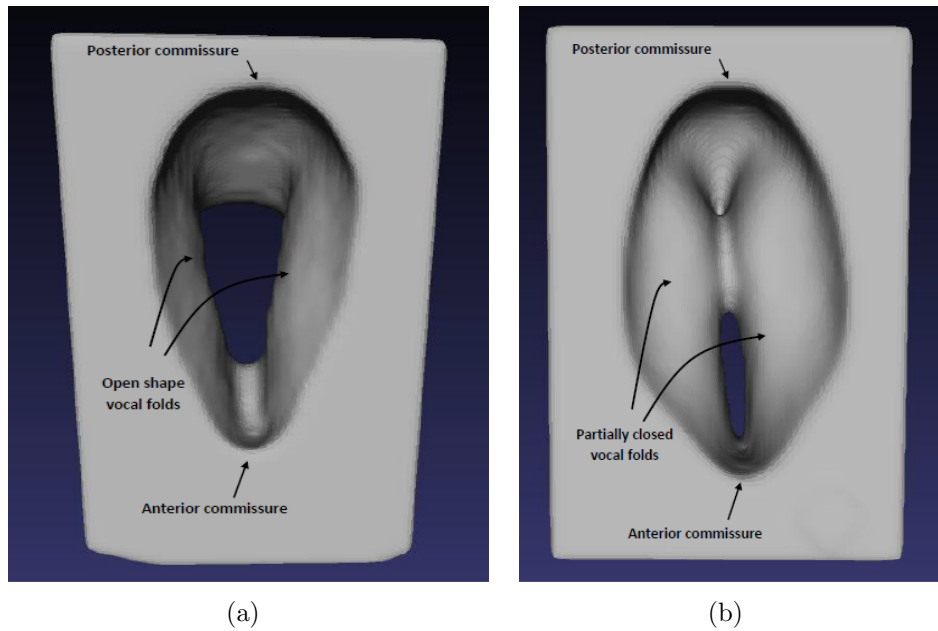


Figure 3–9: (a) 3D reconstructed geometry of vocal folds with the fully open shape (b) 3D reconstructed geometry of vocal folds from edited `dicom` data. Vocal folds have an intermediate configuration between fully closed and fully open.

3.5 Discussion

The image processing method suggested in this chapter has limitations that may have resulted in some errors. All points on the vocal folds were assumed to oscillate with a similar frequency. The movement of the vocal fold in the inferior-superior direction was neglected in this procedure. The number of MRI slices of the vocal folds in the inferior-superior direction is $n \leq 10$, which decreased the accuracy of the method; as a result the 3D reconstructed models have sharp edges on the vocal fold inferior surface. However, the output 3D geometries were smoothed based on the explained method in section 2.2.4 and most of the morphometric errors were eliminated.

Image quality of MRI is lower than that of CT for 3D reconstruction of the vocal folds; however, healthy volunteers cannot be sent for CT scanning because of radiation hazards. Healthy subjects participated in the present study to perform the phonation tasks and therefore, MRI was used instead of CT.

To obtain the best results several MRI protocols were examined. Trade-offs exist among scanning time and image resolution, number of slices and the gap between them in the desired scanning length. Longer time intervals would have increased image quality and the number of image slices in a fixed length. However, performing the tasks (e.g., breath holding or phonation) for long durations may have not been possible for all subjects; therefore, task duration was kept to 12 seconds.

Although the positions of the head and larynx were fixed before imaging, the imaging axes were not completely coincide with body planes. For instance, the obtained frontal images were not completely perpendicular to the anterior-posterior

axis, which can introduce error when approximating the motion functions of the vocal folds' lower layers.

CHAPTER 4

Assessment of the quasi-steady approximation in glottal airflow

4.1 Introduction

The quasi-steady approximation in voice production simulation consists of modeling the complex, unsteady flow through the glottis as a sequence of steady flows through rigid orifices. This approach is numerically less expensive than detailed unsteady simulations. Theoretical and experimental assessments of the accuracy of this approximation have been attempted, but contradictions in previously reported results prompt further analysis. Two-dimensional dynamic simulations of airflow through an idealized glottal orifice with moving walls were performed. A series of steady flow simulations was then performed using vocal fold configurations and boundary conditions that instantaneously coincide with data from the dynamic simulations. Geometries were created based on the M5 model (Scherer et al., 2001). The surface area of the model was kept constant to avoid volume variations, thereby eliminating spurious monopole sources. The results include the fluid flow rate, pressure on the vocal folds, shear stress on the glottal walls, and orifice discharge coefficient. Convective and local accelerations along the centerline within the glottis were evaluated for dynamic simulations. Comparisons between these variables were performed for both dynamic and static sets of data. The importance of time-dependent terms over short intervals during glottal opening and closing was scrutinized and the differences between dynamic and static simulations were investigated.

4.2 Methods

4.2.1 Orifice profiles and wall motion

The M5 model Scherer et al. (2001) was used to define the planar 2D profile of the glottis. In the present study, the surface area of the vocal folds was kept constant for all orifice angles during the oscillation cycles. That is a valid assumption because the vocal fold tissue is generally considered incompressible due to its large water content. Any net volume fluctuation would cause monopolar sound that would not be present in actual voice. That is opposed to the previous studies in which the vocal fold model enters into and exits from the domain e.g (Krane et al., 2007, 2010). In the M5 model, the orifice included angle, Ψ , ranges from -40° for convergent shapes to 40° for divergent shapes. In order to preserve the surface area, the orifice angle range (-40° to 40°) was divided into 40 different steps. In each step, the vocal fold area was calculated and compared to the convergent shape area, $A_0 = A(\Psi = -40^\circ)$.

The orifice angle is defined using Eq 4.1

$$\Psi = \begin{cases} 40(1 - \cos(2\pi t f)) & \dots 0 < t < 1/(2f) \\ -40(1 - \cos(2\pi t f)) & \dots 1/(2f) < t < 1/(f) \end{cases} \quad (4.1)$$

in which f is the frequency of the oscillation. The vocal fold profile for each angle value was shifted in the medial-lateral direction to obtain the same area as A_0 . This procedure determines the distance between the vocal fold tip and the centerline for each orifice angle and the exact location of all the points in the M5 model as a function of Ψ , i.e $x(\Psi)$ and $y(\Psi)$. Location functions, $x(\Psi)$ and $y(\Psi)$, were

imported into COMSOL to accurately create the wall motion. More details about calculation procedure and the location functions are presented in appendix B.

The glottal shape for each static simulation was obtained from the snapshot of the dynamic simulation at corresponding time values. The orifice angle range was divided into ten equally spaced intervals, and the orifice profile at each time step was used in the static simulations.

4.2.2 Numerical simulations

Dynamic and static numerical simulations were performed using the commercially available software COMSOL *multiphysics*[®]. Incompressible Navier-Stokes along with Moving Mesh (ALE) packages were used for the time-dependent simulations. Only the Navier-Stokes package was used for the steady-state simulation.

Figure 4–1 shows the computational domain for the divergent vocal fold included angle. Although the orifice profile is symmetric with respect to the centerline, the flow simulations were performed over the entire glottal orifice. The computational domain included both right and left vocal folds, with no symmetry boundary condition applied on the centerline, to allow the capture of possible asymmetric effects in the flow field, such as the Coanda effect (James, 1977). The two vocal folds were assumed to have identical shapes, although small differences between the right and left fold have been reported in the literature (Hirano et al., 1989; Lindestad et al., 2004; Šidlof et al., 2008) . To obtain the convergence in the simulation, the computational model was scaled up with a factor of 10 relative to the real-life M5 model dimensions. Dynamic and geometry similitude laws were used and Reynolds number, $Re = \rho \frac{\bar{U} \cdot D}{\mu}$, Strouhal number, $St = f \cdot D / \bar{U}$ and dimensionless pressure, $\Delta P / (\frac{1}{2} \rho \bar{U}^2)$, were kept

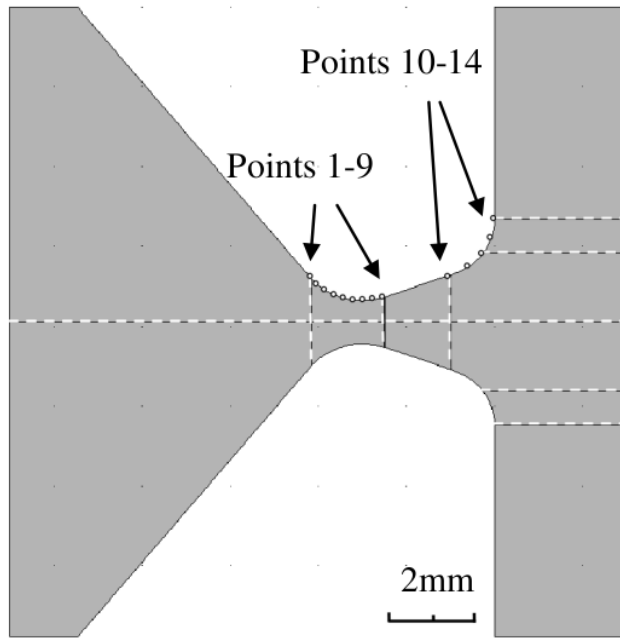


Figure 4–1: Computational domain geometry with divergent vocal fold shape

the same as the real-life dimension in which ρ is the air density, μ is the air viscosity, \bar{U} is the inlet average velocity, D is the channel width and P is the pressure. Dynamic and geometry similitude is commonly used for computational and experimental modeling of glottal flow e.g (Kucinschi et al., 2006). For equal Reynolds numbers, the velocities in the model must be 10 times smaller than in real-life and as a result, the flow rates are 10 times larger. To keep the pressure coefficients equal, the pressure in the model must be 10^2 times smaller than in real-life. Equality of the Strouhal number leads to the frequency of the model being 10^2 smaller than the real life.

The computational domain used in this study has a relatively short supraglottal length. Truncated geometries have been previously used in other glottal flow studies

such as (Scherer et al., 2001; Guo & Scherer, 1993; Kucinschi et al., 2006, 2008). According to these studies, using a shorter inlet and outlet length, does not affect the predicted pressure. Guo & Scherer (1993) studied a computational model with long supraglottal lengths (more than 16 times of the subglottal lateral diameter). They reported that for Reynolds numbers up to 300, the reattachment of the flow to the wall occurs at a distance equal to 15 times of the subglottal lateral diameter and for higher Reynolds numbers convergences of the computational model were not obtained. That may be due to the transition from a laminar to a turbulent flow when the jet flow is discharged out of the glottal exit (Guo & Scherer, 1993). A shorter supraglottal domain ensures that the fluid flow is laminar over the computational domain (Guo & Scherer, 1993). Furthermore, the length of vocal tract in reality is almost half of the required length for reattachment and pressure variations in the pharynx are negligible (Guo & Scherer, 1993). As a result, the computational domain with short inlet and outlet was used to reduce the computational cost.

In both the dynamic and the steady simulations, the orifice did not obstruct the airway completely to prevent numerical instability from collocation of grid points. The imposition of a small gap between the vocal folds during closure is common in glottal flow simulation e.g (Alipour et al., 1996a; Kucinschi et al., 2006; Sidlof, 2007; Sciamarella & Le Quéré, 2008). The smallest distance between the vocal fold for the present model was 0.02 of the channel width.

The computational domain was subdivided into different subdomains for both static and dynamic simulations using “help lines,” as illustrated by dash lines in figure 4–1. The mesh size can be defined separately in each of the subdomains. Help lines were

used because they enable a finer mesh in subdomains near the constriction walls and a coarser mesh in other subdomains. They also help prevent mesh inversion, a common problem for moving boundary problems with large deformations. In this study, help lines track boundary motion, which reduced mesh deformation and better convergence of the solution.

To set the subdomains parameters and boundary conditions in the incompressible Navier-Stokes solver, the air density and viscosity were defined for subdomains. The gauge pressure magnitude was imposed at inlet and outlet boundaries. In the time-dependent simulations, the inlet pressure was gradually ramped up at a constant rate from zero amplitude to the desired value ($P=1000$ Pa). A homogeneous outlet gauge pressure was imposed. The vocal fold boundaries were defined as moving walls in the software. A no-slip boundary condition was imposed on other sections of the wall, i.e trachea walls. A pressure gradient equal to that of the dynamic simulation was used for the steady-state simulation. A constant pressure magnitude was imposed at the inlet and no ramp function was used. The outlet pressure was zero and the no-slip boundary condition was applied on all other boundaries.

A moving mesh application mode was used to handle the moving wall problem in the dynamic simulation. The moving mesh application in COMSOL uses the Arbitrary Lagrangian Eulerian (ALE) method. Further details on the ALE method can be found in the COMSOL documentation and other sources e.g (Kjellgren & Hyvärinen, 1998; Sarrate et al., 2001). To define the subdomain settings and boundary conditions for the moving mesh solver, the “mesh free displacement” condition was applied to all subdomains. The zero mesh displacement applied to all boundaries

except the vocal fold ones. Location functions for points 14,10,9 and 1 in figure 4–1 were calculated in the appendix, which define the horizontal and vertical components of the mesh displacement at the start and the end points of each vocal fold boundary segment. To achieve a smooth surface over the entire oscillation cycle, the curves along the superior and inferior tips were divided into 4 and 8 segments, respectively as shown in figure 4–1. Linear interpolation was used for the points between 1 to 9 and 10 to 14.

The Mach number, based on the maximum velocity in the glottis, was $M \approx 0.1$ and $Re < 2500$ and the fluid flow was considered incompressible. No turbulence modeling was used and the Navier-Stokes and continuity equations, Eq 4.2, were solved:

$$\begin{cases} \rho \frac{\partial \mathbf{u}}{\partial t} + \rho (\mathbf{u} \cdot \nabla) \mathbf{u} = \nabla \cdot [-P\mathbf{I} + \mu (\nabla \mathbf{u} + (\nabla \mathbf{u})^T)] \\ \nabla \cdot \mathbf{u} = 0 \end{cases} \quad (4.2)$$

in which \mathbf{u} is the velocity vector. The UMFPACK solver was selected for both stationary and time dependent solutions. COMSOL uses an implicit scheme which is stable for any time step size. The computational method has a second order accuracy. For the time dependent solution, the BDF time stepping method was used and the error in each integration step was controlled by both absolute and relative tolerance. In COMSOL, the time step is acceptable if :

$$\left(\frac{1}{N_d} \sum_i \left(\frac{|E_i|}{AT_i + R|U_i|} \right)^2 \right)^{1/2} < 1 \quad (4.3)$$

in which U_i is the solution vector corresponding to a certain time step, and E_i is the error estimated by the solver for U in this time step, N_d is the number of degrees of freedom (DOF), AT_i is the absolute tolerance for DOF i and R is the relative tolerance. For the present cases, a relative tolerance of 0.01 and an absolute tolerance of 0.001 were used.

4.2.3 Mesh refinement

Free mesh parameters in COMSOL was used to create an unstructured triangular mesh. The computational domain was divided into more than 162,000 and 188,000 elements for the dynamic and static simulations, respectively. The mesh size in subdomains and on the boundaries was refined for three steps to achieve convergence. Mesh refinement scales in each step differ for one subdomain to another. Subdomains near the glottis had a finer mesh to resolve larger velocity gradients. In the fourth step, the maximum mesh size on the boundaries is one twentieth time that of the first simulation, and the maximum mesh sizes in the glottis subdomain and on the glottis boundaries are $D/32$ and $D/160$, respectively. The shear stress on the vocal fold wall at a parallel position from the dynamic simulation, S^{dy} , was monitored to establish the mesh dependency of the results. The L^2 relative error norm and number-of-elements ratio were calculated in each refinement step using Eq 4.4. The results are presented in Table 4–1.

$$L^2 \text{ relative error norm} = 100 \times \frac{\sqrt{\sum (S_{(n+1)th}^{dy} - S_{(n)th}^{dy})^2}}{\sqrt{\sum (S_{(n)th}^{dy})^2}} \quad (4.4)$$

$$\text{Number of elements ratio} = \frac{\text{Number of elements } (n+1)}{\text{Number of elements } (n)} \quad (4.5)$$

Table 4–1 shows that relative error is negligible and the results are mesh size independent in the last refining step.

Case	Number of elements	Number of elements ratio	L^2 relative error norm(%)
Base, n=0	14154		
n=1	38144	2.6949	38.06
n=2	80766	2.1174	4.42
n=3	162372	2.0104	3.07

Table 4–1: The number of elements in each refinement step and relative error between refinement steps

4.3 Results and discussion

A pressure gradient of ($\Delta P = 1000 Pa$) across the glottis and an oscillation frequency of $f = 100 Hz$ was imposed. The pressure gradient and stress on the walls were compared for three different vocal fold configurations: convergent, parallel and divergent, corresponding to $\Psi = -40^\circ$, 0° and 40° , respectively. Fourteen locations were selected for virtual probes at the vocal fold tip, as shown in figure 4–1. Shear stress and pressure were read at these locations to quantify the differences between the dynamic and static simulations. The normalized error was calculated. The convective and temporal accelerations were compared along the centerline in the glottal region during one complete cycle.

4.3.1 Velocity profile and unsteady flow features

The computational fluid streamlines are shown in figure 4–2, 4–3, 4–4. Dashed lines represent help lines in the computational domain. A qualitative comparison

between the streamlines reveals an asymmetry in the velocity field. The asymmetry is greater for the divergent included wall angle as shown in figure 4–2. Dynamic simulations showed that fluid flow in the divergent configuration is less stable than in the convergent and parallel ones. The jet plume fluctuations result in greater differences between the static and dynamic solutions for the divergent configuration.

To better analyze the quasi-steady approximation, the equation of motion on the centerline of the domain is considered and the time dependent acceleration is compared with the convective one. The axial momentum along the centerline is given by Eq. 4.6:

$$\frac{\partial u}{\partial t} + u \frac{\partial u}{\partial x} = -\frac{1}{\rho} \frac{\partial P}{\partial x} \quad (4.6)$$

in which u is the component of the velocity along the glottis from the subglottal to the supraglottal region. The centerline is considered to be far from the boundary layer and that is why the viscous terms are ignored in this equation. The first term on the left-hand side is the time dependent acceleration or local acceleration, and the second one is the convective acceleration term. These two terms were compared at two different locations (points A and B in figure 4–2(a) and 4–4(a)) along the centerline in the glottal region with the minimum glottal width for fully divergent and convergent configurations. The convective and local accelerations for these points are shown in figure 4–5.

Their magnitudes were normalized by the maximum convective acceleration magnitude of point A. The unsteady accelerations were found to vary less than the convective ones during the cycle. The convective acceleration at point A is very large

while the vocal folds are moving toward each other. This peak is due to the increase in the velocity gradient, $\frac{\partial u}{\partial x}$. When the vocal folds are in a converging configuration, spatial changes of velocity dominate temporal changes. For point B, the convective acceleration is larger than the local one over one complete oscillation cycle. When vocal folds have a convergent shape, the difference between local and convective accelerations is lower than for the rest of the cycle. For point A, there is no apparent difference between local and convective accelerations. The ratio of the local and the convective acceleration for point A is shown in figure 4–6. Over more than 70 % of the cycle this ratio is equal to or less than 0.1. The convective acceleration is larger than the local acceleration over most of the cycle, until the moment when the included angle becomes divergent. At the opening and closing moments, the local acceleration is not negligible. This observation is consistent with previous studies about the inaccuracy of quasi-steady approximation during the opening and closure phase of oscillation (Park & Mongeau, 2007).

4.3.2 Pressure gradient

The glottal wall pressures obtained from dynamic and static simulation at 14 virtual probe locations for three different angles are shown in figure 4–7. For the convergent included angle (-40°), the pressure is positive producing a net lateral force that pushes the vocal folds outward. Figure 4–7 shows that the results from dynamic and static simulations are in a perfect agreement. It also shows that among the three configurations, the best match was obtained for the parallel vocal fold configuration. This confirms previous observations e.g (Park & Mongeau, 2007), on

the validity of quasi-steady approximation during the open phase of the glottal duty cycle.

4.3.3 Wall shear stress

The shear stress was calculated at 14 locations on the vocal fold surface. The maximum shear stress was found at point 5 for the divergent included angle, at point 6 for the parallel included angle and at point 10 for the convergent included angle. The shear stress on the surface of vocal folds had the largest magnitude for a divergent included angle and the lowest magnitude for a convergent included angle. The L^2 relative error norm of the dynamic and static results presented in Table 4–2. The error is minimum for a parallel included angle and maximum for a divergent included angle.

The discrepancy between the shear stress of the dynamic and static solutions			
Angle (°)	-40	0	40
L^2 relative error norm (%)	1.7767	0.6412	1.90

Table 4–2: The discrepancy between the shear stress of the dynamic and static solutions

4.3.4 Flow rate

The flow rate at the discharge boundary for the dynamic and static models is shown in figure versus orifice angle 4–8. The static flow rates are in good agreement with the dynamic ones. Over the complete cycle, the static flow rate values are bounded by the dynamic flow rate values. The L^2 relative error norm between the flow rate of the dynamic and static solutions was 3.92%.

4.3.5 Orifice discharge coefficient

The orifice coefficient is defined as:

$$C_d = \frac{Q}{(A_m \cdot u_m)} \quad (4.7)$$

which is the ratio of the flow rate, Q , to the minimum area, A_m , multiplied by the centerline velocity, u_m , at the point of minimum area (maximum constriction). The radiated sound pressure can be obtained analytically as a function of the orifice discharge coefficient for a case of a long non-reflecting tube and no acoustic loading (Park & Mongeau, 2007). The orifice discharge coefficient includes the effects of viscous losses, contraction in the wetted flow area and pressure head loss along a streamline passing through the centerline. Orifice discharge coefficients for the static and dynamic cases are shown in figure 4–9. The L^2 relative error norm between the dynamic and static orifice coefficients is 2.07%.

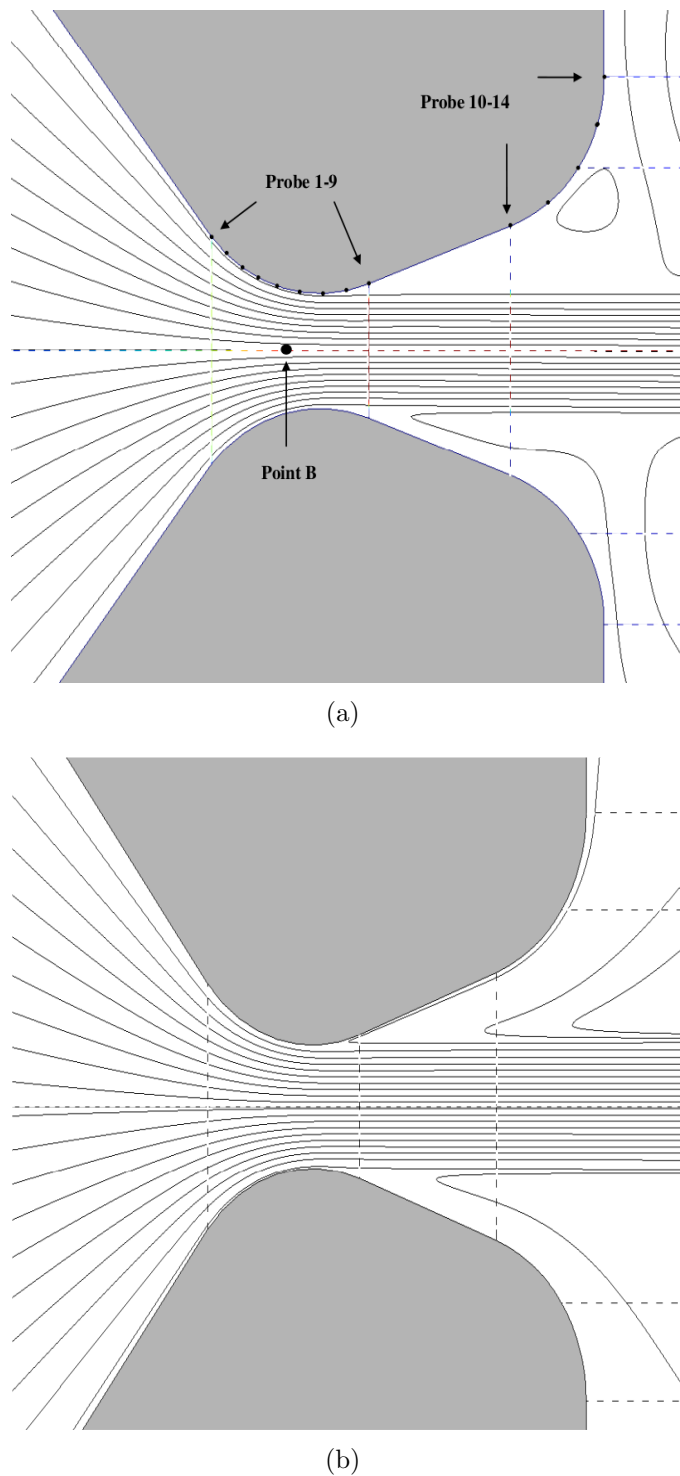


Figure 4–2: Computational fluid streamlines in divergent shape (a) Dynamic simulation (b) Steady simulation

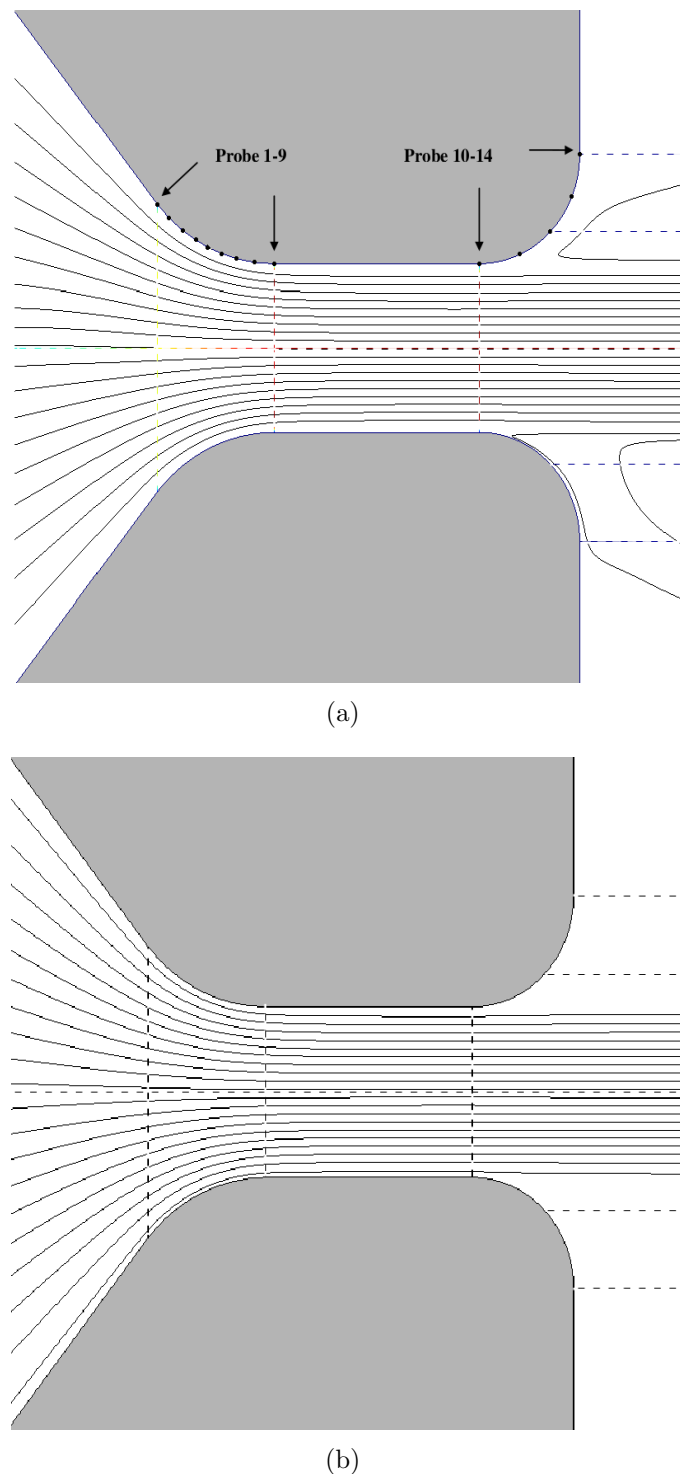


Figure 4–3: Computational fluid streamlines in parallel shape (a) Dynamic simulation (b) Steady simulation

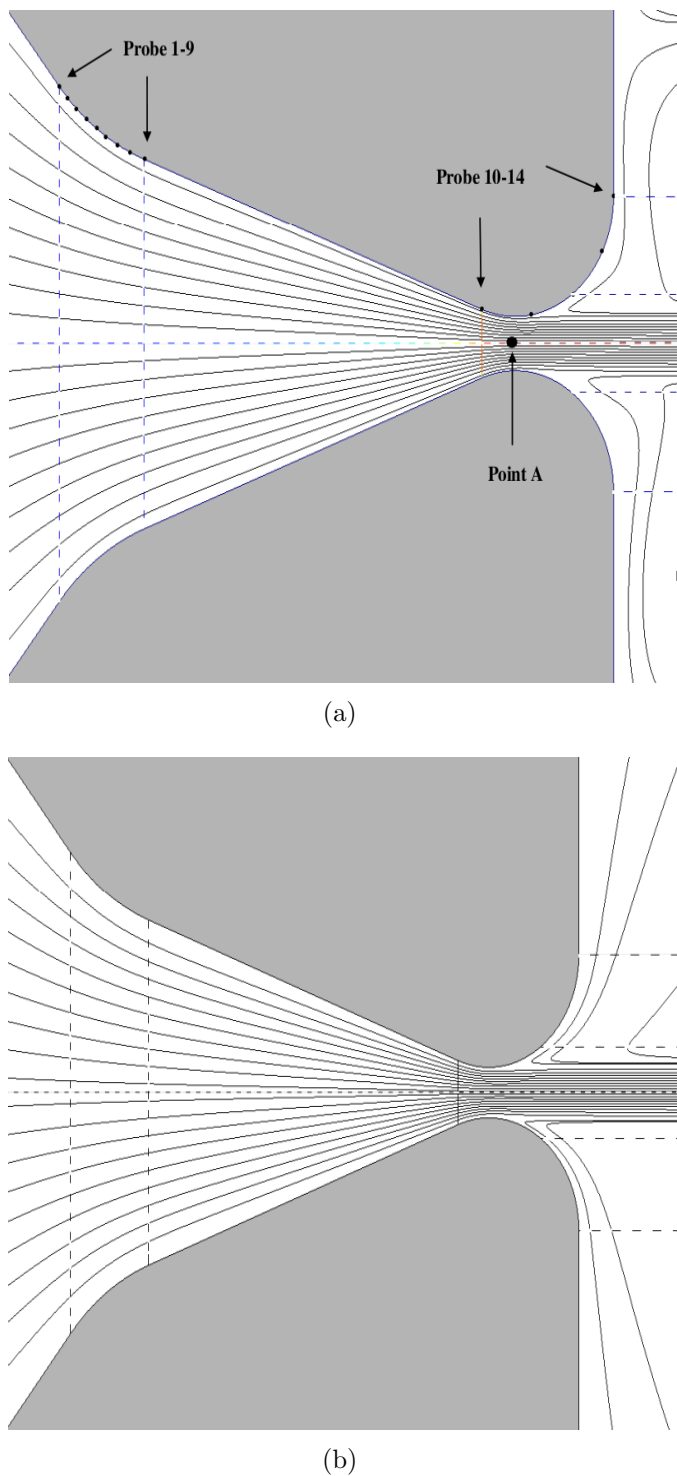


Figure 4–4: Computational fluid streamlines in convergent shape (a) Dynamic simulation (b) Steady simulation

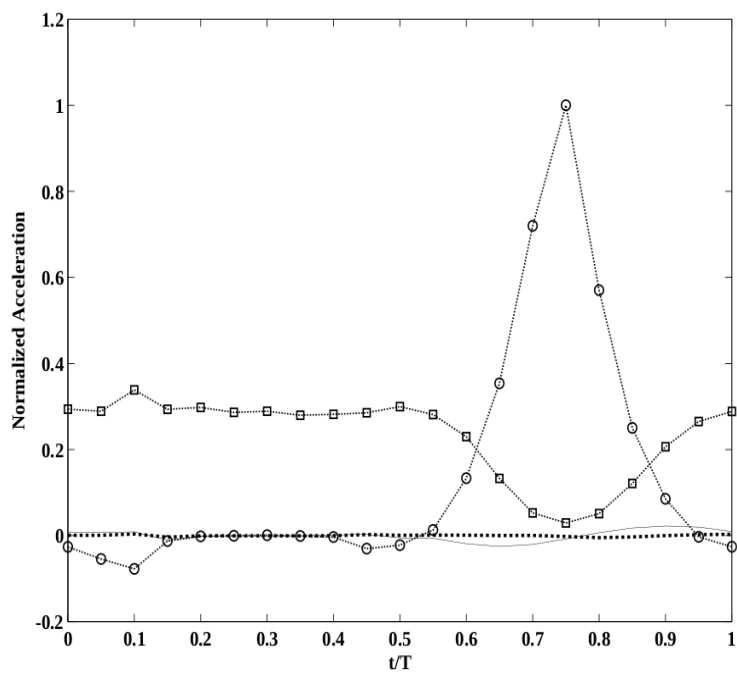


Figure 4–5: Convective and local accelerations for point A and B: $\cdots \circ \cdots$:Convective acceleration at A $\cdots \square \cdots$:Convective acceleration at B, — Local acceleration at A, \cdots : Local acceleration at B

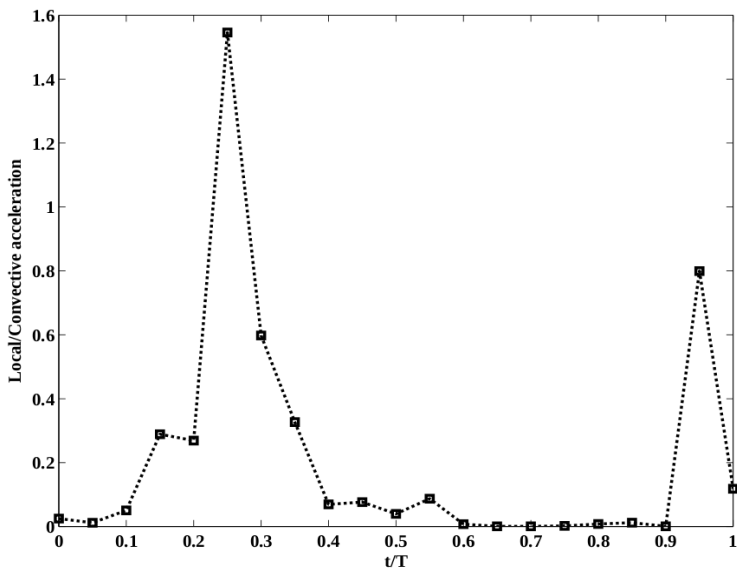


Figure 4-6: Ratio of the local acceleration to the convective acceleration for point A

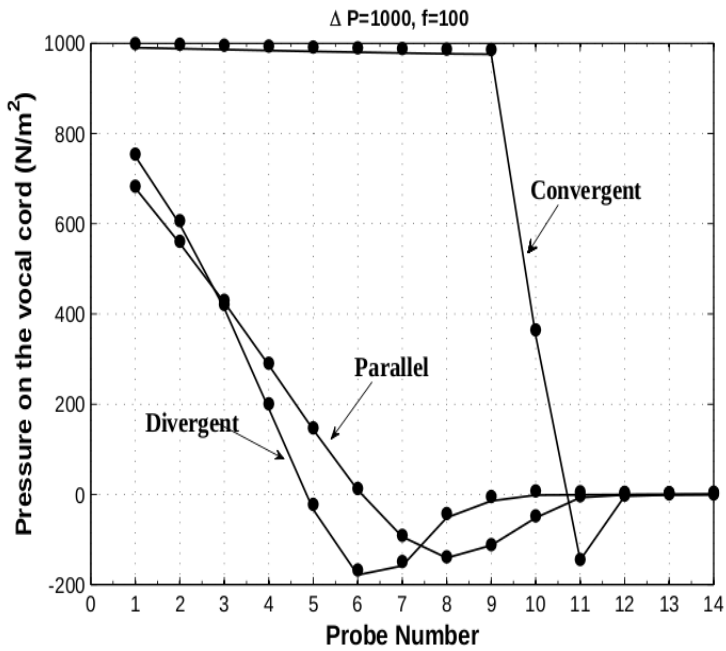


Figure 4-7: Glottal wall pressures for dynamic and static simulations at 14 virtual probes for divergent, convergent and parallel glottal shape

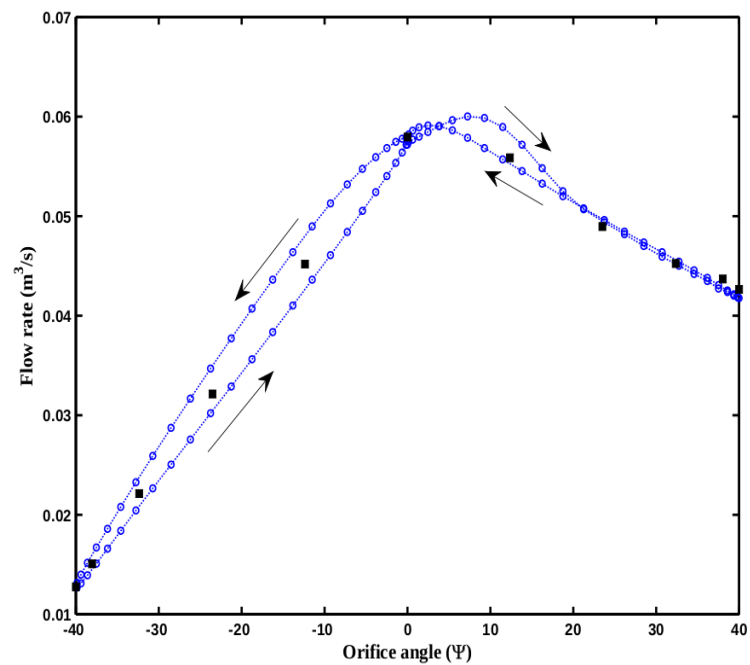


Figure 4–8: Flow rate vs. orifice angle over one cycle ■: static, ···○···:Dynamic

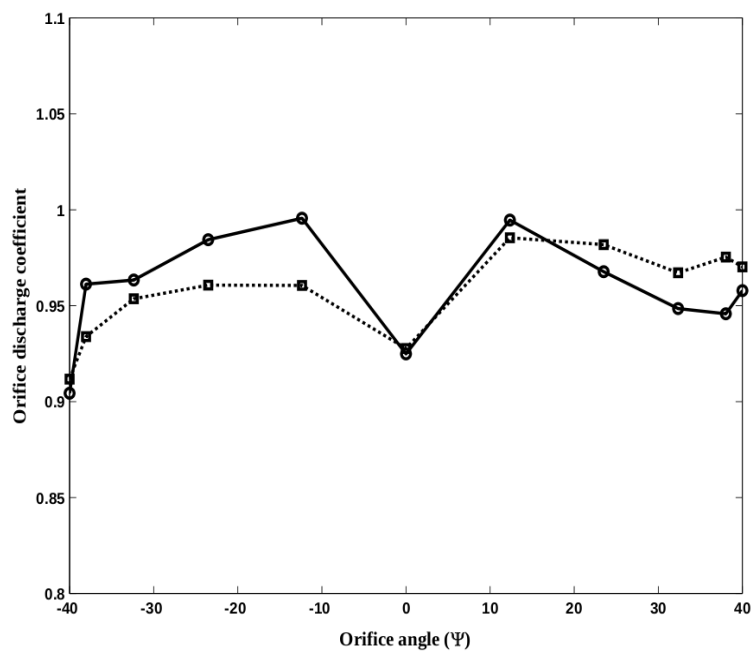


Figure 4–9: Orifice discharge coefficient over half a cycle model – \circ – : static ,
... \square ... dynamic

CHAPTER 5

Numerical simulations of the airflow in subject-specific airway models

5.1 Introduction

Numerical simulations of the airflow in two of the human-specific models described in chapter 2 were performed, and aerodynamic results were compared. One of the models was for a healthy subject. The second model was a postsurgical geometry from a patient with cancer.

A frontal CT scan image was used to create a 2D computational domain. Planar flow simulations were performed with boundary conditions identical to those of the 3D simulation. Flow parameters such as the orifice discharge coefficient, the jet flow deflection and secondary flows were compared with those of the corresponding planar model. Significant differences in flow features between the 2D and 3D simulations were observed. These differences highlight the 3D nature of the fluid flow inside larynx. The importance of using realistic geometries for simulation of voice production was assessed through comparisons with the results from idealized orifice profiles.

5.2 Creation of solid models from CT scan

The procedure for the creation of solid models from CT scan data is described in chapter 2. Two reconstructed 3D models were used for performing numerical airflow simulations. The cross sections of the models before and after smoothing are shown in figure 2–3. The first model was for a healthy subject, as shown in figure 2–3(b). The second model, shown in figure 2–3(c), pertains to the post-surgery data of a

patient with cancer. The post-surgery images were taken during phonation, with the vocal folds adducted. Due to tissue removal, asymmetry between the right and left folds was observed for the described subject model . The vocal tract and the glottis constitute the airway, defined as the hollow space within the larynx and between the vocal folds, respectively. In numerical flow simulations, these cavities substitute the computational domain. The smoothed healthy and post-surgery computational domains with their corresponding sagittal CT scan images are shown in figures 2–4 and 2–5 respectively.

5.3 Numerical procedures

5.3.1 Lattice Boltzmann method

The lattice-boltzmann equation has the following form (Chen & Doolen, 1998):

$$f_i(\mathbf{x} + c_i \Delta t, t + \Delta t) - f_i(\mathbf{x}, t) = -\frac{\Delta t}{\tau} (f_i(\mathbf{x}, t) - f_i^{eq}(\mathbf{x}, t)) \quad (5.1)$$

where $f_i(\mathbf{x}, t)$ is the single-particle probability distribution function at position \mathbf{x} , with a particle velocity c_i in the i^{th} direction at time t . The term on the left hand side is the streaming term and the term on the right hand side is the collision term. The collision term models the relaxation of the particles to their equilibrium state, $f_i^{eq}(\mathbf{x}, t)$, using the Bhatnagar-Gross-Krook (BGK) approximation (Bhatnagar et al., 1954). The relaxation time, τ , is related to the kinematic viscosity, ν , through

$$\tau = (\nu + 0.5) / T, \quad (5.2)$$

where T is the lattice temperature, which is set to $T = 1/3$ for isothermal simulations. Macroscopic variables are obtained from summations of the zeroth and the first order

moments of the distribution function given by

$$\rho(\mathbf{x}, t) = \sum_i f_i(\mathbf{x}, t) , \quad (5.3)$$

and

$$\rho\mathbf{u}(\mathbf{x}, t) = \sum_i c_i f_i(\mathbf{x}, t) . \quad (5.4)$$

The D3Q19 model (Chen et al., 1997; Qian et al., 1992) is used in the commercially available Powerflow[©] software. The local equilibrium distribution function has the form

$$f_i^{eq} = \rho w_i \left[1 + \frac{c_i \cdot \mathbf{u}}{T} + \frac{(c_i \cdot \mathbf{u})^2}{2T^2} - \frac{\mathbf{u}^2}{2T} + \frac{(c_i \cdot \mathbf{u})^3}{6T^3} - \frac{c_i \cdot \mathbf{u}}{2T^2} \mathbf{u}^2 \right] , \quad (5.5)$$

in which the weighting parameters, w_i , are

$$w_i = \begin{cases} 1/18 & \text{for } i=0\dots5 (\text{coordinate direction }) \\ 1/36 & \text{for } i=6\dots17 (\text{bi-diagonal direction}) \\ 1/3 & \text{for } i=18 (\text{rest of particles}) \end{cases} \quad (5.6)$$

Ease of parallelization and handling complicated geometries and boundary conditions are advantages of lattice-Boltzmann method over the conventional Navier-Stokes solvers. More details about this method can be found in the literature (Chen & Doolen, 1998; Chen et al., 1992; Qian et al., 1992).

5.3.2 Computational setup

Three-dimensional accurate geometry

A pressure gradient of $600Pa$ was applied between the inlet and outlet of the computational domains. The inlet is located near the end of the trachea and the

beginning of the larynx as shown in figures 2–4 and 2–5, The outlet is 1-2 cm above the vocal fold, below the epiglottis. Inlet, outlet and glottis areas for both 3D cases are listed in table 5–1.

Case	Inlet area(mm^2)	Outlet area(mm^2)	Glottis area(mm^2)
Healthy vocal folds	253.7	303.5	45.9
Post-surgery vocal folds	304.3	313.7	43.3

Table 5–1: Inlet, outlet and glottis areas for both healthy and postsurgical geometries

A no-slip boundary condition was applied on the walls. The Reynolds number was defined based on the characteristic length $10mm$ and the characteristic velocity $1m/s$ and the air viscosity. The subglottal diameters are different for two geometries and similar characteristic values were used for both simulations to have equal Re numbers, $Re = 1351$. It should be noted that this Re number was chosen before starting the simulation. The characteristic length and velocity are inputs for the software to start the simulation. A maximum expected velocity magnitude was also set before staring the simulation. After performing the simulation and post-processing the results, the maximum obtained velocity were compared to the maximum expected velocity. The calculated maximum velocity magnitudes were smaller than the expected maximum velocity verifying the accuracy of the simulations.

To reduce the computational cost, the domains were decomposed into variable resolution (VR) regions. Each VR region is assigned with a resolution level. Each grid cell called “voxel” is cubic in shape and the voxel size between subsequent VR levels changes by factor of two. Because cells are cubic in shape the number of grid points increases by factor of eight between two subsequent VR regions. To resolve the boundary layer, the highest VR region with the finest voxel size was defined to be an

inward offset layer of the larynx wall with the thickness of 0.5 mm . Six VR regions were defined. The resolution of the finest VR region for both cases is 80 cells/mm which resulted in more than 62 and 55 million cells for healthy and post-surgery vocal fold geometries respectively. The computational domain of healthy geometry with mesh grid is shown in figure 5–1.

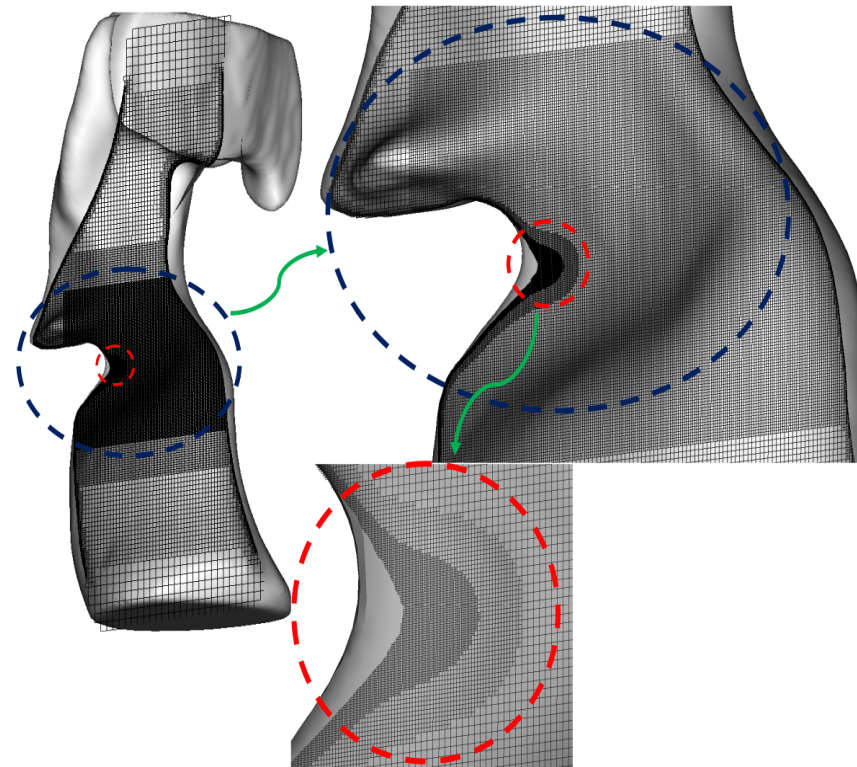
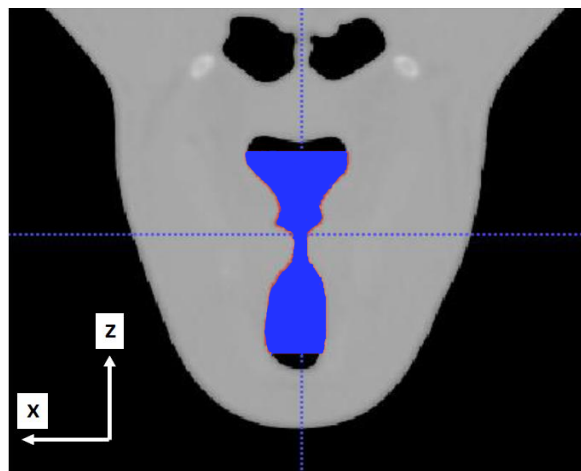


Figure 5–1: Computational domain for the healthy subject

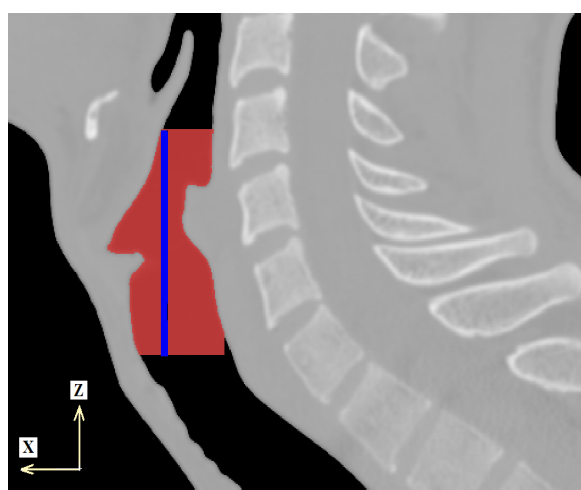
Two-dimensional models

3D simulation results for the healthy configuration were compared with a 2D computational model made from the same CT scan data. The planar 2D cross section was extracted from one frontal CT scan image. The computational domain is shown

on the selected frontal CT image in figure. 5–2(a). The location of the selected frontal plane is shown as a thin rectangular bar on the mid-sagittal plane in figure.5–2(b). The selected cross-section is closer to the anterior commissure because the vocal folds, the false vocal folds and the laryngeal ventricles can be seen more easily rather than sections closer to the posterior commissure. The open source software SALOME was used for mesh generation of the 2D simulations. The pressure gradient and the boundary conditions were the same as for the corresponding 3D case.



(a)



(b)

Figure 5–2: 2D computational domain on the (a) frontal (b) sagittal CT image

5.4 Results

5.4.1 Three dimensional models

For the 3D cases the computational time was approximately one week to converge using 128 processors in parallel on the Colosse computer cluster at McGill University. Physical time scaling for the healthy and post-surgery cases are $3.031e - 08s$ and $6.567e - 08s$ respectively. To ensure the convergence of the simulations, one virtual probe was located near the outlet and the velocity magnitude and the pressure were recorded every 500 time steps. Simulations were evolved until average velocity and pressure became reached a steady state. The convergence criteria, 5.7 and 5.8, were satisfied.

$$\frac{\bar{U}_n - \bar{U}_{n-1}}{\bar{U}_n} \leq 0.01 , \quad (5.7)$$

and

$$\frac{\bar{P}_n - \bar{P}_{n-1}}{\bar{P}_n} \leq 0.01 \quad (5.8)$$

were used, where U_n and P_n are the n_{th} recorded velocity and pressure magnitude respectively. The time-averaged velocity, \bar{U}_n , and the average pressure, \bar{P}_n , were calculated using equations 5.9 and 5.10.

$$\bar{U}_n = \frac{1}{n} \sum_1^n (U_n) , \quad (5.9)$$

and

$$\bar{P}_n = \frac{1}{n} \sum_1^n (P_n) \quad (5.10)$$

It took 1.4 million time steps for healthy and 500,000 time steps for post-surgery case to converge. That is due to the larger size of the computational domain for the healthy geometry.

The velocity fields for both healthy and post-surgery geometries using mid-coronal and three transverse planes in subglottal, intraglottal and supraglottal regions are shown in figures 5–3(a) and 5–3(b). The mid-coronal section overlapped with streamlines is shown in figures 5–3(c) and 5–3(d). The streamlines are more parallel in the post-surgery configuration than in the healthy vocal folds. That is because the orifice area is smaller in the post-surgery geometry than in the healthy one. From the frontal and transverse plane, it can be observed that the velocity profile and streamlines are less symmetric in the post-surgery shape than in the healthy one. That may be due to the asymmetry of the post-surgery geometry.

Sagittal cross section views are shown in figures 5–4(a) and 5–4(b). In contrast to mid-coronal planes, flow separation and the jet plumes can be observed for both geometries in the mid-sagittal planes. For the healthy geometry, the anterior and posterior boundaries of the jet plume converge toward the center. For the post-surgery model, jet plume boundaries are parallel. Sections of the vocal fold are removed, which altered the orifice geometry and caused asymmetry between the left and right vocal fold. Although the post-surgery geometry is related to phonation, a large gap between the folds was observed, and the fluid flow rate is thus relatively high. That is consistent with the breathy voice of patients with massive tissue removal which prevents a complete closure of vocal fold.

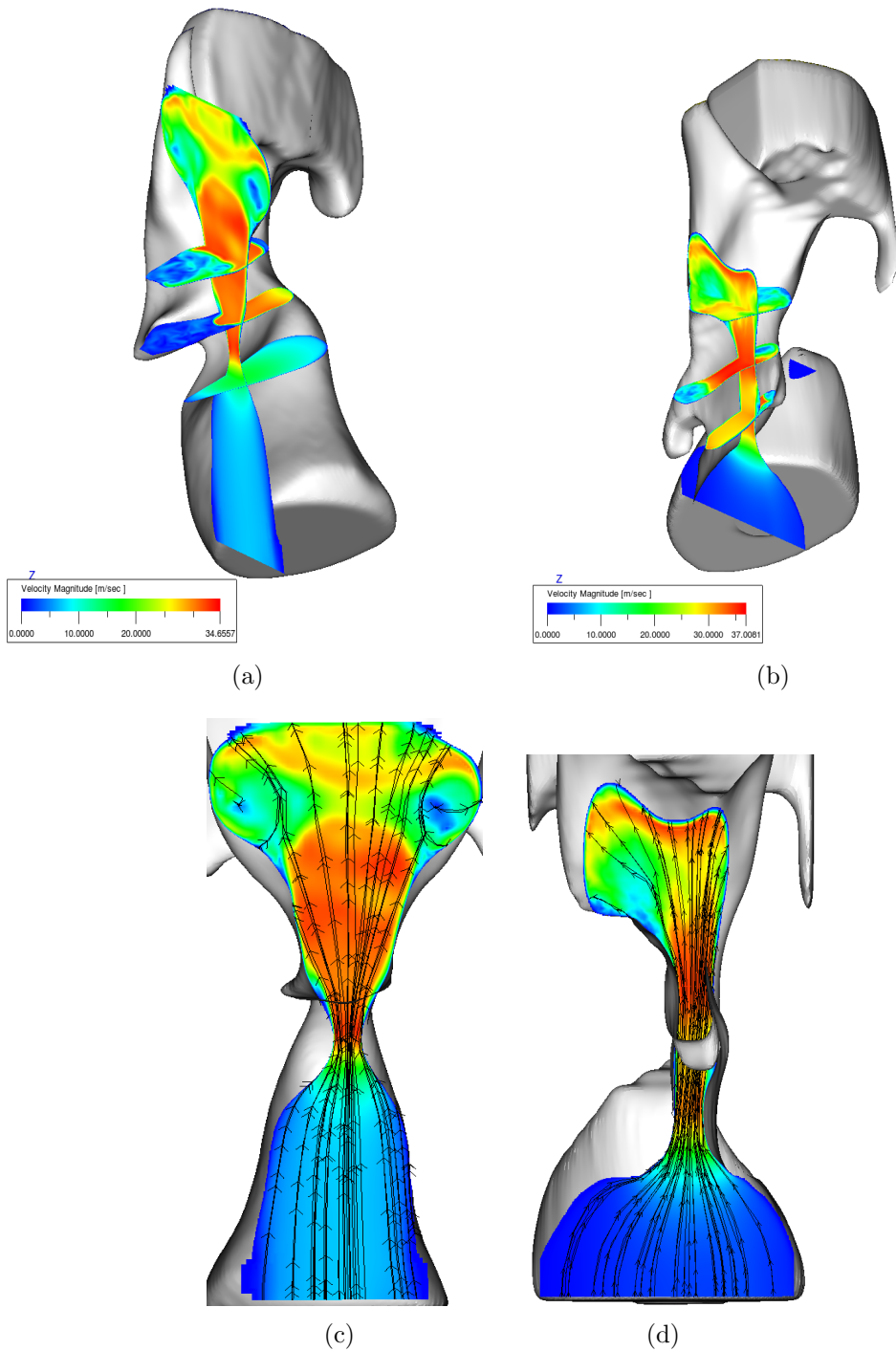


Figure 5–3: Velocity profile is shown on a mid-coronal and three transverse planes for (a) healthy (b) post-surgery geometry. Mid-coronal slice overlapped with streamlines for (c) healthy (d) post-surgery vocal folds

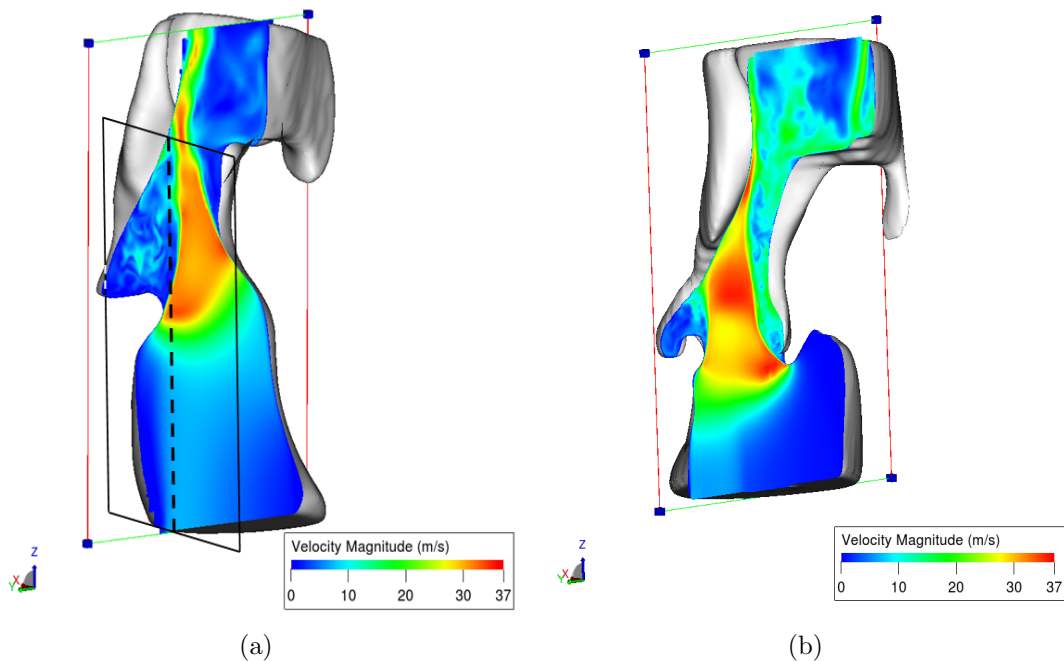


Figure 5–4: Velocity profiles in the mid-sagittal cross section (a)healthy geometry
(b) post-surgery vocal folds

5.4.2 Two dimensional model

The velocity field and streamlines in the 2D model and the corresponding planar section in the 3D simulation are shown in figures 5–5(a) and 5–5(b) respectively. Significant differences between the results are observed. In the 2D simulation, figure 5–5(a), flow separation from the orifice wall is observed. The separation point is located slightly after the minimum constriction point. The Coanda effect James (1977) is observed between the glottis and the false folds. Fluid flow through the orifice deviates from a straight path and bends toward one wall. These differences are mostly due to the intrinsic differences between a 2D and a 3D simulation. It should be noticed that the location of the selected 2D cross sections in the anterior-posterior direction has a significant effect on the net fluid flow through the 2D slice in 3D simulation (figure 5–5(b)). In figure 5–4(a) the location of the 2D coronal plane (parallel to X-Z plane) is shown. The dashed-line shows the intersection between the mid-sagittal plane and the planar section. This intersection is closer to the anterior commissure and from figure 5–4(a) it is seen that the fluid coming out of the glottis converges rapidly toward the posterior wall and the jet plume has a noticeable distance from the 2D slice plane. As a result, the fluid flow rate in the planar section of the 3D simulation is lower than that for the 2D simulation.

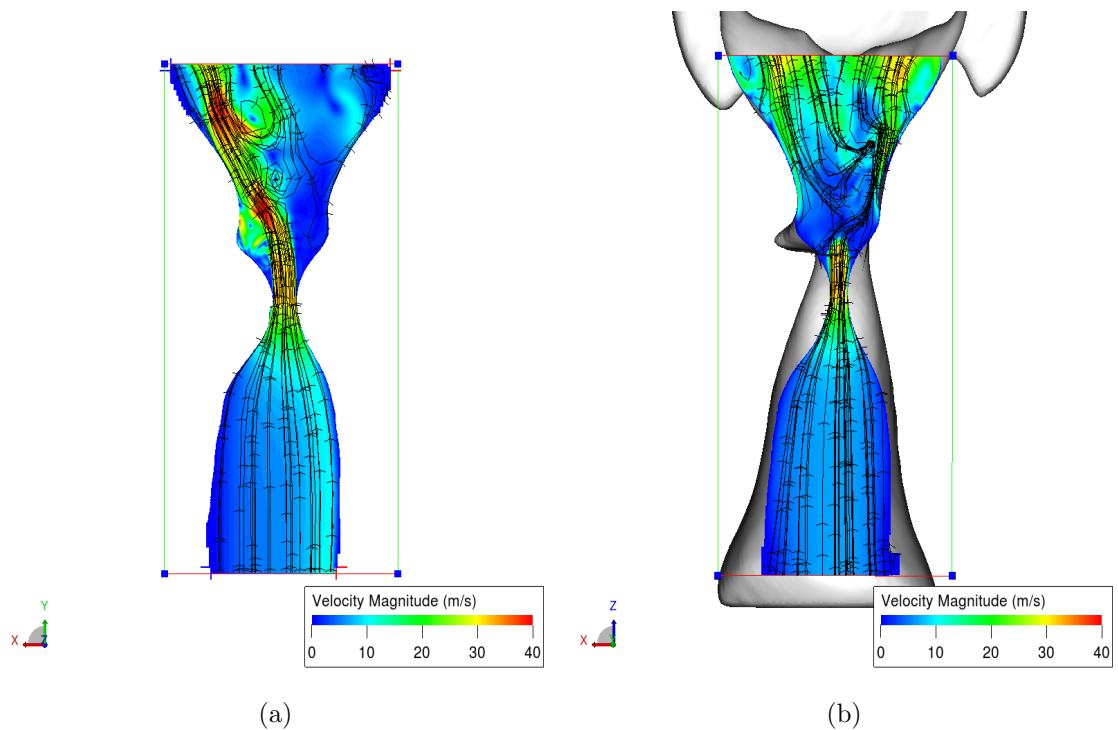


Figure 5–5: Velocity profile in (a) 2D cross section (b) corresponding slice of 3D simulation

5.5 Discussion

5.5.1 Orifice discharge coefficient

The orifice discharge coefficient, C_d , was used to compare glottal airflow in series of static orifices and a dynamic one to validate quasi-steady approximation in section 4.3.5 and in the study of Park & Mongeau (2007). The orifice discharge coefficient, C_d , is defined as the ratio of the actual flow rate, Q_{real} , to the product of minimum orifice area, A_m , and centerline velocity component normal to the minimum area plane (Park & Mongeau, 2007)

$$C_d = \frac{Q_{real}}{A_m \cdot u}. \quad (5.11)$$

It can also be defined as the ratio of actual fluid flow rate to the ideal flow rate with Bernoulli velocity. i.e.,

$$C_d = \frac{Q_{real}}{A_m \cdot \sqrt{\frac{2\Delta P}{\rho}}}. \quad (5.12)$$

The radiated sound pressure can be described as a function of C_d (Park & Mongeau, 2007). Orifice discharge coefficient includes the effects of viscous losses, contraction in geometry and pressure head loss along a streamline passing through the centerline (Park & Mongeau, 2007).

The cross-section area is a key parameter in both C_d definitions. The accurate calculation of the minimum area and the determination of its location is very challenging in 3D cases. The posterior commissure is located higher than the anterior commissure. The anterior-posterior commissure axis is therefore not horizontal. As a result, the minimum area plane is not parallel to the transverse planes. Furthermore, for the post-surgery model, pathological effects and surgery have changed the

geometry and it even makes it more difficult to choose the minimum area plane. Due to these difficulties, the transverse plane at the posterior commissure level was used to calculate the minimum area for both geometries.

Case	Healthy vocal folds	Post-surgery vocal folds	2D
C_d	0.62	0.50	0.89

Table 5–2: Comparison between C_d s for different cases

Table 5–2 shows the C_d values calculated from Eq. 5.11. The orifice discharge coefficient, C_d , for the healthy vocal fold is larger than that of the post-surgery vocal folds. This is consistent with results from Park & Mongeau (2007), which showed that C_d is increased as the orifice area is increased. Although the post-surgery model is for a phonatory condition, there is no significant differences between the C_d values between the healthy and post-surgery models. The relatively large gap between the folds in the post-surgery geometry decreased the difference between the orifice discharge coefficients. A noticeable difference between C_d of 2D and 3D cases was obtained. That could be due to a boundary layer effect. In the 3D model, boundary layers are established around the entire periphery of the glottis. This increases the viscous and pressure head losses in the fluid. However, for 2D case, it is assumed that the anterior-posterior direction is long enough to be ignored and only side wall effects are considered.

The gauge pressure variation along the inferior-superior direction on a two centimeter long line are shown for both the 2D and 3D cases in figure 5–6. The glottis is located at the origin and negative and positive locations designate the subglottal and supraglottal regions, respectively. It can be observed in figure 5–6 that the pressure

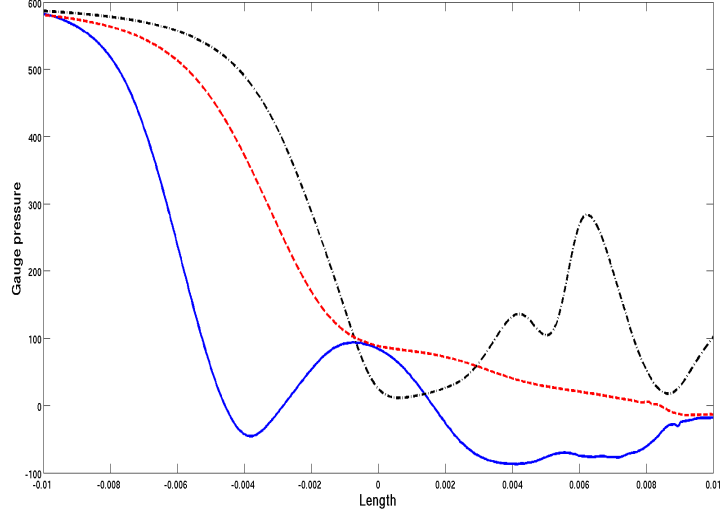


Figure 5–6: Gauge pressure distribution along the inferior superior direction, Dash line (- -): 2D model, Dash dot line (.-): Open-shape, Solid line(—): post-surgery

drops as the fluid moves toward the glottis for all cases. A greater pressure recovery was observed in the supraglottal region, near the false folds, for 2D case rather than 3D cases. That reduces head loss and increases C_d for 2D case. The post-surgery geometry has the highest pressure drop which resulted in the lowest C_d .

The flow resistance of the subglottal and supraglottal regions was calculated. To eliminate the length effect, a two-centimeter section of the larynx including the glottis in the middle was selected for all cases. The flow resistance was calculated from Eq.5.13

$$R_f = \frac{\Delta P}{Q_{real}} \quad (5.13)$$

The flow resistance values for the 2D and 3D cases are shown in table 5–3. The

Case	Healthy vocal folds	Post-surgery vocal fold	2D
$R_f(\frac{Pa\cdot s}{cm^3})$	0.631	0.882	0.01

Table 5–3: Comparison between fluid resistances for different cases

2D model has the lowest resistance and the post-surgery model has the highest fluid resistance. A higher flow rate and a larger pressure recovery for the 2D geometry resulted in lower flow resistance.

5.5.2 Flow asymmetry

The intraglottal flow asymmetry depends on several parameters such as geometric asymmetries between the left and right fold, surface roughness (Erath & Plesniak, 2006a,b,c) and also jet confinement, jet pulsatility and intrinsic instabilities of the glottal jet (Zheng et al., 2011a). Furthermore, instabilities in one location may propagate and change the flow structure in another region (Mittal et al., 2013) and that suggests the important role of the supraglottal flow in the glottal jet flow deflection (Zheng et al., 2009; Luo et al., 2008; Neubauer et al., 2007).

Among these parameters, the focus of the present study is on the effects of utilizing accurate 3D geometry of the larynx and vocal folds in glottal flow simulations. Comparison between the fluid flow in the healthy and post-surgery geometries shows the important role of the glottal geometry in the jet asymmetry. Due to the asymmetry in the glottal geometry in post-surgery case, the streamlines in figure 5–3(d) are less symmetric than those of the healthy geometry, figure 5–3(c). A significant jet deflection is seen in the 2D simulation however, this asymmetry is not seen in the 3D realistic models, figures 5–3(c) and 5–3(d). That is consistent with the findings of Triep and Brucker that the jet skewing in the supraglottal regions is greatly decreased

in 3D jets (Triep & Brücker, 2010). Zheng *et al.* also confirmed that the more realistic geometries resulted in the less flow structure asymmetry (Zheng et al., 2011a). It seems that realism of the experimental and computational models will decrease the flow variability (Mittal et al., 2013). That is closer to the previous research suggesting that the Coanda effect cannot be generated in phonatory jets (Pelorson et al., 1994; Hofmans et al., 2003). Matteus and Brucker also suggested the cautious interpretation of the jet asymmetry in simplified models and according to their findings, the Coanda effect might not be a relevant flow feature in glottal jet flow (Mattheus & Brücker, 2011). These differences underline the significant effects of the geometry on glottal flow features.

5.5.3 Secondary flow

Figures 5–4(a) and 5–4(b) show the velocity gradients along the anterior-posterior direction and the resulting pressure gradient in this direction in the supraglottal region. These figures also clearly show the jet Vena contracta in the mid-sagittal plane in the supraglottal region. This is consistent with the observations of Khosla *et al.* in their PIV measurements of the glottal airflow in canine larynges (Khosla et al., 2008). The reported jet widening in the midcoronal plane and jet narrowing in the midsagittal plane demonstrate the phenomenon of jet axis switching (Khosla et al., 2008). In 2D simulations, the plane of the computational domain is parallel to the frontal plane and as a result, the anterior-posterior velocity, V_y , and the pressure gradient along this direction are ignored. Only the velocity component along the inferior-superior direction, V_z , is considered. However, for 3D glottal models, V_y is not negligible because of the presence of secondary flows in the glottis.

To better show the secondary flow in the glottis, velocity vectors within the transverse plane at the level of glottis are shown schematically in figure 5–7. The transverse velocity profile along the anterior-posterior direction is also shown in figure 5–7. One can observe that V_y has a greater amplitude near the anterior and posterior commissures than towards the mid-coronal regions. The presence of the secondary flow in the transverse plane has been previously reported for 3D glottal orifices (Scherer et al., 2010).

The maximum value of V_y occurred near the anterior commissure, as shown in figure 5–7. This has been previously reported in several excised larynx experiments e.g (Khosla et al., 2008; Berke et al., 1989; Alipour & Scherer, 1995; Bielamowicz et al., 1999).

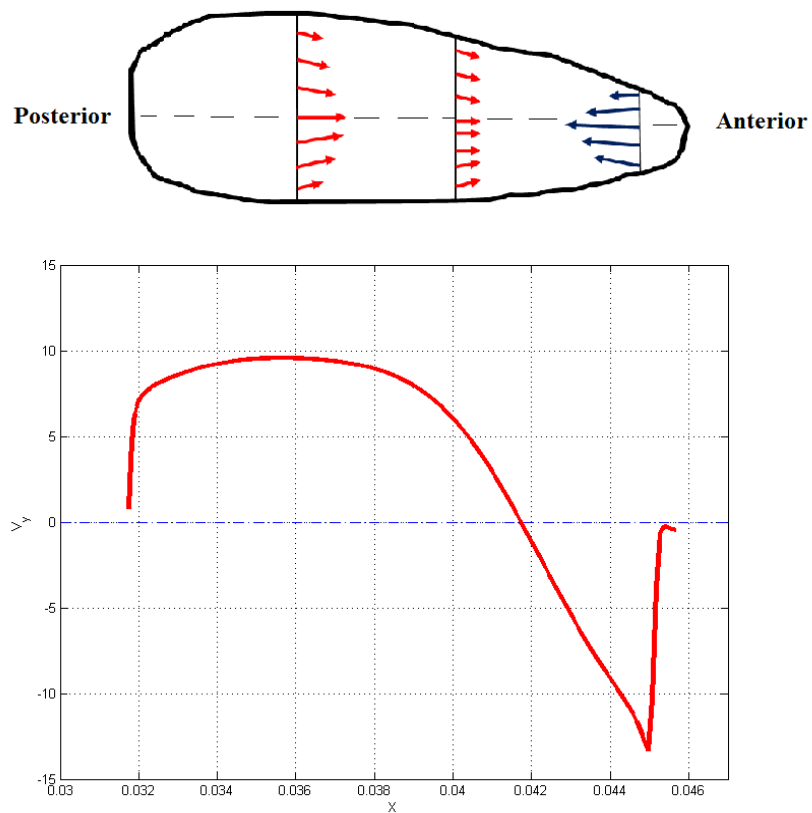


Figure 5–7: V_y Velocity profile on the transverse plane at the glottis level and the velocity profile on the anterior-posterior line

CHAPTER 6

Determination of strain field on porcine excised larynges using DIC

6.1 Introduction

Optical measurements of vocal fold vibrations along with digital image correlation (DIC) may improve the determination of time-dependent strains on the superior surface of the vocal folds. Further analysis and constitutive relations allow the estimation of the mechanical stress field within the mucosa. Measurements were performed using excised porcine larynges on a humidified flow bench, equipped with high-speed cameras and a commercially available DIC software. Measurement data for adducted and freely-suspended vocal folds were used to estimate the distribution of the initial prephonatory strain field. The use of DIC in the excised larynx setup led to accurate measurements of the vocal fold displacement field. Surface deformations were estimated from digital images recorded at 3000 frames per second during continuous self-oscillation in four excised porcine larynges. Porcine larynges have been used in excised larynx experiment (Alipour & Jaiswal, 2008, 2009). Alipour & Jaiswal (2008) examined the phonatory characteristics of pig, sheep and cow larynges. The glottal resistance of the excised pig, sheep and cow larynges was measured by Alipour & Jaiswal (2009).

Larynx preparation consisted of removing the supraglottal wall and the false folds. Two high-speed cameras recorded the images from different angles. DIC yielded the deformation field on the superior visible surface of vocal folds. An

isotropic constitutive law, the polymer eight-chain model, was used to estimate the surface distributions of planar stresses from the strain data. The Lagrangian strain values were between $\sim 16\%$ and $\sim 29\%$ along the anterior-posterior direction of the four porcine vocal folds. In contrast to previously observed kinematical characteristics of silicon models, the motion of material points on the vocal fold surface had an elliptical trajectory during oscillation. A phase difference was observed between the anterior-posterior displacement and the medial-lateral displacement. DIC analysis for the planar projection of tissue movements, and use of the eight-chain model, displayed a maximum body stress of ~ 4 kPa along the medial-lateral direction on the superior surface.

6.2 Methods

6.2.1 Sample preparation

Porcine larynges were obtained from a local abattoir and transported to the laboratory while immersed in a 0.9% saline solution. A 3-cm long section of the trachea attached to the larynx was kept to facilitate connection to the airflow pipe. A standard snap-freezing protocol was used while each larynx was submerged in normal phosphate saline buffer. On the day of the experiment, they were thawed at room temperature; then, the surrounding connective soft tissues were removed and the superior part of the larynx, above the false folds, was dissected as shown in figure 6–1A. This was performed by cutting the thyroid cartilage along the midline to the level of the false folds and continuing laterally to both left and right sides (dashed lines in figure 6–1A). The false folds in figure 6–1B were subsequently removed using small scissors to reveal the vocal folds as shown in figure 6–1C. The epiglottis, which

is located in the posterior glottis, was removed completely. A thin string was passed through the arytenoid cartilage laterally as suggested by (Alipour & Jaiswal, 2009). This string was attached to a pulley-weight system that was designed to pull the

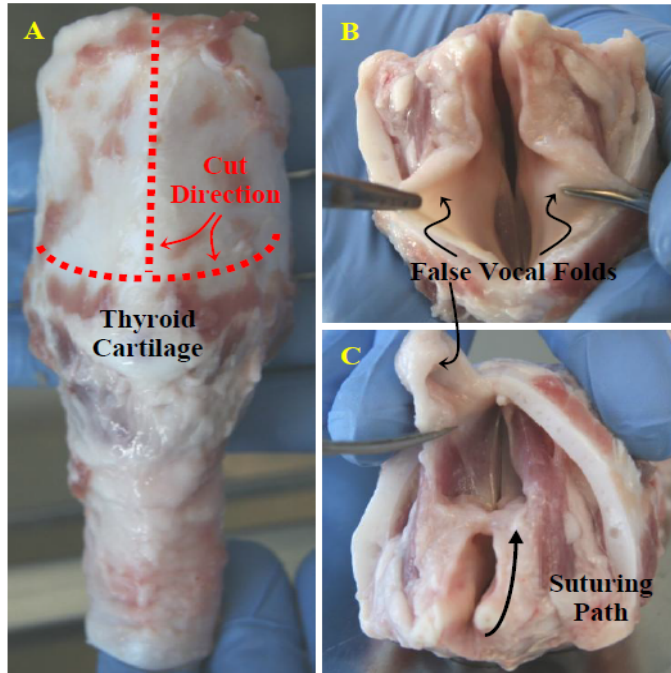


Figure 6–1: Dissection of porcine larynx, (a) Dash-lines show the direction of dissection on the thyroid cartilage, (b) False folds in porcine larynx, (c) Cutting the false folds to reveal the vocal folds.

arytenoids anteriorly (figure 6–2). The required tension on the vocal folds for proper oscillation was applied using the known weights. The large gap in the posterior glottis was sealed using surgical sutures beginning at the upper arytenoid and continuing to the most posterior part of the vocal folds, as shown in figure 6–1C.

6.2.2 Experimental apparatus

A test frame (80/20 Inc., Columbia City, IN) was mounted on an optical table (ThorLabs, Newton, NJ) to install and stabilize the sample holder, digital cameras

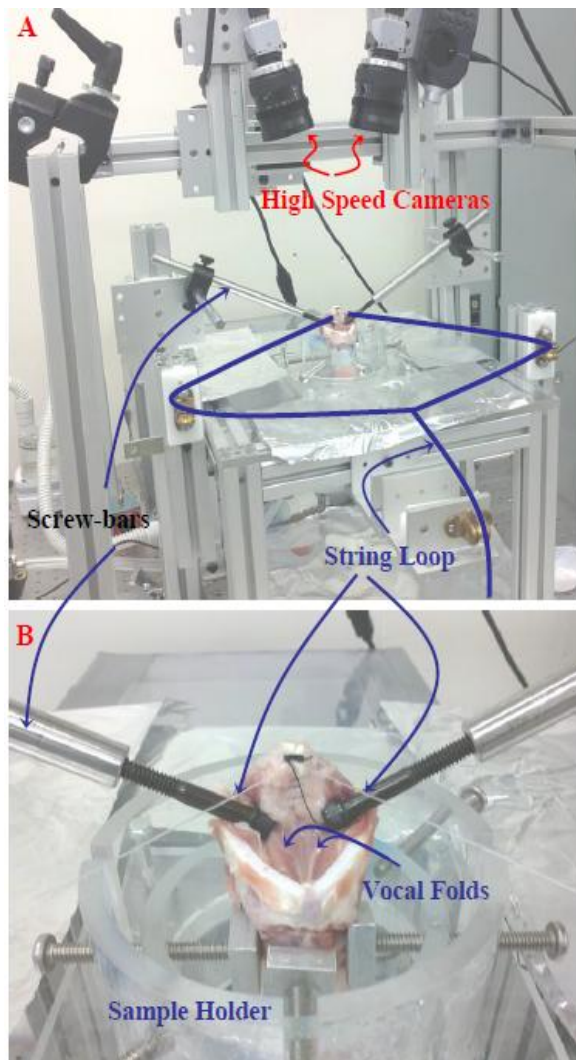


Figure 6–2: (a) Excised larynx set-up (b) Larynx holder

and a light source (figure 6–2). The system was assembled using aluminum bars (T-slotted profiles), plastic sliders, steel bolts and Plexiglas plates. The holder frame is made of a transparent Plexiglas plate that facilitates the connection of the larynx and tubes. The cylindrical sample holder has four adjustable screws with flat heads to maintain the larynx. The trachea was glued to a polyvinyl chloride (PVC) tube

(McMaster-Carr, Chicago, IL) with an outer diameter of 1/2' (0.0127 m) or 5/8' (0.0159m), depending on the size of the larynx, to mount the larynx on the test bench. Two screw bars were placed on the posterior part of the folds. The pulley-weight system and the screw bars were used to apply the required tension on the vocal folds to initiate self-oscillations. A sutured larynx, attached to the pulley-weight system and the sample holder are shown in figure 6–2. Any play in the larynx support could move the speckled region of interest out of the camera's focus area. To minimize vibration in the setup, the camera frame and the sample holder frame were attached to the optical table.

Two high-speed black and white cameras (Fastcam MC2 - Model 10K; Photron Limited, San Diego, CA) were installed on the frame using adjustable sliders. Their position could be changed along three spatial directions. Images were taken at a rate of 3000 frames per second to obtain sufficient temporal resolution. A distance of 40 cm between the vocal folds and the cameras was found to provide an optimum field of view. The cameras were equipped with two zoom lenses (EF-S17-85mm; Canon Canada, Mississauga, ON), which allowed for increased resolution during the experiment. A fiber optic light (Model 21-AC; Salem, NH) with two semirigid probes located approximately 8-10 cm away from the vocal fold surface was used to produce sufficient light and reduce glare. The light beam was oriented at an angle of approximately 30 degrees with respect to the horizontal to minimize glare. Other components of the experimental setup are shown schematically in figure 6–3.

A centrifugal blower (D-14.5cm; Ametek Windjammer, Kent, OH) was used as the airflow source. A muffler was used to attenuate noise from the flow supply.

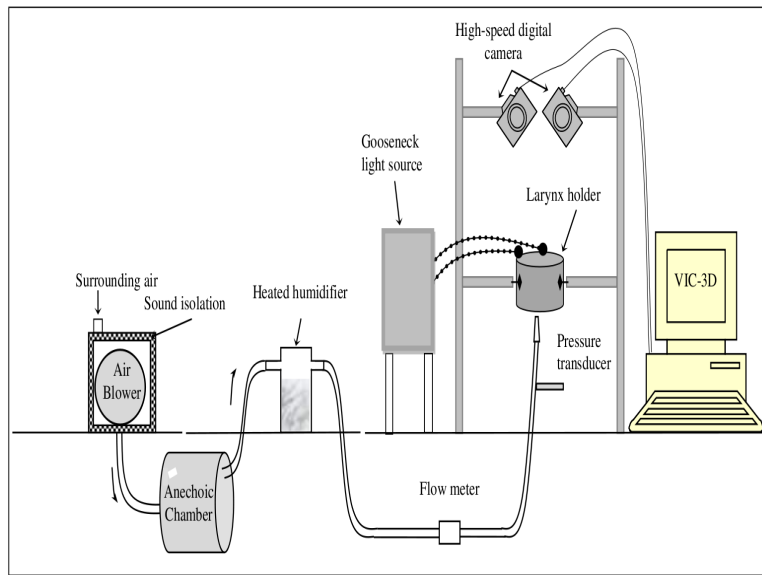


Figure 6–3: Schematic illustration of the excised larynx testbed

Airflow was humidified and heated up to 90-95% and 30 – 37°C, respectively, using a heated humidifier (HC-150; Fisher & Paykel, Mississauga, ON). The time-averaged, mean volumetric flow rate was measured using a flow meter (MKS Instruments, Andover, MA). The static pressure also was recorded at a 1-2 cm distance before the trachea using a hydrostatic pressure transducer (MKS Instruments, Andover, MA). Once the larynx was secured in the holding clamp and attached to the PVC tubing, the air supply was turned on and raised until self-oscillation occurred. Pressure-flow rate measurements for three samples are shown in figure 6–4. Measurements were performed while increasing and decreasing flow rate to capture hysteresis. The pressure recorded while the flow rate was diminished was consistently lower than that recorded while the flow rate was increased. Such a trend was observed for all

larynges tested and is consistent with results from (Alipour & Jaiswal, 2008) during pressure sweep experiments on porcine larynges.

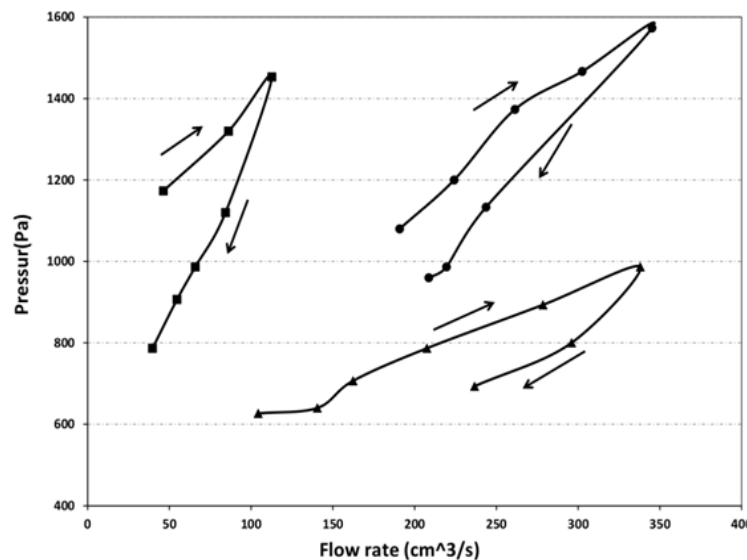


Figure 6-4: Pressure vs. flow rate for three porcine larynges

6.2.3 Digital image correlation

Three-dimensional DIC analyses were performed using the commercially available software VIC-3D and -2D (Correlated Solutions Inc., Colombia, SC). DIC provides surface displacements along three spatial directions from correlations of grayscale patterns between a reference image and successive deformed images. The reference image was typically the image of the tissue at the resting position, prior to oscillations. A randomized speckle pattern was applied on the deformable solid to uniquely identify each material point. As multiple pixels may have the same grayscale value, the program analyzes a square subset of pixels of predetermined size

and calculates the strain as the square is deformed. More details about the algorithm in this program can be found in the literature (Miri et al., 2012b; Chu et al., 1985).

Efforts were made to identify the best dyes to create a robust speckle pattern. The speckle pattern should adhere onto the tissue surface, without diffusing or dispersing out of the tissue. Isotropic diffusion of the pattern causes a uniform distribution that is not appropriate for analysis by VIC-3D. In addition to chemical dyes, cosmetic products, such as foundation sprays and ink powders, as well as food dyes were tested. Powdered dyes such as methylene blue and congo red were tested with multiple solvents including water, corn syrup and barium. Some produced insufficient contrast, or produced a uniform coating rather than local speckles. Contact with humidified air and collision between vocal folds tended to displace or entirely remove the dye. Allowing the dye to dry over periods of 5, 15 or 30 minutes did not resolve the problem. Figure 6–5 shows a summary of different background speckle combinations and the qualitative results. The best results were obtained using a cosmetic facial product and graphite powder. A thin layer of foundation material was sprayed on the vocal fold surface then graphite powder was distributed on the foundation layer. Solid particles of graphite powder do not distribute over the tissue and they reduce the glare during the experiment.

The typical area of interest for DIC analysis and the coordinate system with the origin being in the center of imaged area are shown on the vocal folds with graphite speckle pattern in figure 6–6. The x and y axes are in the medial-lateral and anterior-posterior direction, respectively. The selected area approximately includes the middle half of the vocal folds length (from $-L/4$ to $+L/4$) in the y direction,

SYMBOLS		BACKGROUND					
		SPECKLE					
Ineffective	-	Graphite powder					
Natural	x	Flat enamel paint (Plasti-Kote Black)	-	x			
Effective	+	Black India ink - Graphic (Pebeo)	x				
Excellent	++	Tissue dye (Fisher Scient. Black)					
		Fluorescent yellow (CreateX)					
		Black India ink (ACMI)					
		Flat enamel paint (Plasti-Kote)					
BACKGROUND		Tissue dye (Fisher Scientific Yellow)	+	x	-	+	-
ERA face foundation (Classified Cos - Y1)		-	+	-	-	-	x
ERA face foundation (Classified Cos - R10)		-	-	+	-	x	-
Airbrush legs (Sally Hansen)		x	-	-	x	+	x
Air flash (Dior)		-	-	x	-	-	+

Figure 6–5: The chemical colors used in the experiment and the outcome results

with L being the anterior-posterior length. The areas near the anterior and posterior ends (i.e $y > L/4$ and $y < -L/4$) were excluded from the area of interest for DIC because of very low vibration amplitude in these regions. Figure 6–6 also shows the contour of physical point locations on the superior surface of the vocal fold along the inferior-superior direction (i.e., the z-component).

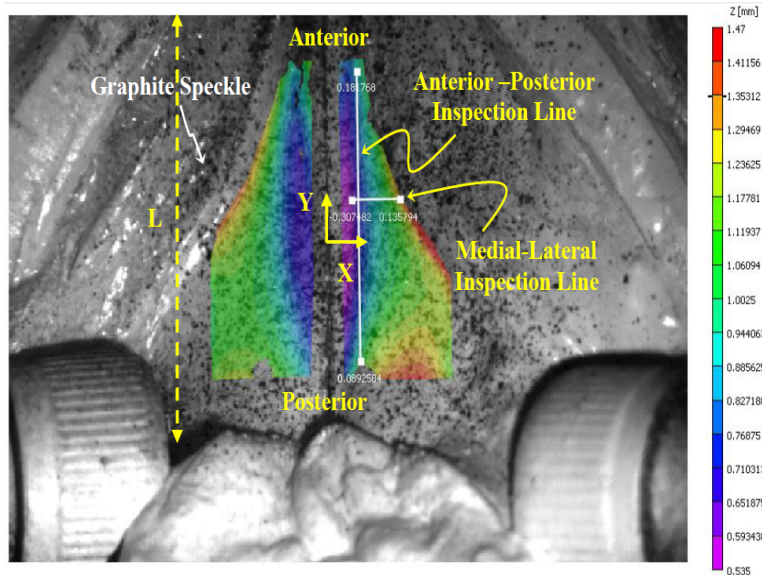


Figure 6–6: Vocal folds with a layer of speckle pattern with the contour of depth position on the superior surface of vocal fold and inspection lines in both anterior-posterior and medial-lateral direction.

6.2.4 Determination of the initial pre-phonatory strain

Vocal folds are initially under tension before phonation onset. In order to prevent the mode change and the frequency jump during oscillation (Alipour & Jaiswal, 2008), which is a very common phenomenon for porcine larynges, further tension was applied to adjust pitch and obtain the sustained oscillation using the pulley-weight system and screw bars. To estimate the effective strains and stresses, the initial strain must be added to the relative strain measured during vibration. The following approach was used to obtain the initial strain field. After recording high-speed images of the vocal folds during self-sustained oscillations, a snapshot of the vocal folds in the resting position (i.e., no airflow passing through the glottal area) was recorded. Using a scalpel and starting at the most anterior part of the vocal

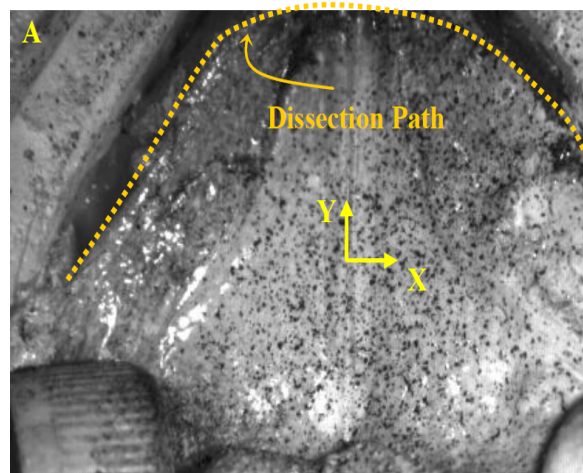
folds, a circumferential cut was made to dissect them from the thyroid cartilage. This was done to remove the strain caused by the natural geometry of the vocal folds in the laryngeal cartilage framework. The cutting path and the dissected tissue are shown in figure 6–7(a). No weights were used and the screw bars were removed. Efforts were made to maintain the orientation of the larynx and to preserve the speckle pattern as much as possible. In some cases, the vocal folds were moved out of the focus of the cameras, hampering the DIC analysis. Vocal fold images at rest and after dissection were imported into VIC-2D to calculate the initial, at-rest strain. The dissected vocal fold image was used as the reference image in DIC to measure the initial strain. The image of the vocal fold at rest was used as the reference image to measure strain during phonation.

Performing the DIC analyses was done with the direct collaboration of Justin C.W. Yang,¹ and Amir K. Miri². Jonathan Young³, as a former member of Prof. Mongeau’s research group, started the excised larynx experiment and the techniques for dissection and suturing of the larynges were demonstrated by him.

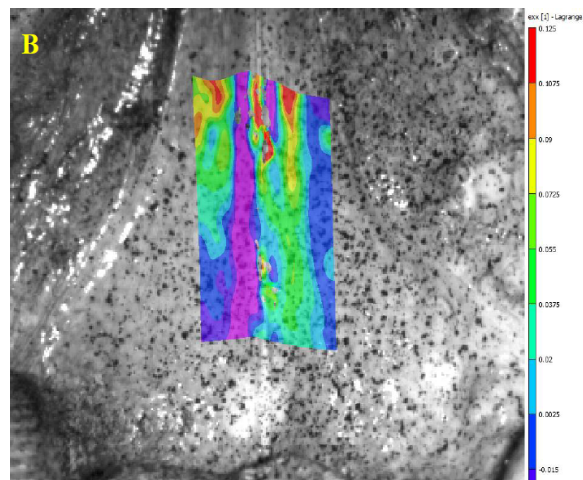
¹ Undergraduate student at Mechanical Engineering Department, McGill University. He was working under the supervision of the author of the present dissertation on the Summer Undergraduate Research in Engineering (SURE) project

² Phd, Mechanical Engineering Department at McGill University

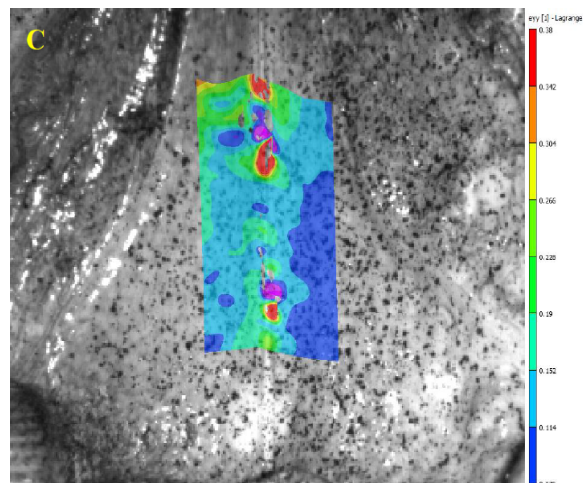
³ Associate Professor, Faculty of Medicine, McGill University, Department of Otolaryngology-Head and Neck Surgery



(a)



(b)



(c)

Figure 6–7: (a) Larynx before after cut showing dissection path, (b)-(c) The larynx before cut

6.3 Results and Discussion

6.3.1 Initial strain field on the vocal folds

The initial strain deformation of the vocal fold surface was evaluated. Because of inhomogeneity through the thickness of the vocal fold tissue, from the epithelium to the muscle, the strains mostly indicate the deformation of the lamina propria (Miri et al., 2012b). Ten larynges were subjected to the initial prephonatory strain protocol. Only one sample yielded an acceptable correlation range for 3D DIC. The other samples moved out of camera focus or their speckle patterns changed dramatically, causing a low-image correlation. Four samples supplied proper images for planar (i.e., 2D) DIC.

A typical area of interest in VIC-2D is shown on the superior surface of the vocal folds in figure 6–7. The distributions of the initial strain in the medial-lateral direction, ϵ_{0xx} , and anterior-posterior direction, ϵ_{0yy} , on the vocal fold surface before being cut from the thyroid cartilage are shown in figure 6–7(b) and 6–7(c), respectively. The measured strain values were relatively larger in the center of the imaged area. The initial strain values, ϵ_{0xx} , ϵ_{0yy} and ϵ_{0xy} in the central region of the vocal fold for four samples are shown in table 6–1.

Sample Num	Length (mm)	Mean ϵ_{xx} (%)	Mean ϵ_{yy} (%)	Mean ϵ_{xy} (%)
1	18.8	3.59±2.18	16.15±2.96	1.57±7.59
2	19.2	7.15±7.68	16.06±4.99	5.59±7.39
3	20.1	10.11±7.44	29.25±4.49	12.27±8.77
4	20.7	7.05±8.59	21.58±9.43	17.72±4.23

Table 6–1: Pre-strain in the vocal fold

As expected, the initial strain along the anterior-posterior direction, ϵ_{0yy} , had the largest magnitude among them. The normal strains along the x direction are positive, showing a tensile initial strain in the vocal folds. Discrepancies between the initial strain magnitudes for different samples in table 6–1 may be due to the inevitable differences in suturing, larynx size and weight used to obtain the sustained oscillation. However, the calculated initial strains are consistent with visual observations. After the cut, the tissue shrank posteriorly with a large deformation and both vocal folds moved toward the midsagittal plane, showing a tensile initial strain in both anterior-posterior and medial-lateral directions.

6.3.2 Kinematics of vocal fold vibration

The kinematics of the self-oscillations during the opening and closing phases of the glottal cycle were investigated. The flow rate, the static pressure and the frequency of vibration were $Q = 236\text{cm}^3/\text{s}$, $P = 690\text{Pa}$ and $f = 245\text{Hz}$, respectively. Comparisons were made with previous results obtained using a synthetic replica (Spencer et al., 2008).

Figure 6–6 shows the inspection lines along both anterior-posterior and medial-lateral directions on the two-dimensional (2D) contour plot. Displacement amplitudes of the vocal fold physical points in the z direction, W , and in the x direction, U , along the inspection lines were recorded during the oscillations. Figures 6–8(a) and 6–8(b) show that the maximum amplitude of W and U along the anterior-posterior inspection line occurs close to $y = 2\text{mm}$. Figure 6–8(c) shows that the maximum amplitude of W along medial-lateral inspection line occurs close to

$x = 0.8\text{mm}$. This point with maximum displacement amplitude in both x and z directions, ($x = 0.8\text{mm}, y = 2\text{mm}$), is called “midpoint” hereinafter.

The history of vocal fold displacement for ten cycles of the tissue vibration at the midpoint, along three spatial directions is shown in figure 6–9(a). The medial-lateral displacement amplitude, U , was the largest followed by W . The anterior-posterior displacement amplitude, V , has the lowest magnitude, as expected.

A phase difference observed between displacement components U and W is shown by the two arrows in figure 6–9(a), which are pointing at the U and W maximum amplitude points. Because of the phase difference between U and W , the tissue material points undergo an elliptical motion with time. To better illustrate this elliptical motion, the vocal fold midpoint trajectory in the frontal plane (x - z plane) and the curve fitting ellipse function are shown in figure 6–9(b). The elliptical trajectory of vocal fold material points has been reported in the literature (Boesennecker et al., 2007; Berry et al., 2001). In contrast, there was no phase difference between the displacement components in the medial-lateral direction and the one in the inferior-superior direction in the synthetic model (Spencer et al., 2008) and the physical points reach their maximum and minimum amplitudes in the medial-lateral and inferior-superior direction simultaneously.

The in-plane medial-lateral relative strain at the instant of maximum opening and closure were shown in figure 6–10. The initial strain values are neglected in this figure and only the effect of oscillation on the strain field of the superior surface of the vocal folds is considered. During closure, tensile strain is dominant and for the fully open state, the vocal folds were under compression strain. During closure, the

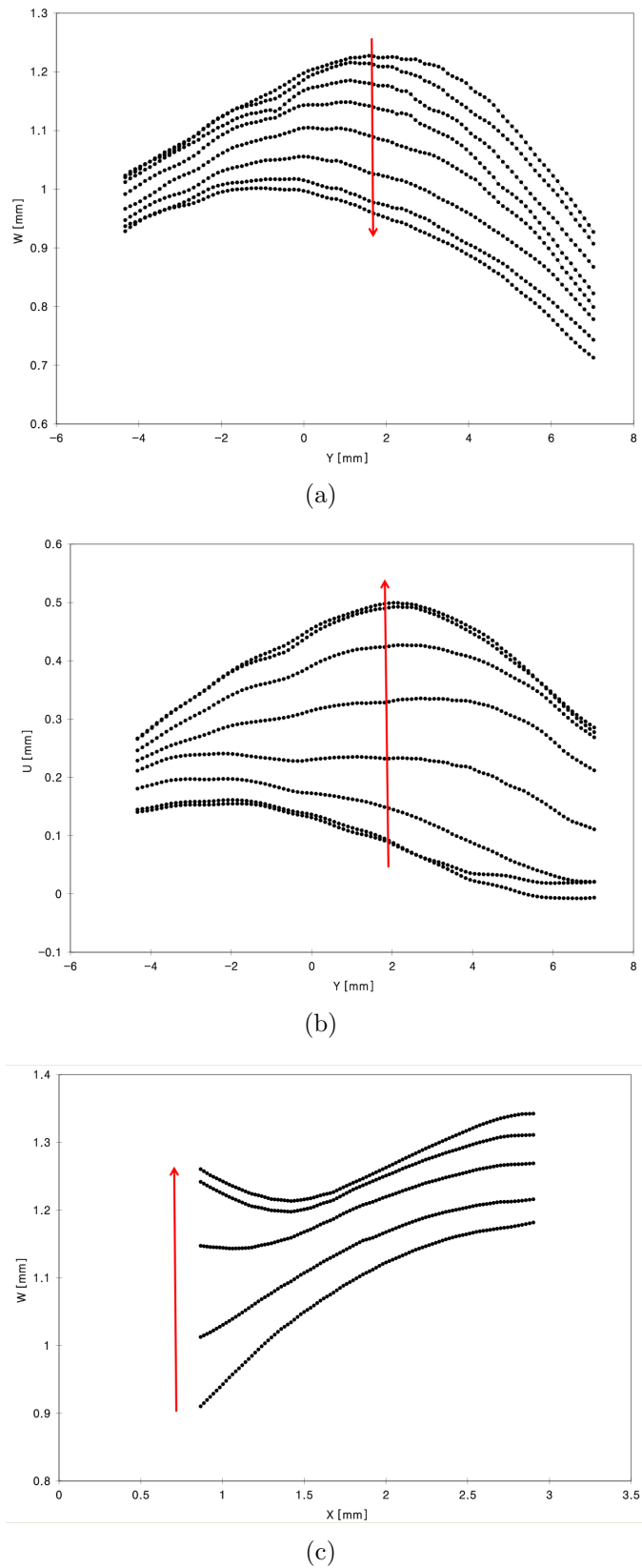


Figure 6-8: (a) Variations of W along the anterior-posterior during closing and (b) Variations of U along the anterior-posterior during opening (c) Variation of W along the medial-lateral inspection line during opening phase of oscillation

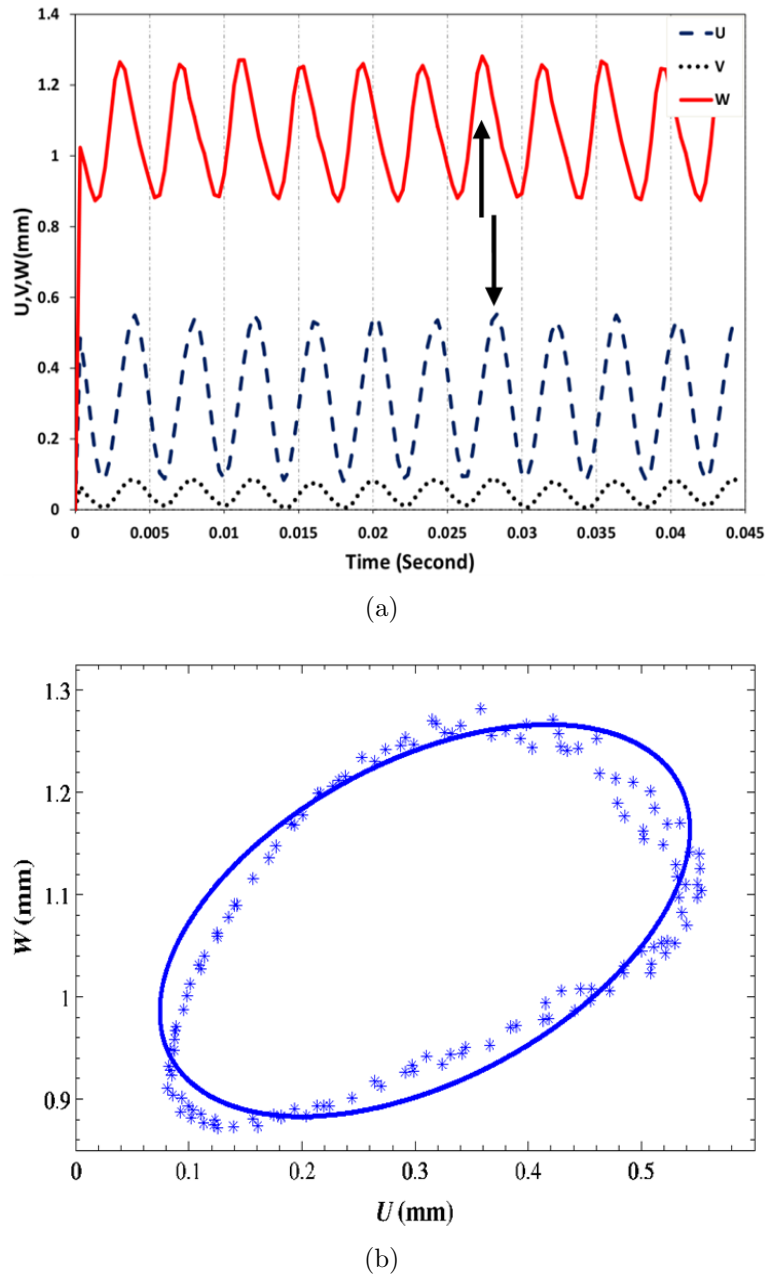


Figure 6-9: (a) Time history of displacement of the vocal fold midpoint, (b) Elliptical trajectory of midpoint

ϵ_{xx} strain is almost uniform along the edge, along the anterior-posterior direction. In the open state, the strain reaches a maximum value near the mid anterior-posterior points due to their high displacement amplitude in the x direction as shown in figure 6–8(c).

The time history of the effective strain distribution at the midpoint along the medial-lateral direction, ϵ_{xx} and along the anterior-posterior direction, ϵ_{yy} are shown in figure 6–11. It can be seen that ϵ_{xx} , is alternately in compression and in tension and the oscillation amplitude is much larger than that of ϵ_{yy} . Although the motion is periodic, slight changes in the maximum and minimum amplitudes of ϵ_{xx} can be seen from cycle to cycle. The anterior-posterior strain, ϵ_{yy} , was tensile during the entire vibration cycle, with a low oscillation amplitude. The initial strain in the anterior-posterior direction, ϵ_{0xy} has a large positive magnitude and superposition of that on the anterior-posterior strain from DIC resulted in the tensile ϵ_{yy} , during the whole vibration cycle as shown in table 6–1.

Normal strains values at the vocal fold midpoint in the anterior-posterior direction versus flow rate at the time of maximum opening and closure are shown in figure 6–12(a). As seen before, ϵ_{xx} is compressive in the maximum opening and tensile during the close state of vocal fold. For all flow rates presented in this figure, the absolute magnitude of the ϵ_{xx} for maximum opening is larger than that of closing. Vocal folds are close to the centerline in the reference image as shown in figure 6–6, as a result less deformation is expected during complete closure than maximum opening. This behavior of the vocal fold is consistent with that of the synthetic model of (Spencer et al., 2008). Figure 6–12(b) shows values of the anterior-posterior strain

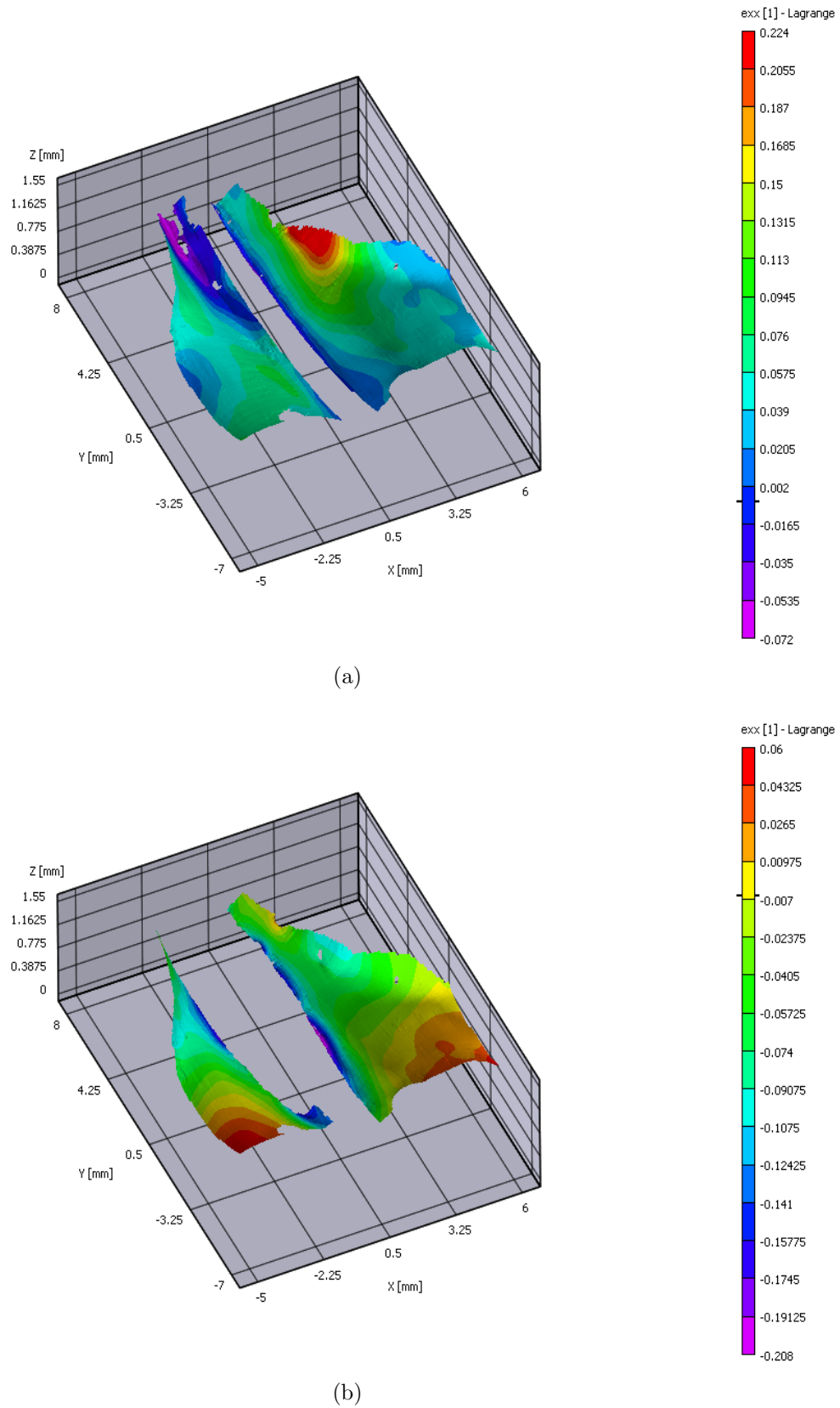


Figure 6–10: Contours of normal strain on deformed superior surface of vocal fold for (a) Open state and (b) Close state of vocal folds

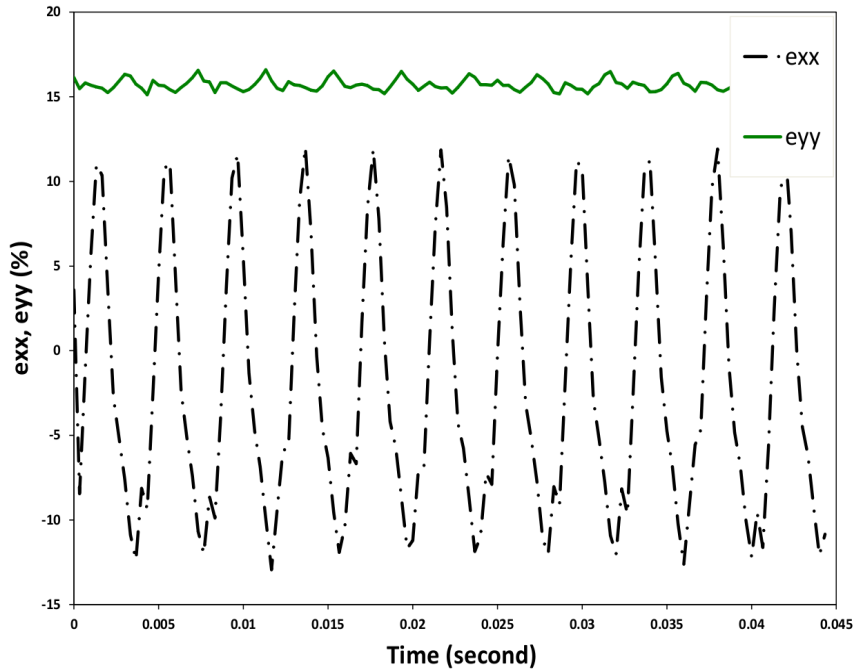
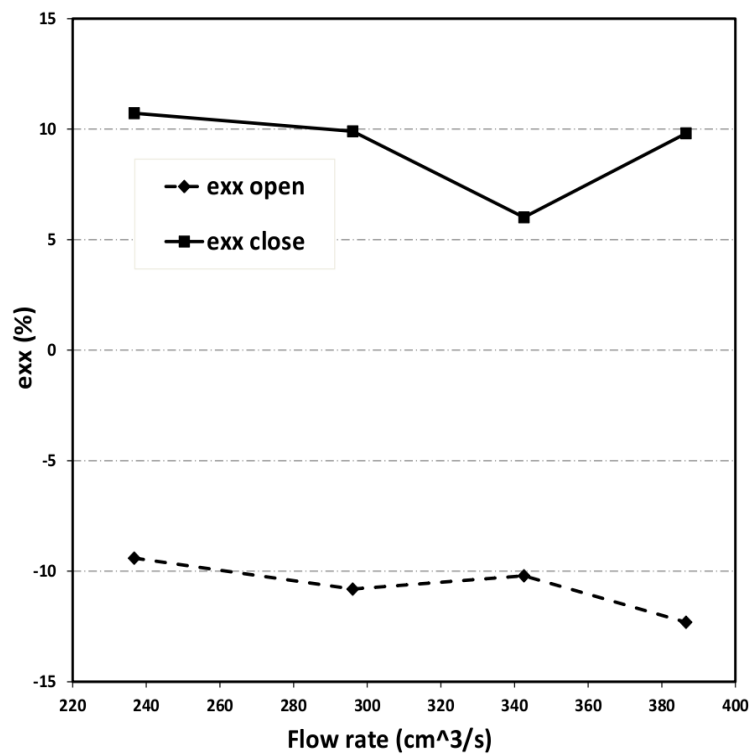


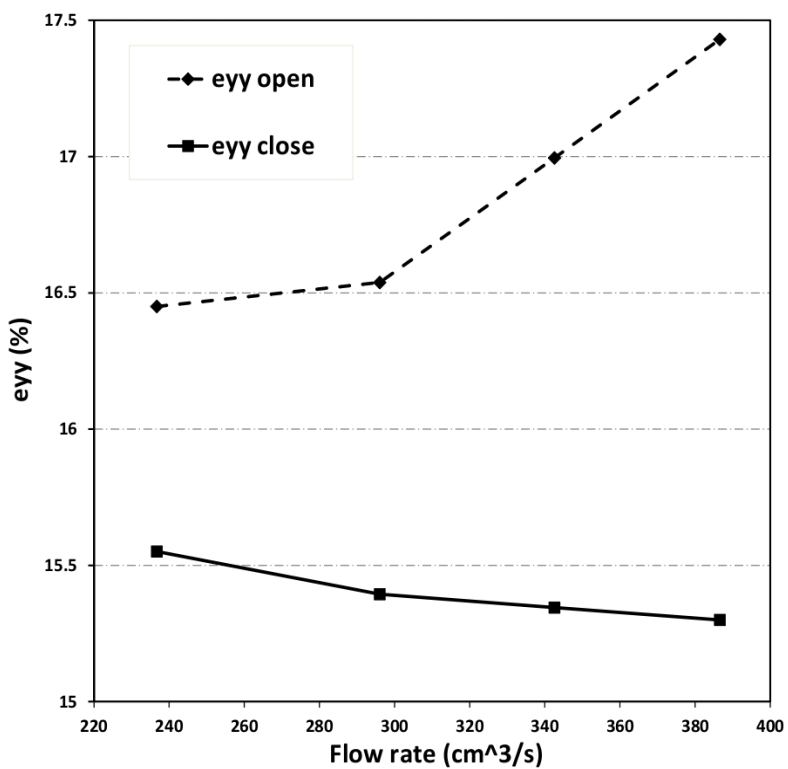
Figure 6–11: Strain-time history

ϵ_{yy} at the mid anterior posterior point versus flow rate. The values of ϵ_{yy} for close state decrease as flow rate increases and for maximum opening, the values of ϵ_{yy} increase with flow rate. The increase rate of ϵ_{yy} for maximum opening is higher than the decrease rate for close state.

To correlate strain and displacement, U , W , ϵ_{xx} and ϵ_{yy} are shown over four cycles in figure 6–13. To emphasize the phase differences, each variable was normalized by dividing its amplitude by its maximal value. The vocal folds midpoint was under maximum tensile strain in the medial-lateral direction when it was at the minimum displacement point in the inferior-superior direction. Maximum compression strain occurred when the midpoint was moving in the inferior and lateral directions at



(a)



(b)

Figure 6–12: Normal strain vs flow rate at vocal fold midpoint (a) ϵ_{xx} (b) ϵ_{yy}

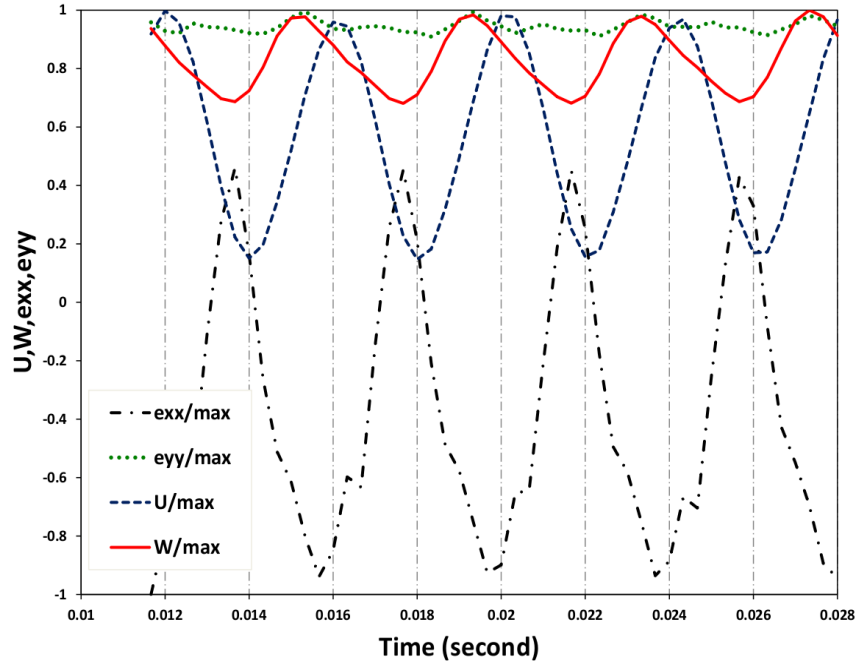


Figure 6–13: U , W , ϵ_{xx} , and ϵ_{yy} , over four cycles

the same time. At this moment in the experiment, the midpoint has reached its maximum neither in Z nor in X direction.

The vocal fold midpoint has the maximum tensile strain in the anterior-posterior direction (i.e., ϵ_{yy} maximum) when it has the maximum displacement in the inferior-superior direction (i.e., W maximum). The maximum compression strain in the anterior-posterior direction, i.e ϵ_{yy} minimum, happened when the midpoint passed the minimum displacement point in the medial-lateral direction minimum and was moving in the lateral and superior direction.

6.3.3 Impact stress assessment using an isotropic constitutive law

The principal objective of the present study is to introduce DIC as a precise and noninvasive method for determining vocal fold impact stresses. The importance

of initial strain was investigated using an isotropic hyperelastic constitutive law. Although porcine vocal fold tissue exhibits strong anisotropy (Miri et al., 2012a), the well-known eight-chain constitutive model for the sake of simplicity was selected (Miri et al., 2012b). Associated model parameters were obtained from in-vitro uni-axial traction testing of ten porcine vocal folds (Miri et al., 2012b). Application of the model to the strain field of Sample 1, with or without adding the initial strain values of table 6–1, yields the stress component in the X and Y directions, as shown in figure 6–14. The distribution of normal stress along the Y direction, based on only dynamic strains (figure 6–14A), shows a more uniform pattern than the case with initial strains (figure 6–14B) at the closing position. The former has a maximum of $\sim 1.5\text{kPa}$ while the latter reaches 15 kPa at some locations. This was expected from the initial strain value (table 6–1) and the hyperelasticity of vocal fold tissue (Miri et al., 2012b). For the open position of the vocal folds, the stress along the longitudinal direction is tensile and varies between 1 kPa and 15 kPa.

The stress component along the X direction spanned a symmetric range, from -4 kPa to 4 kPa, when initial strain values were included (figure 6–14D) while the case of dynamic strains (figure 6–14C) spans negative values. This stress component represents an accurate estimation of the impact stress because it measures tissue forces along the direction of collision. The compression body stress of 4 kPa magnitude for the subglottal pressure of $P=690$ Pa, may be considered very close to the impact stress because of the force equilibrium at the contact point. The calculated stress has the same order of magnitude of the impact stresses from other studies. In a study by (Jiang & Titze, 1994), for instance, the stress between the vocal fold of

the canine hemilarynx and the vertical plate was found to be in the range of 0.5 to 5 kPa. (Verdolini et al., 1998) have reported values in the range of 0.3 to 5.3 kPa for impact stress of canine larynx. Considering the subglottal pressure and the corresponding impact stress range, higher stresses are obtained in the present study. For instance, for a subglottal pressure range of 0.9 to 1.5 kPa, contact pressure ranged from 0.8 to 1.5 kPa in (Jiang et al., 2001) study. The impact stresses reported in the literature are mostly for canine larynges.

Comparing the cases of closing (figure 6–14D) and opening (figure 6–14E) stresses revealed a significant difference in the normal stress along the transverse direction. During opening, the tissue experiences a compression stress of 15 kPa close to the vocal fold edge. This can be due to aerodynamic stresses (i.e., the aerodynamic pressure in the airflow). Stress distributions were calculated using an isotropic model; however, the porcine vocal fold tissue exhibits a strong anisotropy (Miri et al., 2012a), calling for further analysis.

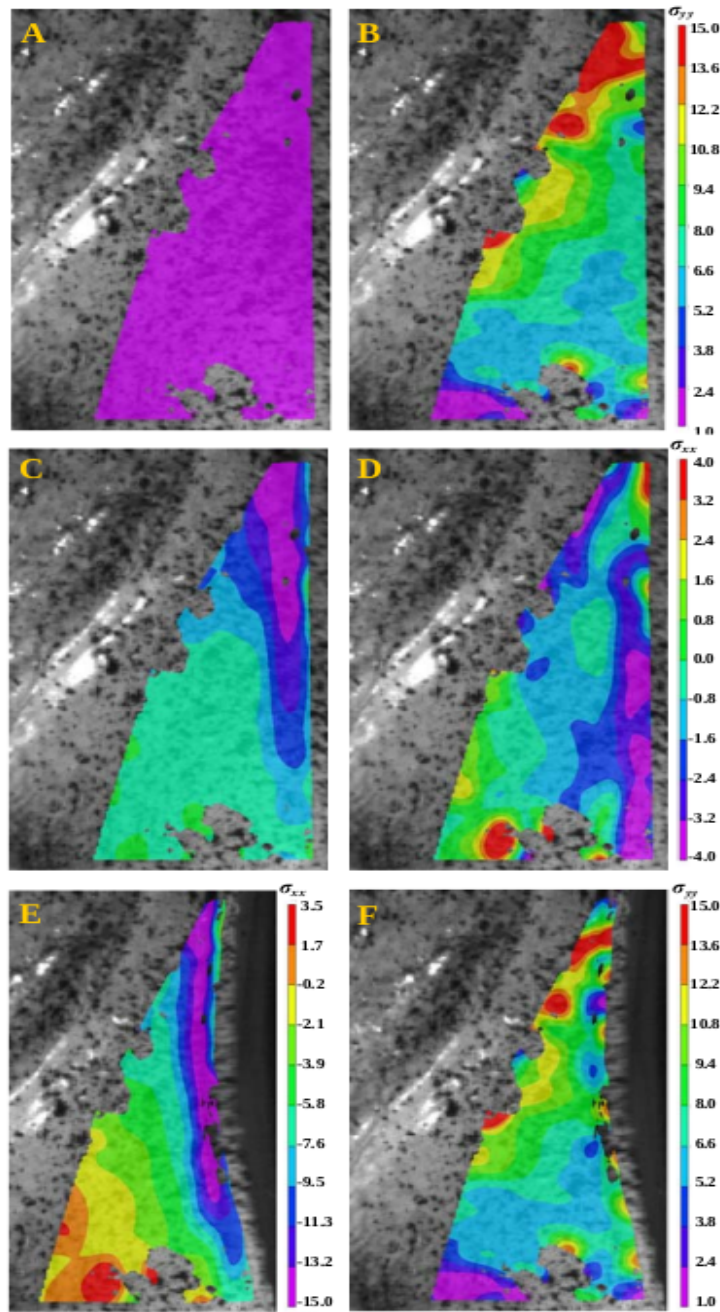


Figure 6-14: A-B) Distribution of the normal stress σ_{xx} on deformed surface of vocal fold at closing position based on dynamic strains and dynamic strain with pre-strain, respectively; C-D) Distribution of the normal stress σ_{xx} on deformed surface of vocal fold at closing position based on dynamic strains and dynamic strain with pre-strain, respectively. E) Distribution of the normal stress σ_{xx} on deformed surface of vocal fold at opening position. F) Distribution of the normal stress σ_{yy} on deformed surface of vocal fold at opening position

CHAPTER 7

Concluding remarks and future work

7.1 Concluding remarks

7.1.1 Three-dimensional reconstruction of human vocal folds and laryngeal cartilages using CT scan data

Eight sets of laryngeal cartilages were successfully segmented from CT scan images to recreate subject-specific models of the laryngeal cartilages, vocal folds and vocal tracts. The morphometric measurements from the reconstructed laryngeal cartilages were compared to those from excised larynges, and deemed to be accurate within a relatively small percent error. Healthy and post-surgery geometries of the vocal folds and vocal tract during phonation and respiration were also reconstructed from CT images.

In order to enhance the repeatability and comparability between research groups and to facilitate the access to the 3D models, general models of the laryngeal cartilages were proposed. General cartilage models designed using the landmark points and dimensions from the reconstructed geometries. Furthermore, biomechanically important morphometric features were preserved in these models, therefore they can be used for further simulations. Subject-specific solid models for vocal folds and vocal tract were still preferred due to the fact that the geometry of the vocal folds constantly changes and the segmentation of CT images for these geometries is much easier than that for the cartilages.

7.1.2 Three-dimensional reconstruction of human vocal folds by mapping HSDI data and MRI images

An image processing method was proposed to create the geometries of the vocal folds at desired glottal angles during one complete oscillation cycle. Vocal fold edges were detected using a threshold-based method. The displacements of the edges were curve-fitted with sinusoidal time functions. Mucosal wave propagation speed was also calculated by following the mucosal wave peak on the vocal fold surface. Mucosal wave speed and wave propagation methods were used to calculate the motion functions of the vocal folds lower layers. Only the superior surface of the vocal folds is visible in HSDI data, and lower layers of the vocal folds in the inferior direction are visible in transverse MRI images. Therefore, HSDI data with high temporal resolution was overlapped with transverse MRI images of the vocal folds, and new sets of MRI images were produced for the desired glottal angles. Solid 3D models created from modified MRI images can be used to assess the applicability of the quasi-steady approximation in 3D glottal airflow simulation. Due to the complexity of the FSI simulations, using accurate 3D geometries of the larynx and vocal folds with different glottal angles along with quasi-steady approximation may be considered as an alternative for 3D glottal airflow simulation.

7.1.3 Assessment of the quasi-steady approximation in glottal airflow

A series of dynamic and static finite element simulations of airflow within the glottis was performed using the COMSOL multiphysics[®] software to investigate the validity of the quasi-steady approximation. The velocity field, airflow rate, pressure and shear stress on the vocal fold wall, and orifice discharge coefficients obtained in the dynamic and static simulations were compared. Fourteen virtual probes were

located on the vocal fold tip to quantify the differences between the dynamic and static simulation results.

A qualitative comparison of the velocity streamlines in the glottis shows a similarity between those in the steady and dynamic simulations. In both cases, asymmetry among the streamlines was observed downstream of the vocal folds. Comparisons among the flow rates, shear stress, pressure on the vocal fold wall and orifice discharge coefficients show relatively small differences between the steady-state and the dynamic simulations. Comparison between the time dependent and convective accelerations of the minimum constriction point on the centerline at convergent and divergent shapes of the vocal folds shows that the convective acceleration is dominant during the open phase of the glottal duty cycle. The overall contribution of unsteady effects to the radiated sound are thus negligibly small when there is no net displacement flow from large nearfield volume fluctuations. However, the time-dependent acceleration is not negligible near the onset and closure instances; as a result, quasi-steady approximation is not strictly valid at these times.

The present simulation method has some limitations that may be improved in future work. Comparison of the current results with previous simulations is qualitatively validating; however, because of the lack of empirical data, quantitative validation of the computational simulation was impossible. Only the normal oscillation frequency for a healthy male subject (i.e., 100 Hz) was considered. The average frequency of phonation for normal woman larynx is 200-250 Hz. Higher oscillation frequencies will accentuate the role of the unsteady variables. Preventing vocal folds closure resulted in a reduced contribution of the unsteady terms, which dominate

during the opening and closing phases of the glottal cycle and decreases the difference between steady-state and dynamic simulations.

Despite all their limitations and simplification, 2D models can be useful for understanding the acoustics and aerodynamic phenomena during vocal fold vibration. Investigation of the quasi-steady approximation in fully three-dimensional models will be the objective of future work.

7.1.4 Numerical simulation of the airflow in subject-specific airway models

Realistic geometries play an important role in reproducing the physics of phonation in computational and experimental studies. As shown in Chapter 5, the differences between the healthy and postsurgical geometries directly affect the jet flow features in the larynx. Elements such as secondary flow in the transverse plane, pressure gradient in the anterior-posterior direction, realistic jet flow asymmetry and the jet axis switching phenomenon cannot be captured in 2D models; therefore, 3D geometries should be used. Although the simulations presented in Chapter 5 used the static solid models of the larynx and the vocal folds, many of the 3D characteristics of the flow field which were reported in the FSI simulations and excised larynx experiments, were observed, highlighting the importance of using realistic geometries and showing that 3D quasi-steady approximation may be used to scrutinize certain elements in voice production simulations.

7.1.5 Determination of strain field on excised porcine larynges using DIC

The DIC method was used to calculate the deformation field on the vocal fold surface of porcine larynges during self-sustained oscillation. To calculate the effective strain and stress values, the initial strain field in the vocal folds was calculated.

The initial strain originated from the physiology of the laryngeal framework and the amount of exerted force required to make the vocal folds phonate on the excised larynx setup. Empirical findings for the stress and strain field of the vocal folds during vibration can be used as the input for computer simulations. The applicability of this method in studies of excised larynges paves the way for obtaining the deformation field in future studies using human subjects. This may eventually lead to strategies to reduce stress within the larynx, thus diminishing the incidence of and helping in the nonsurgical therapy of nodules, polyps and cysts. This technology may also contribute to the identification of early lesions, which are difficult to detect clinically.

Although the accuracy of the DIC method was verified by comparing results with Laser Doppler Velocimetry (LDV) (Spencer et al., 2008), a few limitations persist when using it to determine vocal fold deformation fields. Providing a speckle pattern that can remain unchanged on the surface of the vocal folds during oscillation is challenging and time consuming. Even for the optimum combination of background and chemical dye or powder, several trials were needed to obtain the acceptable pattern. Using the backgrounds on the surface of the folds dehydrates the tissue, which may affect its mechanical properties. As a result, the speckle pattern and the background were frequently cleaned off during the experiment to hydrate the superior surface of the folds and a new pattern was then created. For future *in vivo* applications of this method, the speckle pattern must also be nontoxic.

Although using high-speed cameras provides a high temporal resolution of the displacement and deformation of physical points, they have a low range of focus. Slight changes in the location of the larynx or high-amplitude vibration of the vocal

folds can displace them from camera focus and make the images blurry. Suturing the posterior part of the larynx may cause an asymmetry in vocal fold postures, which can cause differences between the strain read out for the left and right fold. Suturing is performed to prevent air leakage from the posterior part of the larynx and to guide the air to the glottis. However, the initial strains applied on the vocal folds by suturing could be different from one larynx to another.

Significant differences were observed between the results of this study using porcine vocal folds and those of one using a rubber vocal fold model (Spencer et al., 2008). The phase difference between the displacements in the inferior-superior and medial-lateral directions was only observed for porcine vocal folds. That may be due to differences in the mechanical properties and geometry of vocal fold tissue and the rubber model. In contrast to the findings of the present study, no mucosal wave was reported for the rubber model (Spencer et al., 2008). The variation of the ϵ_{xx} and ϵ_{yy} versus flow rate differs between the rubber model and porcine vocal folds. Because of large values of initial strain in the anterior-posterior direction, vocal folds are under tensile strain during the fully closed and fully open states; however, according to Figure 5 in Spencer et al. (2008), the rubber model experienced compression in the closed state.

7.2 Contributions to the voice research

The overall objective of this dissertation was to create computer models and perform experiments that can be used to create subject-specific models of the larynx and vocal folds. The image reconstruction method explained in Chapter 2, provides subject-specific geometries that can be used for computational simulations.

Generic computer models of the laryngeal cartilages (thyroid, cricoid and arytenoid) were created and appear to be the first of their kind. All biomechanically important dimensions are preserved in these models. General laryngeal cartilages are subject-independent and accessible to all researchers; as a result, they make simulations repeatable and comparable between different research groups.

Chapter 5 also shows that realistic 3D models capture many of the fluid features of glottal airflow that have been previously reported in the experimental analyses. This, paired with the major challenges in the creation of a realistic FSI simulation, may lead to consideration of the quasi-steady approximation as an alternative. The image processing method proposed in Chapter 3 provides accurate 3D models of the larynx and vocal folds at different glottal angles which may be used for the assessment of the quasi-steady approximation in 3D glottal airflow simulations. As an introductory step, the quasi-steady approximation in simulating glottal airflow was evaluated in a 2D driven model in Chapter 4. The effect of vocal fold volume fluctuation on unsteady terms was investigated by keeping the area of the vocal folds constant at all glottal angles.

The final contribution of the present dissertation is the calculation of the strain field of the superior surface of the vocal fold using DIC. Excised porcine larynges were used to investigate the kinematics of the vocal fold motion, and the differences with synthetic rubber model were explained. The initial strain on the vocal folds tissue was calculated based on a novel dissection protocol. The initial strain was added to the measured stain obtained from DIC to calculate the effective strain during oscillation.

7.3 Recommendations for future work

7.3.1 Assessment of the quasi-steady approximation in 3D-accurate models

Assessment of the quasi-steady approximation for a 2D driven vocal fold model is presented in Chapter 4. Assessment of this approximation in 3D-accurate geometries will be among future studies. Subjects will perform the same phonation tasks during three sets of experiments MRI, HSDI and Rothenberg mask. The circumferentially vented (CV) pneumotachograph mask is mostly used for aerodynamic assessment of vocal function (Rothenberg, 1973). The oral volume velocity and the intraoral pressure will be captured. Accurate 3D geometries with various glottal angles will be used and glottal airflow simulations will be performed for each geometry, as in the Chapter 5 simulations. Using the Rothenberg mask, the pressure and airflow at the level of mouth can be obtained. Inverse filtering methods can be used to calculate the glottal flow rate. To validate the 3D simulations, the glottal fluid flow will be compared to the experimental results from a Rothenberg mask. This comparison will enable us to assess the validity of quasi-steady approximation in 3D simulation.

7.3.2 *In vivo* digital image correlation analyses

The applicability of the DIC method for calculation of the vocal folds surface strains in excised porcine larynges is shown in the Chapter 6. Direct application of DIC for *in vivo* measurement is challenging. In order to create a speckle pattern on the human vocal folds for *in vivo* experiments, the dye has to be non-toxic, biocompatible and water insoluble. Furthermore, to perform DIC analysis, the design of new endoscopic probes for imaging with two separate cameras from two different angles is needed. Another challenge of *in vivo* DIC analysis is to reduce the glare

created by the reflection of the light source. As stated in Chapter 6, this problem was solved by using a layer of cosmetic foundation on the vocal folds and using the graphite powder instead of the dye. Apparently, this method and the same material cannot be used for *in vivo* measurements. *In vivo* measurements provide the accurate strain field of the superior surface of the human vocal folds. These results can be used as the benchmark for validation of computational simulations.

7.3.3 Building subject-specific models of the larynx and vocal folds

Although person-specific geometries of the vocal folds and larynges with different glottal angles were produced in the present study, the lack of appropriate viscoelastic tissue properties for the vocal folds (Mittal et al., 2013) continues to hamper the creation of high-fidelity person-specific models. In a recent study Kazemirad et al. (2013), a non-invasive method was developed to determine the shear modulus of human vocal fold tissue *in vivo* via measurements of the mucosal wave propagation speed calculated in Chapter 3, during phonation. Using the obtained *in vivo* mechanical properties along with the accurate geometries of the vocal folds and larynx from the present study, may result in the development of FM subject-specific models with high potential for application in treatments.

APPENDIX A

Design details of laryngeal cartilages and engineering drawings

The thyroid cartilage was constructed in two parts: the cornua and the laminae. Each part was created on one side and mirrored across the mid-sagittal plane. The cornua were designed using ellipses sketched parallel to the coronal plane. Their major and minor diameters were averaged from the reconstructed geometries, and their positions were given according to those dimensions from Table 2–1. All measurements were referenced and adapted to the inferior-posterior edge of the thyroid notch (point 2 in figure 2–2(a)). The lamina was constructed using four sketches also parallel to the coronal plane. Sketch details can be found in figure A–1. To enhance the realism of the cartilage, particular attention was placed on ensuring correct curvature of the superior edge of the lamina, including that of the thyroid notch. However, since these cartilages are aimed at uses relating to phonation phenomena, less emphasis was given to the oblique line, where the thyrohyoid muscles attach to the thyroid. Since the hyoid bone has only a minimal role in voice production, it was not included in this model. The various parts of the thyroid were lofted together as surfaces before being converted to solid bodies.

The cricoid cartilage was the simplest of the three structures to construct, created from a single loft of four sketches and two splines. Two sketches were made on the mid-sagittal plane, and two others on the coronal plane. In particular for

this cartilage, great importance was placed on joint facet locations. The cricothyroid facets were delimited simply by the dimensions of the coronal-plane sketches, and the cricoarytenoid facets by the superior spline. The superior spline connects the top edges of all sketches and delimits points X (left and right), 8-8', and 6-6'. The inferior spline emphasizes the anterior arch, points 9-9' and 7-7'. Construction details are shown in drawing shown in figure A-2.

The arytenoid was composed of six sketches lofted together using three splines. A larger amount of sketches was necessary to ensure correct thickness and shape. As discussed in section 2.4.1, the dimensions of the reconstructed arytenoids were subject to large errors, especially those dimensions involving the vocal process. Therefore, in order to minimize the error in the generic model, measurements involving the exact location of the vocal process were taken from literature values. The arytenoids were constructed at an angle of 51.84 degrees from the mid-sagittal plane, and at a height of 25.05mm from the top plane, in order to make the final assembly easier. Drawing shown in figure A-3 and A-4 show the important characteristics of the structure.

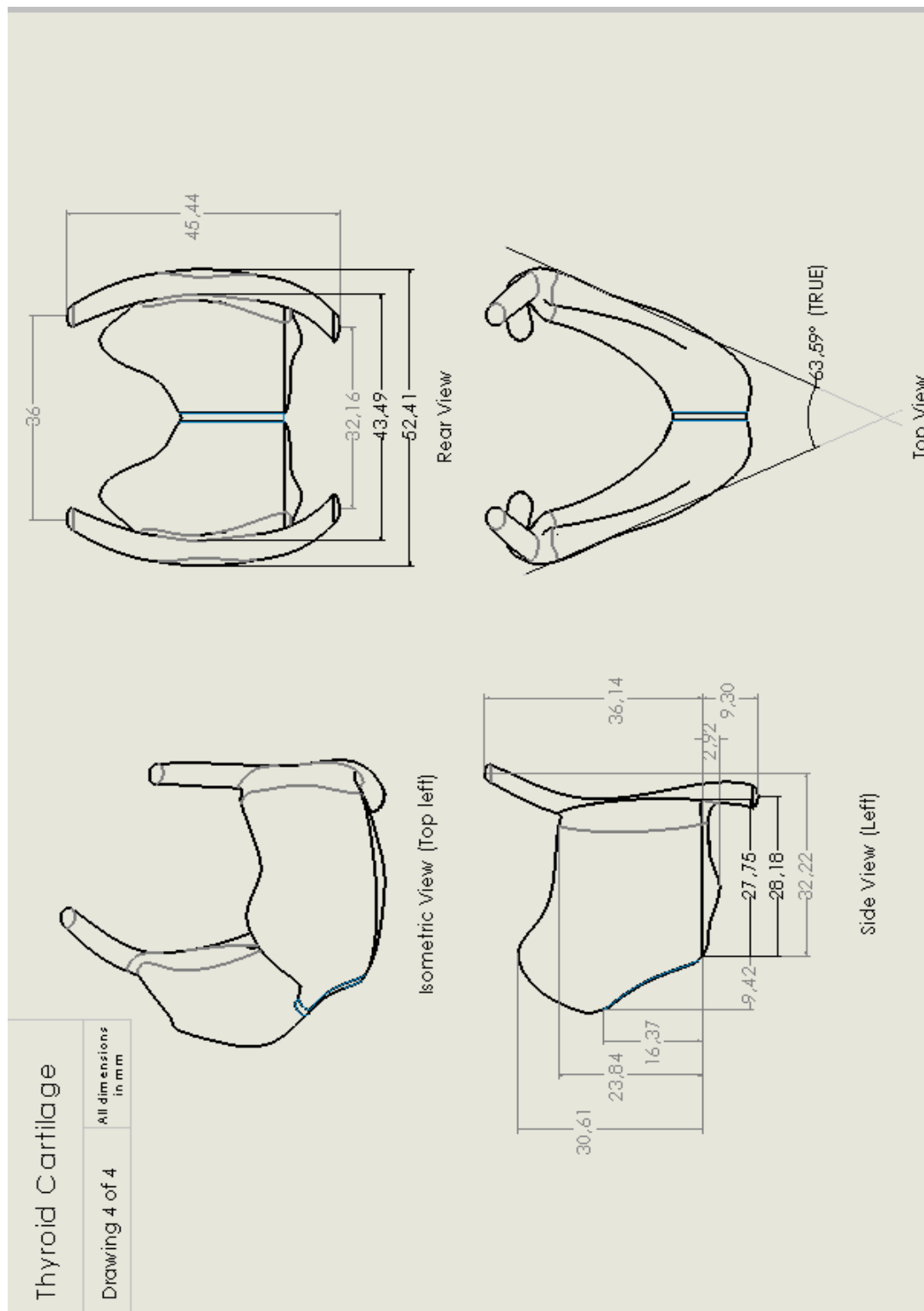


Figure A–1: Engineering drawings of standard thyroid cartilage model

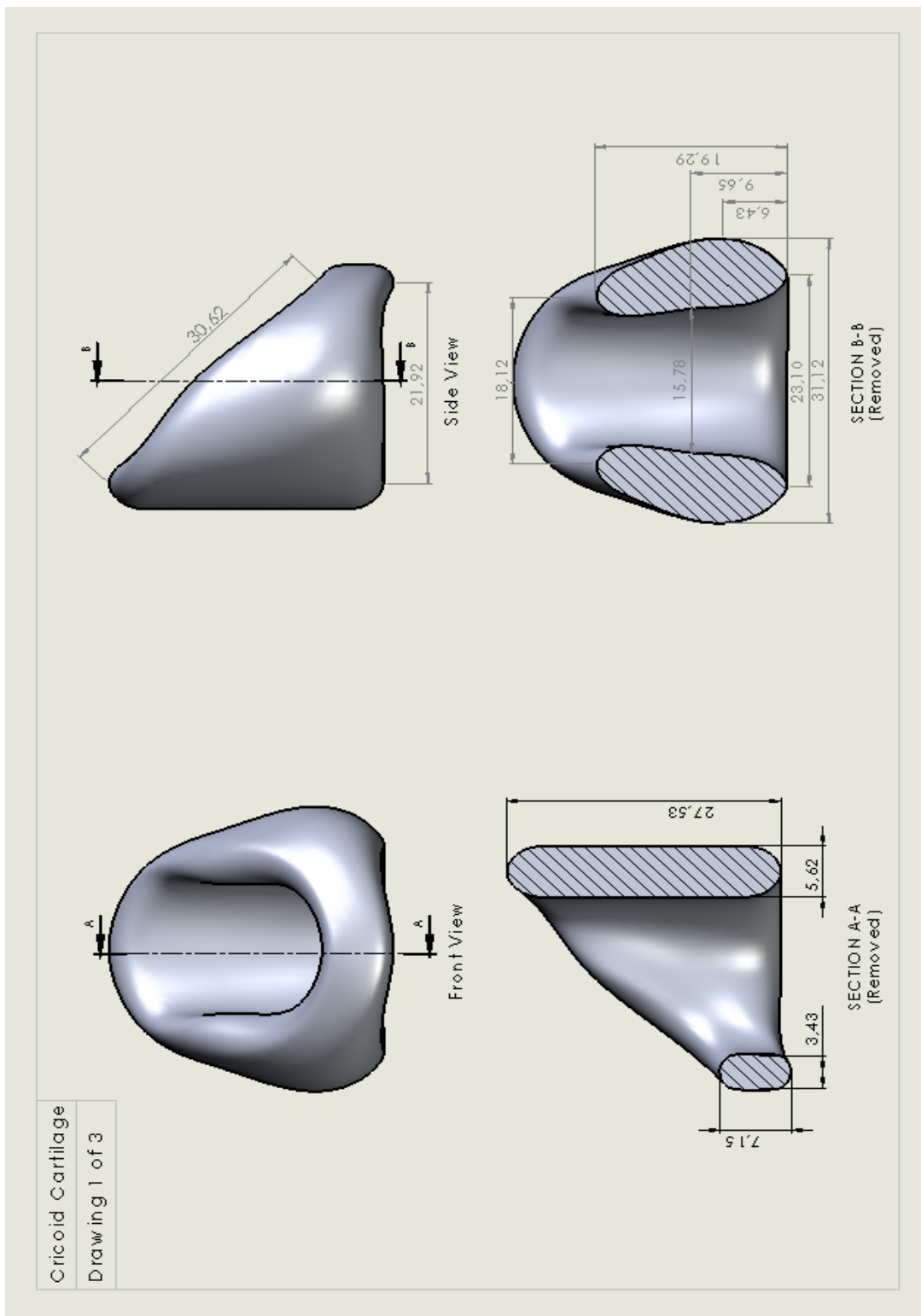


Figure A-2: Engineering drawings of standard cricoid cartilage model

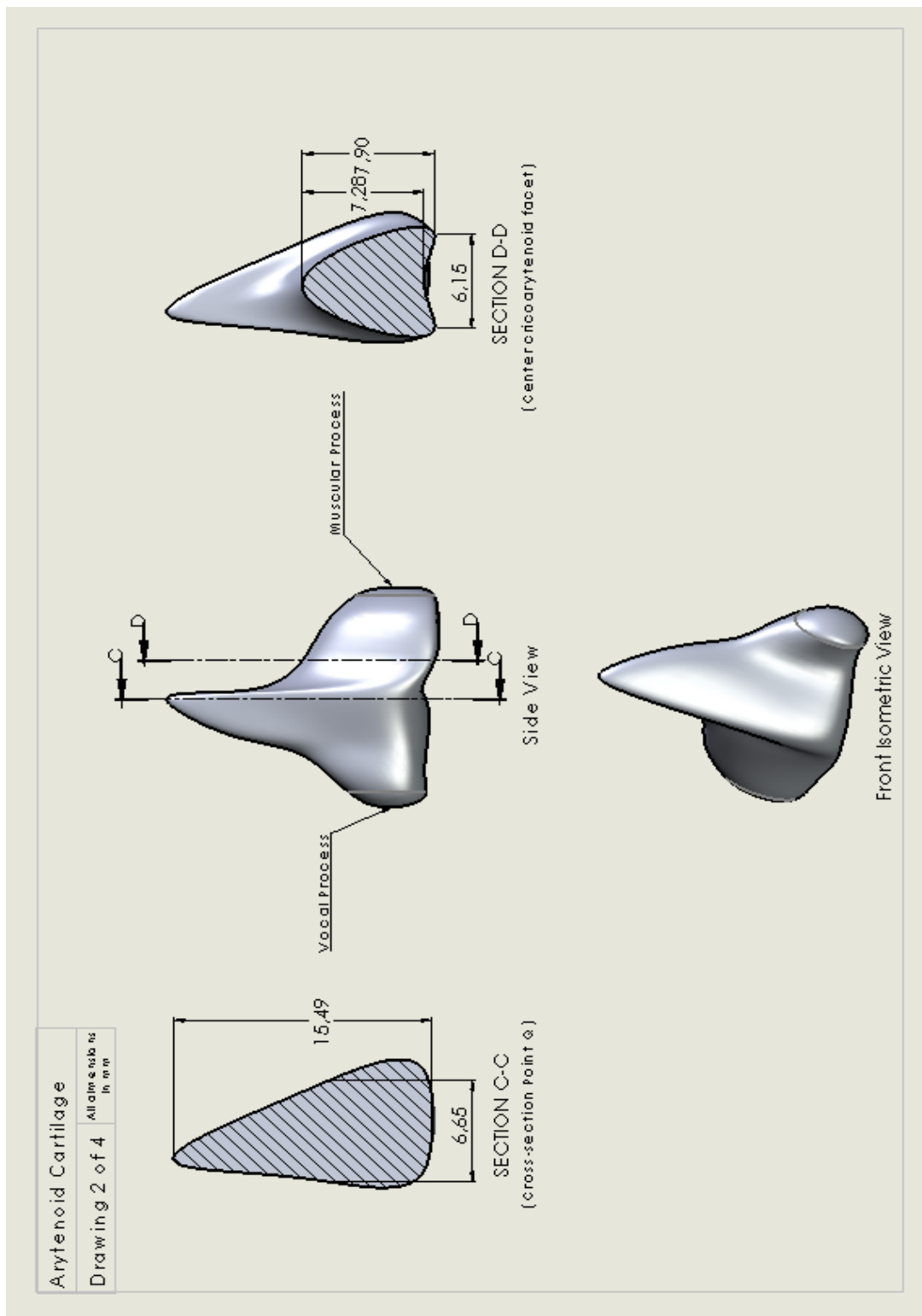


Figure A-3: Engineering drawings of standard arytenoid cartilage model

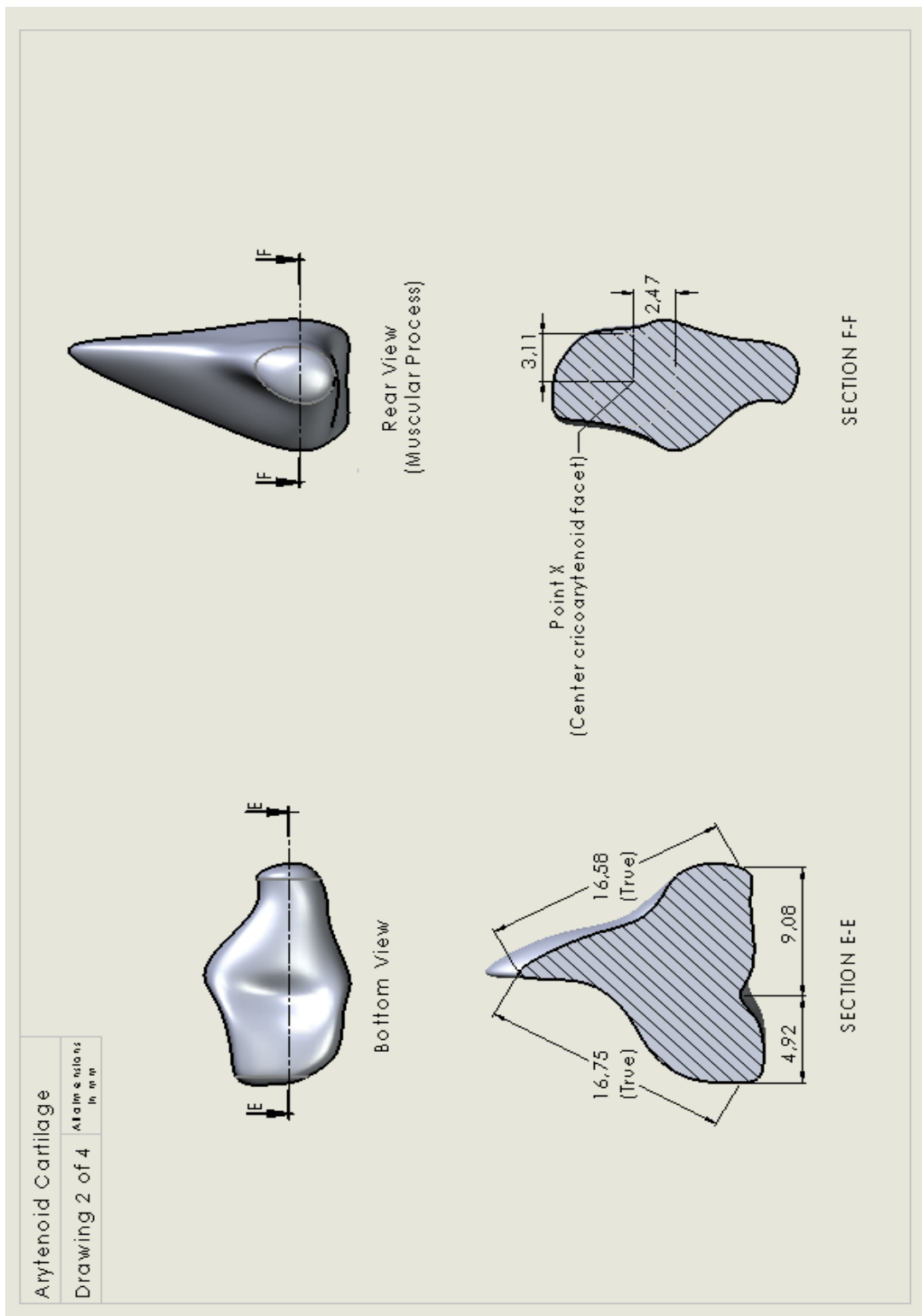


Figure A-4: Engineering drawings of standard arytenoid cartilage model

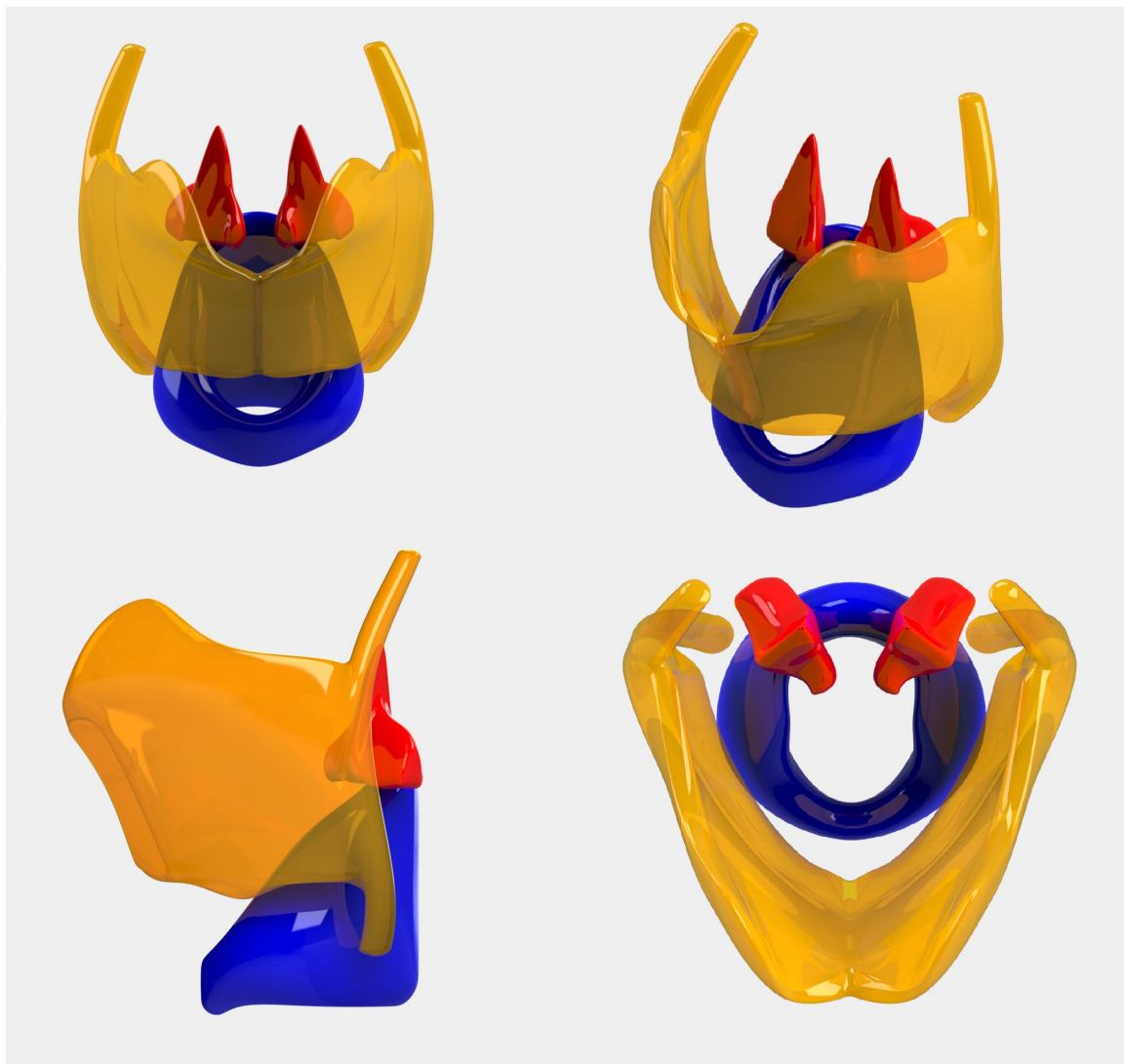


Figure A-5: Standard laryngeal cartilage framework

APPENDIX B M5 model

The cross section area of the M5 model is divided into seven parts as illustrated in figure B–1.

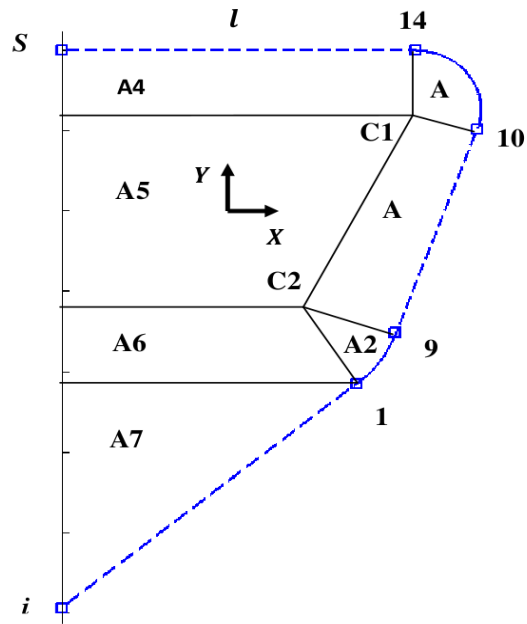


Figure B–1: Cross section area of the M5 model

Each of these areas and as a result the whole area is a function of the orifice angle, Ψ , and the vocal fold superior length in the medial lateral direction, l , i.e $A = f(l, \Psi)$.

The geometry of M5 model as well as $R_0, R_{40}, R_L, R_\Psi, B, T, Q_1, Q_2, Q_3, Q_4, Q_5$, parameters are defined in (Scherer et al., 2001). According to figure B-1:

$$x_{14} = x_s + l \quad (\text{B.1})$$

$$y_{14} = y_s \quad (\text{B.2})$$

$$x_{c1} = x_{14} \quad (\text{B.3})$$

$$y_{c1} = y_{14} - R_\Psi \quad (\text{B.4})$$

$$y_{10} = y_{14} - R_\Psi + R_\Psi \cdot \sin(\Psi/2) \quad (\text{B.5})$$

$$x_{10} = x_{14} + R_\Psi \cdot \cos(\Psi/2) \quad (\text{B.6})$$

$$y_9 = y_{14} - Q_4 - Q_3 \quad (\text{B.7})$$

$$x_9 = -(y_9 - y_{10}) \cdot \tan(\Psi/2) + x_{10} \quad (\text{B.8})$$

$$x_{c2} = x_9 - R_L \cdot \cos(\Psi/2) \quad (\text{B.9})$$

$$y_{c2} = y_{14} - T \quad (\text{B.10})$$

$$y_1 = y_{14} - T + Q_5 \quad (\text{B.11})$$

$$x_1 = \sqrt{\left| R_L^2 - (y_1 - y_{14} + T)^2 \right|} + x_9 - R_L \cdot \cos(\Psi/2) \quad (\text{B.12})$$

$$A_1 = R_\Psi^2 \cdot \left(\frac{\pi}{2} - \Psi/2 \right) / 2 \quad (\text{B.13})$$

$$A_2 = R_L^2 \cdot \left(\left(\frac{50}{180} \right) \cdot \pi + \Psi/2 \right) / 2 \quad (\text{B.14})$$

$$A_3 = (R_L + R_\Psi) \cdot Q_1 / 2 \quad (\text{B.15})$$

$$A_4 = (R_\Psi) \cdot l \quad (\text{B.16})$$

$$A_5 = \left[(x_{14} - x_s) + \left(x_9 - R_L \cdot \cos\left(\frac{\Psi}{2}\right) - x_s \right) \right] \cdot |(y_{14} - R_\Psi) - (y_{14} - T)| / 2 \quad (\text{B.17})$$

$$A_6 = |y_{c2} - y_1| \cdot [(x_{c2} - x_s) + (x_1 - x_s)] / 2 \quad (\text{B.18})$$

$$A_7 = |(y_i - y_1) \cdot (x_1 - x_s)| / 2 \quad (\text{B.19})$$

$$A = A_1 + A_2 + A_3 + A_4 + A_5 + A_6 + A_7 \quad (\text{B.20})$$

For a given Ψ , the difference between the area of the M5 model, A and the $A_0 = A(l_0 = 7mm, \Psi = -40^\circ)$. In order to keep the area constant and equal to A_0 the superior length should be updated as:

$$x_{shift} = -2.\Delta A / (|y_i - y_{14}| - |y_i - y_1|) \quad (\text{B.21})$$

$$l = l_0 + x_{shift} \quad (\text{B.22})$$

Having the updated l , the new location of points 14, 10, 9 and 1 are obtained from equations B.1to B.22.

References

- Alipour, F., Fan, C., & Scherer, R. (1996a). A numerical simulation of laryngeal flow in a forced-oscillation glottal model. *Computer Speech & Language*, 10(2), 75–93.
- Alipour, F., & Jaiswal, S. (2008). Phonatory characteristics of excised pig, sheep, and cow larynges. *The Journal of the Acoustical Society of America*, 123(6), 4572.
- Alipour, F., & Jaiswal, S. (2009). Glottal airflow resistance in excised pig, sheep, and cow larynges. *Journal of Voice*, 23(1), 40–50.
- Alipour, F., Scherer, R., & Knowles, J. (1996b). Velocity distributions in glottal models. *Journal of voice*, 10(1), 50–58.
- Alipour, F., & Scherer, R. C. (1995). Pulsatile airflow during phonation: An excised larynx model. *The Journal of the Acoustical Society of America*, 97, 1241.
- Alipour, F., & Scherer, R. C. (2004). Flow separation in a computational oscillating vocal fold model. *The Journal of the Acoustical Society of America*, 116, 1710.
- Barney, A., Shadle, C., & Davies, P. (1999). Fluid flow in a dynamic mechanical model of the vocal folds and tract. i. measurements and theory. *The Journal of the Acoustical Society of America*, 105, 444.
- Becker, S., Kniesburges, S., Müller, S., Delgado, A., Link, G., Kaltenbacher, M., & Döllinger, M. (2009). Flow-structure-acoustic interaction in a human voice model. *The Journal of the Acoustical Society of America*, 125, 1351.

- Berke, G. S., Moore, D. M., Monkewitz, P. A., Hanson, D. G., & Gerratt, B. R. (1989). A preliminary study of particle velocity during phonation in an in vivo canine model. *Journal of Voice*, 3(4), 306–313.
- Berry, D., Montequin, D., & Tayama, N. (2001). High-speed digital imaging of the medial surface of the vocal folds. *The Journal of the Acoustical Society of America*, 110, 2539.
- Bhandari, A., Izdebski, K., Huang, C., & Yan, Y. (2012). Comparative analysis of normal voice characteristics using simultaneous electroglottography and high speed digital imaging. *Biomedical Signal Processing and Control*, 7(1), 20–26.
- Bhatnagar, P., Gross, E., & Krook, M. (1954). A model for collision processes in gases. i. small amplitude processes in charged and neutral one-component systems. *Physical Review*, 94(3), 511.
- Bielamowicz, S., Berke, G. S., Kreiman, J., & Gerratt, B. R. (1999). Exit jet particle velocity in the in vivo canine laryngeal model with variable nerve stimulation. *Journal of Voice*, 13(2), 153–160.
- Boessenecker, A., Berry, D., Lohscheller, J., Eysholdt, U., & Doellinger, M. (2007). Mucosal wave properties of a human vocal fold. *Acta acustica united with acustica*, 93(5), 815–823.
- Chen, H., Chen, S., & Matthaeus, W. (1992). Recovery of the navier-stokes equations using a lattice-gas boltzmann method. *Physical Review A*, 45(8), 5339–5342.
- Chen, H., Teixeira, C., & Molvig, K. (1997). Digital physics approach to computational fluid dynamics: some basic theoretical features. *International Journal of Modern Physics C*, 8, 675–684.

- Chen, L., & Mongeau, L. (2011). Verification of two minimally invasive methods for the estimation of the contact pressure in human vocal folds during phonation. *The Journal of the Acoustical Society of America*, 130, 1618.
- Chen, S., & Doolen, G. (1998). Lattice boltzmann method for fluid flows. *Annual review of fluid mechanics*, 30(1), 329–364.
- Chen, T., Chodara, A., Sprecher, A., Fang, F., Song, W., Tao, C., & Jiang, J. (2011). A new method of reconstructing the human laryngeal architecture using micro-mri. *Journal of Voice*, 26, 555–562.
- Chu, T., Ranson, W., & Sutton, M. (1985). Applications of digital-image-correlation techniques to experimental mechanics. *Experimental Mechanics*, 25(3), 232–244.
- Dang-Tran, K., Dedouit, F., Joffre, F., Rougé, D., Rousseau, H., & Telmon, N. (2010). Thyroid cartilage ossification and multislice computed tomography examination: A useful tool for age assessment? *Journal of forensic sciences*, 55(3), 677–683.
- de Oliveira Rosa, M., & Pereira, J. (2008). Aerodynamic study of three-dimensional larynx models using finite element methods. *Journal of Sound and Vibration*, 311(1-2), 39–55.
- Deliyski, D. D., & Hillman, R. E. (2010). State of the art laryngeal imaging: research and clinical implications. *Current opinion in otolaryngology & head and neck surgery*, 18(3), 147.
- Deliyski, D. D., Petrushev, P. P., Bonilha, H. S., Gerlach, T. T., Martin-Harris, B., & Hillman, R. E. (2008). Clinical implementation of laryngeal high-speed videoendoscopy: challenges and evolution. *Folia Phoniatrica et Logopaedica*, 60(1), 33–44.

- Eckel, H., & Sittel, C. (1995). Morphometry of the larynx in horizontal sections. *American journal of otolaryngology*, 16(1), 40–48.
- Eckel, H., Sittel, C., Zorowka, P., & Jerke, A. (1994). Dimensions of the laryngeal framework in adults. *Surgical and Radiologic Anatomy*, 16(1), 31–36.
- Erath, B. D., & Plesniak, M. W. (2006a). An investigation of bimodal jet trajectory in flow through scaled models of the human vocal tract. *Experiments in Fluids*, 40(5), 683–696.
- Erath, B. D., & Plesniak, M. W. (2006b). An investigation of jet trajectory in flow through scaled vocal fold models with asymmetric glottal passages. *Experiments in fluids*, 41(5), 735–748.
- Erath, B. D., & Plesniak, M. W. (2006c). The occurrence of the coanda effect in pulsatile flow through static models of the human vocal folds. *The Journal of the Acoustical Society of America*, 120, 1000.
- Field, D. (1988). Laplacian smoothing and delaunay triangulations. *Communications in Applied Numerical Methods*, 4(6), 709–712.
- George, N., de Mul, F., Qiu, Q., Rakhorst, G., & Schutte, H. (2008). Depth-kymography: high-speed calibrated 3d imaging of human vocal fold vibration dynamics. *Physics in Medicine and Biology*, 53(10), 2667.
- Gökcan, M., Kurtuluş, D., Üstüner, E., Özyürek, E., Kesici, G., Erdem, S., Dursun, G., & Yağci, C. (2010). A computational study on the characteristics of airflow in bilateral abductor vocal fold immobility. *The Laryngoscope*, 120(9), 1808–1818.
- Gray, S., & Titze, I. (1988). Histologic investigation of hyperphonated canine vocal cords. *The Annals of Otology, Rhinology, and Laryngology*, 97(4 Pt 1), 381.

- Gunter, H. (2003). A mechanical model of vocal-fold collision with high spatial and temporal resolution. *The Journal of the Acoustical Society of America*, 113, 994.
- Gunter, H., Howe, R., Zeitels, S., Kobler, J., & Hillman, R. (2005). Measurement of vocal fold collision forces during phonation: Methods and preliminary data. *Journal of Speech, Language, and Hearing Research*, 48(3), 567.
- Guo, C., & Scherer, R. (1993). Finite element simulation of glottal flow and pressure. *The Journal of the Acoustical Society of America*, 94, 688.
- Helm, J., McNeill, S., & Sutton, M. (1996). Improved three-dimensional image correlation for surface displacement measurement. *Optical Engineering*, 35, 1911.
- Hess, M., Verdolini, K., Bierhals, W., Mansmann, U., & Gross, M. (1998). Endolaryngeal contact pressures*. *Journal of Voice*, 12(1), 50–67.
- Hiramatsu, H., Tokashiki, R., & Suzuki, M. (2008). Usefulness of three-dimensional computed tomography of the larynx for evaluation of unilateral vocal fold paralysis before and after treatment: technique and clinical applications. *European Archives of Oto-Rhino-Laryngology*, 265(6), 725–730.
- Hirano, M., Kurita, S., Yukizane, K., Hibi, S., et al. (1989). Asymmetry of the laryngeal framework: a morphologic study of cadaver larynges. *The Annals of Otology, Rhinology, and Laryngology*, 98(2), 135.
- Hofmans, G., Groot, G., Ranucci, M., Graziani, G., & Hirschberg, A. (2003). Unsteady flow through in-vitro models of the glottis. *The Journal of the Acoustical Society of America*, 113, 1658.
- Hunter, E., Hunter, L., & Titze, I. (2005). Individual subject laryngeal dimensions of multiple mammalian species for biomechanical models: A supplement. Tech.

- Rep. 9, he National Center for Voice and Speech.
- James, I. N. (1977). Physical fluid dynamics. by d. j. tritton. van nostrand reinhold, 1977. pp. 356. £12 (cloth) £5.50 (paperback). *Quarterly Journal of the Royal Meteorological Society*, 103(438), 827–827.
URL <http://dx.doi.org/10.1002/qj.49710343830>
- Jiang, J., Shah, A., Hess, M., Verdolini, K., Banzali, F., & Hanson, D. (2001). Vocal fold impact stress analysis. *Journal of Voice*, 15(1), 4–14.
- Jiang, J., & Titze, I. (1994). Measurement of vocal fold intraglottal pressure and impact stress. *Journal of Voice*, 8(2), 132–144.
- Johns, M. (2003). Update on the etiology, diagnosis, and treatment of vocal fold nodules, polyps, and cysts. *Current Opinion in Otolaryngology & Head and Neck Surgery*, 11(6), 456.
- Joshi, M., Joshi, S., & Joshi, S. (2001). Morphometric study of cricoid cartilages in western india. *Australasian Medical Journal*, 4, 542–547.
- Kazemirad, S., Bakhshaei, H., Mongeau, L., & Kost, K. (2013). Non-invasive in vivo measurement of the shear modulus of human vocal fold tissue. *Journal of Biomechanics, Under Review*.
- Kendall, K. A. (2012). High-speed digital imaging of the larynx: recent advances. *Current Opinion in Otolaryngology & Head and Neck Surgery*.
- Khosla, S., Murugappan, S., Lakhamraju, R., & Gutmark, E. (2008). Using particle imaging velocimetry to measure anterior-posterior velocity gradients in the excised canine larynx model. *The Annals of otology, rhinology, and laryngology*, 117(2), 134.

- Kjellgren, P., & Hyvärinen, J. (1998). An arbitrary lagrangian-eulerian finite element method. *Computational Mechanics*, 21(1), 81–90.
- Krane, M., Barry, M., & Wei, T. (2007). Unsteady behavior of flow in a scaled-up vocal folds model. *The Journal of the Acoustical Society of America*, 122, 3659.
- Krane, M., Barry, M., & Wei, T. (2010). Dynamics of temporal variations in phonatory flow. *The Journal of the Acoustical Society of America*, 128(1), 372.
- Krane, M., & Wei, T. (2006). Theoretical assessment of unsteady aerodynamic effects in phonation. *The Journal of the Acoustical Society of America*, 120, 1578.
- Krausert, C., Olszewski, A., Taylor, L., McMurray, J., Dailey, S., & Jiang, J. (2011). Mucosal wave measurement and visualization techniques. *Journal of Voice*, 25(4), 395–405.
- Kucinschi, B., Afjeh, A., & Scherer, R. (2008). On the application of the lattice boltzmann method to the investigation of glottal flow. *The Journal of the Acoustical Society of America*, 124(1), 523.
- Kucinschi, B., Scherer, R., DeWitt, K., & Ng, T. (2006). An experimental analysis of the pressures and flows within a driven mechanical model of phonation. *The Journal of the Acoustical Society of America*, 119, 3011.
- Lindestad, P., Hertegård, S., & Björck, G. (2004). Laryngeal adduction asymmetries in normal speaking subjects. *Logopedics Phoniatrics Vocology*, 29(3), 128–134.
- Lohscheller, J., Toy, H., Rosanowski, F., Eysholdt, U., & Döllinger, M. (2007). Clinically evaluated procedure for the reconstruction of vocal fold vibrations from endoscopic digital high-speed videos. *Medical Image Analysis*, 11(4), 400.

- Luo, H., Mittal, R., Zheng, X., Bielamowicz, S. A., Walsh, R. J., & Hahn, J. K. (2008). An immersed-boundary method for flow–structure interaction in biological systems with application to phonation. *Journal of Computational Physics*, 227(22), 9303–9332.
- Mattheus, W., & Brücker, C. (2011). Asymmetric glottal jet deflection: Differences of two-and three-dimensional models. *The Journal of the Acoustical Society of America*, 130(6), EL373–EL379.
- Miri, A., Mongrain, R., Chen, L., & Mongeau, L. (2012a). Quantitative assessment of the anisotropy of vocal fold tissue using shear rheometry and traction testing. *Journal of Biomechanics*, 45, 2943–2946.
- Miri, A. K., Barthelat, F., & Mongeau, L. (2012b). Effects of dehydration on the viscoelastic properties of vocal folds in large deformations. *Journal of Voice*, 26(6), 688–697.
- Mittal, R., Erath, B. D., & Plesniak, M. W. (2013). Fluid dynamics of human phonation and speech. *Annual Review of Fluid Mechanics*, 45, 437–467.
- Mongeau, L., Franchek, N., Coker, C., & Kubli, R. (1997). Characteristics of a pulsating jet through a small modulated orifice, with application to voice production. *The Journal of the Acoustical Society of America*, 102, 1121.
- Mupparapu, M., & Vuppala pati, A. (2005). Ossification of laryngeal cartilages on lateral cephalometric radiographs. *The Angle Orthodontist*, 75(2), 196–201.
- Neubauer, J., Zhang, Z., Miraghiae, R., & Berry, D. A. (2007). Coherent structures of the near field flow in a self-oscillating physical model of the vocal folds. *The Journal of the Acoustical Society of America*, 121, 1102.

- Oyamada, Y., Yumoto, E., Nakano, K., & Goto, H. (2005). Asymmetry of the vocal folds in patients with vocal fold immobility. *Archives of Otolaryngology- Head and Neck Surgery*, 131(5), 399.
- Park, J., & Mongeau, L. (2007). Instantaneous orifice discharge coefficient of a physical, driven model of the human larynx. *The Journal of the Acoustical Society of America*, 121, 442.
- Pelorson, X., Hirschberg, A., Van Hassel, R., Wijnands, A., & Auregan, Y. (1994). Theoretical and experimental study of quasisteady-flow separation within the glottis during phonation. application to a modified two-mass model. *The Journal of the Acoustical Society of America*, 96, 3416.
- Qian, Y., D'Humieres, D., & Lallemand, P. (1992). Lattice bgk model for navier-stokes equation. *Europhysics letters*, 17(6), 479–484.
- Rothenberg, M. (1973). A new inverse-filtering technique for deriving the glottal air flow waveform during voicing. *The Journal of the Acoustical Society of America*, 53, 1632.
- Roy, N., Merrill, R., Gray, S., & Smith, E. (2005). Voice disorders in the general population: prevalence, risk factors, and occupational impact. *The Laryngoscope*, 115(11), 1988–1995.
- Sarrate, J., Huerta, A., & Donea, J. (2001). Arbitrary lagrangian–eulerian formulation for fluid–rigid body interaction. *Computer Methods in Applied Mechanics and Engineering*, 190(24), 3171–3188.
- Scherer, R., Shinwari, D., De Witt, K., Zhang, C., Kucinschi, B., & Afjeh, A. (2001). Intraglottal pressure profiles for a symmetric and oblique glottis with a divergence

- angle of 10 degrees. *The Journal of the Acoustical Society of America*, 109(4), 1616–1630.
- Scherer, R., Torkaman, S., Kucinschi, B., & Afjeh, A. (2010). Intraglottal pressures in a three-dimensional model with a non-rectangular glottal shape. *The Journal of the Acoustical Society of America*, 128, 828.
- Sciamarella, D., & Le Quéré, P. (2008). Solving for unsteady airflow in a glottal model with immersed moving boundaries. *European Journal of Mechanics-B/Fluids*, 27(1), 42–53.
- Selbie, W. S., Gewalt, S. L., & Ludlow, C. L. (2002). Developing an anatomical model of the human laryngeal cartilages from magnetic resonance imaging. *The Journal of the Acoustical Society of America*, 112(3), 1077–1090.
- Sidlof, P. (2007). *Fluid-structure interaction in human vocal folds*. Ph.D. thesis, ENSTA ParisTech.
- Spencer, M., Siegmund, T., & Mongeau, L. (2008). Determination of superior surface strains and stresses, and vocal fold contact pressure in a synthetic larynx model using digital image correlation. *The Journal of the Acoustical Society of America*, 123, 1089.
- Sprinzl, G., Eckel, H., Sittel, C., Pototschnig, C., & Koebke, J. (1999). Morphometric measurements of the cartilaginous larynx: An anatomic correlate of laryngeal surgery. *Head & Neck*, 21(8), 743–750.
- Tao, C., Jiang, J., & Zhang, Y. (2006). Simulation of vocal fold impact pressures with a self-oscillating finite-element model. *The Journal of the Acoustical Society of America*, 119, 3987.

- Tayama, N., Chan, R., Kaga, K., & Titze, I. (2001). Geometric characterization of the laryngeal cartilage framework for the purpose of biomechanical modeling. *The Annals of Otology, Rhinology, and Laryngology*, 110(12), 1154.
- Titze, I. (1994). Mechanical stress in phonation. *Journal of Voice*, 8(2), 99–105.
- Triep, M., & Brücker, C. (2010). Three-dimensional nature of the glottal jet. *The Journal of the Acoustical Society of America*, 127, 1537.
- Verdolini, K., Chan, R., Titze, I., Hess, M., & Bierhals, W. (1998). Correspondence of electroglottographic closed quotient to vocal fold impact stress in excised canine larynges1. *Journal of Voice*, 12(4), 415–423.
- Verdolini, K., Hess, M., Titze, I., Bierhals, W., & Gross, M. (1999). Investigation of vocal fold impact stress in human subjects. *Journal of Voice*, 13(2), 184–202.
- Vilain, C., Pelorson, X., Fraysse, C., Deverge, M., Hirschberg, A., & Willems, J. (2004). Experimental validation of a quasi-steady theory for the flow through the glottis. *Journal of Sound and Vibration*, 276(3), 475–490.
- Voigt, D., Döllinger, M., Eysholdt, U., Yang, A., Gürlek, E., & Lohscheller, J. (2010). Objective detection and quantification of mucosal wave propagation. *The Journal of the Acoustical Society of America*, 128(5), EL347–EL353.
- Šidlof, P., Švec, J. G., Horáček, J., Veselý, J., Klepáček, I., & Havlík, R. (2008). Geometry of human vocal folds and glottal channel for mathematical and biomechanical modeling of voice production. *Journal of Biomechanics*, 41(5), 985–995.
- Windisch, G., Hammer, G., Prodinger, P., Friedrich, G., & Anderhuber, F. (2010). The functional anatomy of the cricothyroid joint. *Surgical and radiologic anatomy*, 32(2), 135–139.

- Wittenberg, T., Moser, M., Tigges, M., & Eysholdt, U. (1995). Recording, processing, and analysis of digital high-speed sequences in glottography. *Machine Vision and Applications*, 8(6), 399–404.
- Yan, Y., Chen, X., & Bless, D. (2006). Automatic tracing of vocal-fold motion from high-speed digital images. *IEEE Transactions on Biomedical Engineering*, 53(7), 1394–1400.
- Yushkevich, P. A., Piven, J., Cody Hazlett, H., Gimpel Smith, R., Ho, S., Gee, J. C., & Gerig, G. (2006). User-guided 3D active contour segmentation of anatomical structures: Significantly improved efficiency and reliability. *Neuroimage*, 31(3), 1116–1128.
- Zhang, Y., Bieging, E., Tsui, H., & Jiang, J. (2010). Efficient and effective extraction of vocal fold vibratory patterns from high-speed digital imaging. *Journal of Voice*, 24(1), 21–29.
- Zhang, Y., Shao, J., Krausert, C. R., Zhang, S., & Jiang, J. J. (2011). High-speed image analysis reveals chaotic vibratory behaviors of pathological vocal folds. *Chaos, Solitons & Fractals*, 44(1), 169–177.
- Zhang, Z., Mongeau, L., & Frankel, S. (2002). Experimental verification of the quasi-steady approximation for aerodynamic sound generation by pulsating jets in tubes. *The Journal of the Acoustical Society of America*, 112, 1652.
- Zhao, W., Zhang, C., Frankel, S., & Mongeau, L. (2002). Computational aeroacoustics of phonation, part i: Computational methods and sound generation mechanisms. *The Journal of the Acoustical Society of America*, 112, 2134.

- Zheng, X., Bielamowicz, S., Luo, H., & Mittal, R. (2009). A computational study of the effect of false vocal folds on glottal flow and vocal fold vibration during phonation. *Annals of Biomedical Engineering*, 37(3), 625–642.
- Zheng, X., Mittal, R., & Bielamowicz, S. (2011a). A computational study of asymmetric glottal jet deflection during phonation. *The Journal of the Acoustical Society of America*, 129(4), 2133.
- Zheng, X., Mittal, R., Xue, Q., & Bielamowicz, S. (2011b). Direct-numerical simulation of the glottal jet and vocal-fold dynamics in a three-dimensional laryngeal model. *The Journal of the Acoustical Society of America*, 130(1), 404.
- Zheng, X., Xue, Q., Beilamowicz, S., et al. (2010). A coupled sharp-interface immersed boundary-finite-element method for flow-structure interaction with application to human phonation. *Journal of Biomechanical Engineering*, 132, 111003–1–12.